UNIVERSITY OF CALIFORNIA

Los Angeles

A Single Photon Detector based on the principle of Photoconductive Gain

A dissertation submitted in partial satisfaction of the requirements for the degree Doctor of Philosophy in Electrical Engineering

by

Deepak Sethu Rao

2005

The thesis of Deepak Sethu Rao is approved.

Hong-Wen Jiang

Vwani Roychowdhury

Bahram Jalali

Eli Yablonovitch, Committee Chair

University of California, Los Angeles

2005

TABLE OF CONTENTS

LIST OF FIGURES

ACKNOWLEDGEMENTS

I am indebted to numerous people for their support and encouragement during my graduate career at UCLA. First and foremost, I would like to express my sincere gratitude to my advisor, Prof. Eli Yablonovitch for his scientific guidance and financial support that made the work presented in this dissertation possible. His simple intuitive approaches to seemingly complex problems have been the driving factors that led to the successful completion of this work. I am very deeply indebted to him for his unwavering enthusiasm, optimism and encouragement at every stage of my graduate career over the past five and half years.

This dissertation would also not have been possible without the love, moral support and encouragement of my parents, Sethu Rao and Geetha Rao, and my sister, Preethi. I would like to specially thank my father for always making me always look at the bright side of things and bring out the best of my abilities.

I am deeply indebted to Prof. Hong-Wen Jiang who has served as the co-advisor on my dissertation. His theoretical expertise in condensed matter physics and subtle insights into the art of cryogenic experiments has been invaluable for the success of this work. I would also like to express my sincere thanks to Prof. Vwani Roychowdhury and Prof. Bahram Jalali for serving on my thesis committee, and making the time to participate in my qualifying examination at very short notice.

I am very hugely indebted to my colleagues Hideo Kosaka, Hans Robinson and Thomas Szkopek, Prabhakar Bandaru. Sincere thanks to Hideo for being my mentor during my early years at graduate school, helping me learn the ropes in the clean room

and teaching me the mysterious art of device fabrication. His extraordinary attention to detail and patience is something I would always want to imitate. Hans and Thomas have been my close colleagues in research for almost the entire duration of my graduate career and I would like to sincerely express my gratitude to them for their help during device characterization and experimental set-up. Hans was the low temperature experimental Guru of our team and was always there to help re-kindle our temperamental cryostat. I would also like to thank Thomas for the many memorable discussions about science and religion, philosophy, politics and life in general. I am very grateful to Prabhakar for his invaluable advice in solving many major materials issues and for training me on our e-Beam lithography system. It was real pleasure, excitement and fun working with them.

The fabrication of the devices would have remained all the more elusive without the support of the staff at the Nanoelectronics Research Facility in UCLA. I would like to express my sincere thanks to Steve Franz, Hoc Ngo, Tom Lee, Hyung Do, Wilson Lin, Ivan Alvarado and Jamie Jung. In particular I would like to thank Hoc for help in developing recipes for evaporating new metals in the e-beam evaporator and Ivan Alvarado for quickly fixing problems with the e-Beam writer.

I would also like to thank Jun Chen in Prof. Frank Chang's group for the many invaluable bits of information on InP processing and Toshitsugu Sakamoto from NEC, Japan for providing devices during the early years of my research.

Special thanks are due to my college friend and labmate Adityaram Narasimha for being like family here and for the many inspiring, cheerful discussions and late night Racquetball sessions. I would also like to thank my longtime friend from undergrad,

Ramesh Chokkalingam for the many fun get-togethers and invitations for every special occasion.

A number of people have kept our group running smoothly. I would like express my sincere thanks to Janie Lee-Docter, Jaymie Otayde, Janet Lin for processing the numerous purchase orders and graduate school paperwork. Special thanks to Dorothy Tarkington for processing and keeping track of all the Liquid Helium and Nitrogen orders. My thanks to Ilhee Choi, Cheryl Childress, Letecia Domiguez and Deeona Columbia for making all the administrative tasks seem transparent.

I would finally like to acknowledge Defense Advanced Research Projects Agency (DARPA), Defense MicroElectronics Activity (DMEA), California NanoSystems Institute (CNSI), Center for NanoScience Innovation for Defense (CNID) and Microelectronics Advanced Research Corporation (MARCO) for financially supporting this work.

ABSTRACT OF THE DISSERTATION

A Single Photon Detector based on the principle of

Photoconductive Gain

by

Deepak Sethu Rao

Doctor of Philosophy in Electrical Engineering

University of California Los Angeles, 2005

Professor Eli Yablonovitch, Chair

The transmission of information encoded onto internal spin states of single photons will allow for new forms of data security, based on Quantum Cryptography. The long distance transmission of quantum information requires unconventional regeneration techniques, which involve the sharing of polarization entangled pairs of photons across the tele-communications channel. At every repeater node, a detector must be made available that detects the successful arrival of one photon of an entangled pair in a non-invasive way preserving the polarization information. Conventional single photon detectors based on avalanche gain mechanisms destroy the original photo-excited carrier, which would result in a loss of entanglement. In this dissertation, we present the implementation of a single

photon detector with a gentle photo-conductive gain mechanism that allows for the safe storage and preservation of single photo-excited electrons. Surface gate electrodes on a conventional modulation doped field effect transistor have been used to create electrostatic quantum dots (QD) that can be controllably created and prepared for photo-electron trapping, storage and detection. A point contact field-effect transistor (FET), also created by electrostatic squeezing of the electron gas in the modulation doped heterostructure, functions as a highly sensitive electrometer coupled electro-statically to the charge (spin) preserving quantum dot.

CHAPTER 1 Introduction

1.1. Motivation for a new type of Single Photon Detector

The detection of single quanta of electromagnetic radiation has been traditionally motivated by applications such as materials characterization, medical imaging and diagnosis, chemical analysis and far-infrared spectroscopic research. Over the last two decades, through the merger of concepts in Classical Information Theory and Quantum Physics has emerged the new field of "Quantum Information Science", which in turn has brought forth new technologies such as Quantum Computing and Quantum Cryptography. Quantum information technologies promise unparalleled information processing and secure tele-communications capabilities. With the emergence of these new technologies, the need has arisen to perform more than just the detection of the individual quanta of electromagnetic energy. For example, Quantum Cryptography relies for security on the quantum uncertainty principle, by encoding information onto the intrinsic quantum states of single photons. Hence, it is required of single photon detectors to perform more than just detect the presence or absence of a single photon; they need to have the additional capability of providing a read-out mechanism for the quantum states of single photons over a quantum tele-communications channel.

Conventionally, single photons are detected by the multiplication of a photogenerated carrier through an avalanche gain process, either in a vacuum photomultiplier tube, or, in

the case of the semiconductor avalanche photodiode, a reverse biased junction. These detections mechanisms are rather violent processes that of course provide the gain for single photon detection, but in the process destroy the photo-excited carrier. Such a detection mechanism would be unable to cater to the requirements of new technologies such as quantum tele-communications. Hence, the necessity has arisen for a new type single photon detector at optical communications frequencies that not only flags the arrival of a single photon, but does so through a gentle gain mechanism and stores the photo-excited carrier for quantum information processing and read-out. The implementation, fabrication and characterization of such a single photon detector is the presented in this dissertation. We briefly introduce the emerging field of Quantum Tele-Communications to the reader in the next three sections of this chapter.

1.2. Classical Cryptography: The “Key” distribution problem

Various techniques have been developed over time to achieve the goal of secure communication of information [1], but the art of concealing information has always been under attack by the ingenuity of code breakers. Cryptography, in general, relies on sharing a secret "key" between legitimate users that can be used to encrypt and decrypt messages. In digital cryptography the key is simply a random string of binary digits used to encode messages following standard algorithms. These encrypting and decrypting algorithms can be publicly known, provided that the secrecy of the key can be guaranteed. Such a Private Key Cryptographic scheme also commonly known as "One-time Pads" can ensure a perfectly secure transmission link as long as the key is truly

random, has the same length as the message, and is never re-used for more than one transaction [2]. A technical problem with this Private Key scheme is the requirement of a perfectly secure channel in the first place to share the key between the end users. In other words, secure *key distribution* over classical communication channels can never be guaranteed. Classical channels can always be passively monitored without legitimate users being aware of the presence of eavesdroppers.

Currently, this problem has been overcome by alternative cryptographic schemes that do not rely on the sharing a private key prior to message transmissions. Instead the key is made public and the burden of ensuring secrecy has been transferred onto the algorithms used for encryption and decryption. Such Public Key Cryptographic schemes rely on complexity of certain classes of mathematical problems that are not reversible. The most popular Public Key scheme used for secure transactions over the Internet is the RSA cryptosystem, named after it's developers Rivest, Shamir and Adleman [3]. RSA encryption gets it's security from the difficulty of finding prime factors of large numbers. Two different keys are used over the network: a public key for encryption (A large decimal number N) and a private key for decryption (Prime factors of N). The security in the RSA system relies on the fact that even with the best known algorithms for factorizing large numbers on a classical computer, the computing time increasing exponentially with increasing the number of digits in N. Hence with a sufficiently large number, the task becomes intractable. A message coded using a certain encrypting key can be deciphered only by the user to who publicly announced the encrypting key to the

world and who had prior knowledge of the prime factors. Although such a public key cryptosystem has been very successful thus far, it is only *computationally* secure. As long an eavesdropper intercepting the coded message doesn't have sufficient resources in terms of computation time and processing power to decipher the message, the transaction remains to be secure.

However, with theoretical developments in of field of Quantum Information Science, algorithms that render the RSA system vulnerable to eavesdropping have already been proposed [4]. Such algorithms utilize on the Quantum behavior of single particles such as superposition and entanglement to efficiently factorize large numbers over time scales much faster than classical computers. Although the implementation of these algorithms awaits the development of a Quantum Computer, it is conceivable that an eavesdropper can listen to and store sensitive encrypted information that is currently exchanged across the world and decode it when a Quantum Computer does become available! Hence there is an urgent need for the implementation of other forms of Cryptography that doesn't rely on mathematical complexity.

1.3. Quantum Key Distribution (QKD)

An alternative to the mathematical solution for the key distribution problem is a physical solution that relies on the "quantum uncertainty" principle of single particles. The security that quantum computation takes away from classical Public Key

cryptographic schemes is provided by quantum tele-communications. Cryptography with quantum information is inherently secure because each bit in a cryptographic key is encoded upon quantum states of a single photon. For instance, the polarization states of single photons can be used for encoding the bits of a cryptographic key [5, 6]. The quantum uncertainty principle ensures that the observation of any quantum system will not yield complete information of the system prior to observation. Further the measurement will lead to unavoidable and detectable disturbances in the quantum state. Hence any attempts by an eavesdropper to "hack" or copy this key will quickly become obvious to the sender and receiver. An encryption scheme that relies on the uncertainty principle in polarization states chosen from two orthogonal bases is shown in Figure 1.1. The scheme was proposed by Bennett and Brassard in 1984 [6]. Three specific cases can be identified in this scheme:

Case (i) where the receiver Bob and eavesdropper Eve use the same basis for polarization measurement as Alice's preparation basis [Columns A, D, E in figure];

Case (ii) where Bob uses a basis different from Alice's preparation basis [Columns C and F];

Case (iii) where Bob uses the same basis as Alice's, but Eve uses a wrong basis for measurement in-between [Columns B and G]

In case (i) the presence of Eve goes undetected as expected. Case (ii) simply reduces the data transfer rate since at the end of the transmission Alice and Bob would just ignore these bits knowing fully well that their results would have lost correlation. The interesting case is (iii) which has no classical analog. Eve's measurement using a wrong basis

creates a superposition of polarization states, as a result of which, Bob might end up with a wrong polarization even though he used the same basis as Alice. At the end of the transmission if Alice and Bob compare a portion of their key data (sacrificial bits), there would be errors in atleast 25% of the cases due to the presence of Eve. Thus using a simple quantum protocol such as BB84 using single photons, would ensure a verifiably secure communications channel.

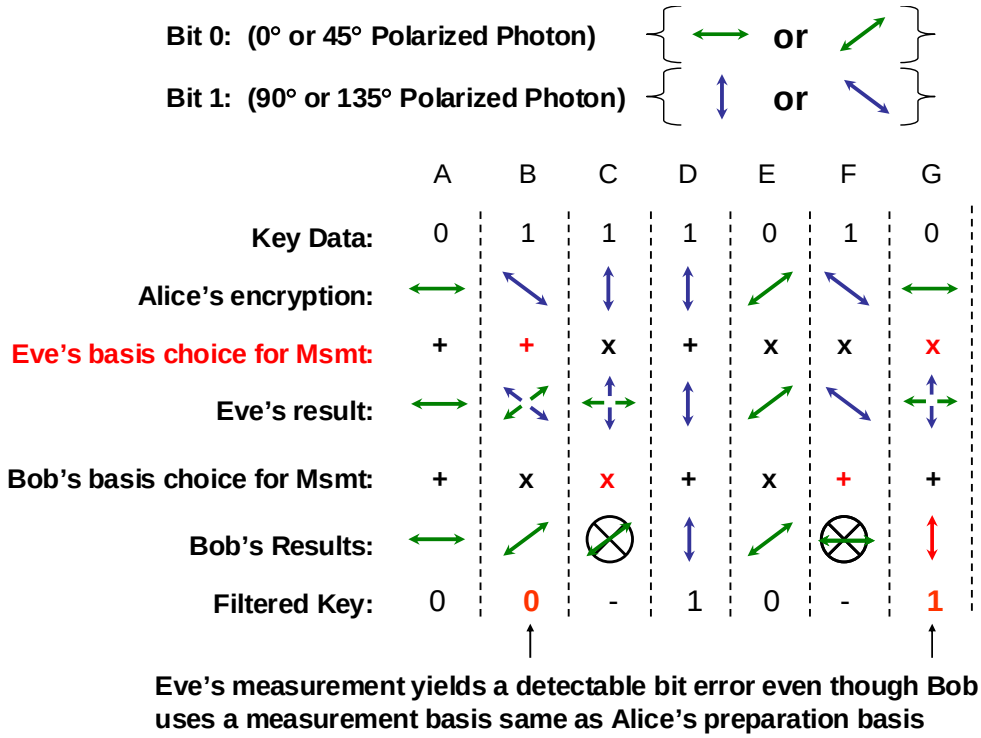

Figure 1.1: 4-state polarization protocol for Quantum Cryptography due to Bennett and Brassard [6]. Security is derived from the Quantum uncertainty principle, which prevents an eavesdropper to obtain complete information about a quantum state without causing an irreversible and detectable quantum state collapse.

Quantum Cryptographic protocols have been successfully implemented using standard telecommunication fibers [7] and commercial QKD black boxes for transmission of key data upto 100 km are being made available [8]. But thus far, the transmission distance has been an important limitation in Quantum Cryptography. Due to fiber losses, the bit rate diminishes significantly with increasing distance, ultimately making key distribution impossible. To enhance the transmission distance and implement QKD over a global network there is a need for a Quantum Tele-communications Repeater.

1.4. Quantum Repeater for long-distance QKD

A conventional '3-R' Repeater utilized in an optical tele-communications system performs the tasks of pulse Re-generation, Re-Shaping and Re-timing. Unlike such repeaters, a repeater in a quantum tele-communications channel cannot be allowed to *read* incoming information for the purpose of re-transmission. Measuring quantum information encoded in an individual photon would collapse the photon's quantum state just like in the act of eavesdropping. The act of re-generating an unknown quantum state without measurement becomes possible through long distance sharing of "Quantum Entanglement" resulting in the form of information transfer known as Quantum Teleportation [9]. Quantum entanglement allows two particles to behave as one even if they are very far apart. Such a non-local correlation between particles, although initially had raised doubts about the validity of Quantum Mechanics [10], has now been demonstrated experimentally by various groups [11-15]. Quantum Teleportation

essentially is a sophisticated process of information transfer that requires the sharing of entangled pairs of photons between two distant locations. Information is "teleported" between such entangled photons, through a series of quantum measurements in the two particle Bell basis [16, 17]. Figure 1.2 below presents the circuit diagram of Quantum tele-communications system incorporating a repeater based on teleportation.

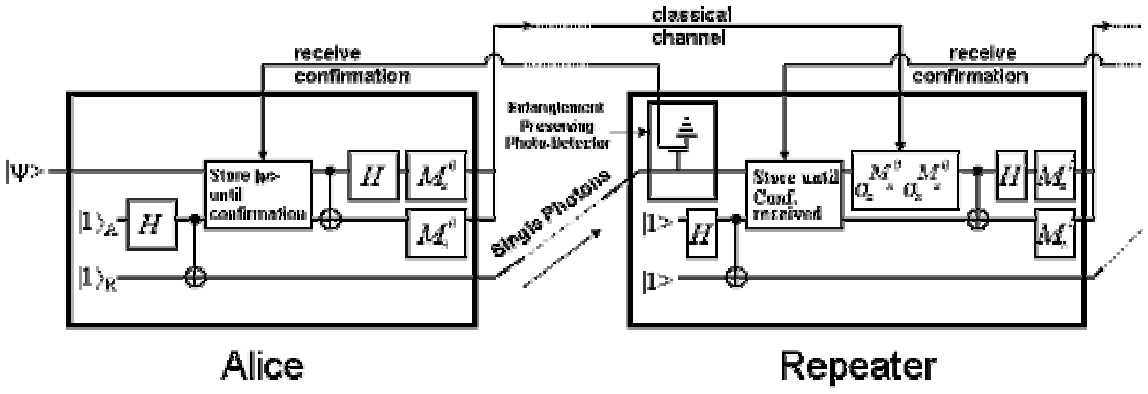

Figure 1.2: Circuit level diagram of a transmitter and repeater in a quantum communications channel for teleportation of quantum information (Due to Prof. Vwani Roychowdhury and Prof. Eli Yablonovitch)

The following paragraphs explain the basic elements of quantum teleportation. For detailed descriptions, we refer the reader to references [16-18]. Teleportation is a simple quantum algorithm operating on just three quantum bits and a quantum repeater could be viewed as a stepping stone to a full-fledged quantum computer. The qubit $|\psi\rangle = \alpha|0\rangle + \beta|1\rangle$ in Figure 1.2 represents the general case of a quantum bit with probability amplitudes 'α' and 'β' that constitute the information content in $|\psi\rangle$. A dummy entangled pair of particles is used to establish non-local correlations between two distant nodes in

the network. In Figure 1.2, the entangled pair is generated by quantum gate operation on two pure eigen states $|1\rangle_A$ and $|1\rangle_R$. "H" indicates a 1-bit Hadamard operation (that converts the pure input $|1\rangle_A$ into a superposition state $^1/_{\sqrt{2}}$ ($|0\rangle$ - $|1\rangle$) [18]) and "$\oplus$" indicates a 2-bit controlled-NOT operation. These two quantum gates operating together on the two pure input qubits in state $|1\rangle$ create the entangled singlet state $^1/_{\sqrt{2}}$ ($|01\rangle$ - $|10\rangle$). One half of this entangled singlet pair is retained by the sender Alice and the other half is transmitted over a regular classical channel to the next node on the link, the repeater. The secret to the success of quantum information repetition is the fact the actual qubit $|\psi\rangle$ is never sent over noisy and lossy classical channels. Singlet pairs carry no special quantum information and can be generated as many times as required till entanglement is successfully shared between two different locations. Following the sharing of entanglement, a set of joint quantum measurements on $|\psi\rangle$ and $|1\rangle_A$ at the transmitter end followed qubit transformations on $|1\rangle_R$ at the repeater end converts $|1\rangle_R$ into $|\psi\rangle$ with the correct probability amplitudes α and β [16].

The circuit level description in Figure 1.2 provides the complete set of quantum operations and quantum gates required for teleportation of quantum information. The most essential step in the entire process is the long distance sharing of quantum entanglement. In Figure 1.3, we show a potential implementation of such a teleportation circuit using off-the shelf components for some of the required tasks. Entangled singlet pair of photons can be readily generated by non-linear optical parametric down conversion [19, 20] and can be shared between adjacent nodes through repeated attempts.

Following this, entanglement can spread over non-adjacent nodes through "Entanglement Swapping" [21, 22]. Swapping entanglement involves a Bell measurement on two particles, each of which constitutes one half of two separate EPR pairs. In Figure 1.3, we show an entanglement swapping scheme between entangled photon pairs through the use of a simple beam splitter and two photon counters D1 and D2. This scheme is inspired by a proposal for a quantum repeater using atomic ensembles by Duan-Lukin [23]. A simultaneous click on both the photon counters means that the two input photons have been projected onto a spatially anti-symmetric state. Since photons are bosons, this can occur only when they are anti-symmetric in their internal polarization states (singlet state), so that the overall state remains symmetric. Hence it is easy to perform a partial bell state measurement of the singlet polarization state using such an arrangement. Following this projection measurement of one half of two EPR pairs, the other halves will collapse into a singlet state as well accomplishing the sharing of entanglement between non-adjacent nodes. Eventually entanglement can be spread across the entire link and shared between the transmitter and receiver.

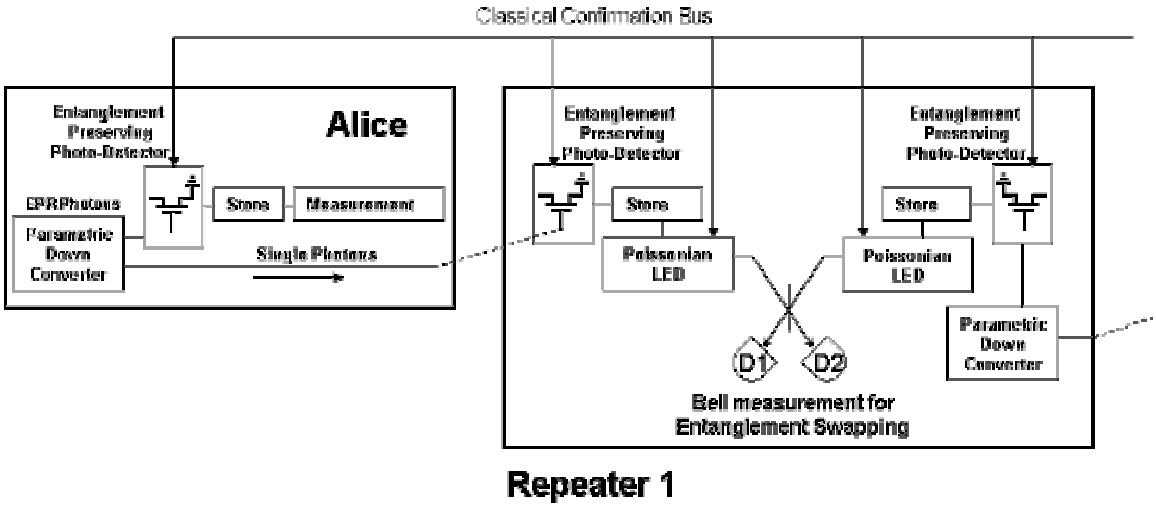

Figure 1.3: System level implementation diagram for teleportation of quantum information. Entangled EPR pairs of photons are generated through a non-linear parametric down converter and shared between adjacent nodes. A Bell measurement set-up utilizing a beam splitter and two photon counters allows for entanglement exchange (swapping) between non-adjacent nodes.

An essential device in the block diagrams of Figure 1.2 and Figure 1.3, that we have refrained from describing thus far, is the "Entanglement preserving photodetector". This detector positioned at the front-end of every node in the quantum communications channel is required to flag the successful arrival of a photon that provides sharing of entanglement between different locations. The realization of a single photon detector suitable for entanglement preservation and measurement is the topic of this dissertation.

CHAPTER 2 FET Single Photon Detector

In this chapter we discuss the use of a conventional Field Effect Transistor as a highly sensitive electrometer for detecting single photo-excited electrons. The gain for single photon detection is derived from a Photo-Conductive amplification process in the channel of the Field effect transistor. We first discuss the principle behind such an amplification process that is crucial for a non-invasive Single Photon Detector necessary for a Quantum Repeater and follow by a discussion on the ultimate limits on such a FET based electrometer. We show that the ultimate limit can be expressed in terms of a few fundamental constants of nature, suggesting that this limit is not specific to the FET implementation but could be generalized to other types of nanoscale electrometers as well.

2.1. The mechanism of Photo-Conductive Gain

Photo-induced changes in the conductivity of a semiconductor sample is commonly observed through the mechanism of *Primary Photoconductivity* [24], where in the photo-exited carriers are directly involved in altering the density of carriers in the conductor. For example, in a P-I-N photo-diode, the photo-excited carriers directly contribute to the enhanced conductivity of the detector when they are swept by the electric field across the PN junction. Similarly, in a strongly reverse biased PN junction avalanche photodiode, the photo-excited carriers cause an avalanche build of excess carriers by the process of impact ionization providing the gain mechanism for the

detection of weak optical signals. Such a primary gain mechanism where photo-excited carriers are lost in the gain process would be too violent for the detection of single photons carrying quantum information.

An alternate mechanism for single photon detection that is suitable for quantum tele-communications is the mechanism of *Photo-conductive Gain* derived from *Secondary Photo-conductivity* in photo-detectors. In secondary photo-conductivity, photo-excited carriers are first trapped in or near the channel of the conductor, and for every trapped photo-carrier, a large number of carriers are transferred over time from the source to the drain Ohmic contacts. In fact, a perfect example of such a *Conductive Gain* mechanism is the Random Telegraph Noise observed in small channel FETs discussed in section 2.3. The random telegraph-like switching of the channel current between discrete states is a reflection of the trapping and de-trapping of single electrons by defect centers close to the channel.

The mechanism of Photo-conductive Gain is schematically shown Figure 2.1. The trapping of one type of photo-carrier, for instance the hole, affects the band structure in the channel region that results in a discrete increase in the electron concentration. These excess electrons are quickly transported towards the drain electrode by the source-drain electric field. The excess carrier concentration is continuously replenished by the source electrode for the trapping duration of the hole.

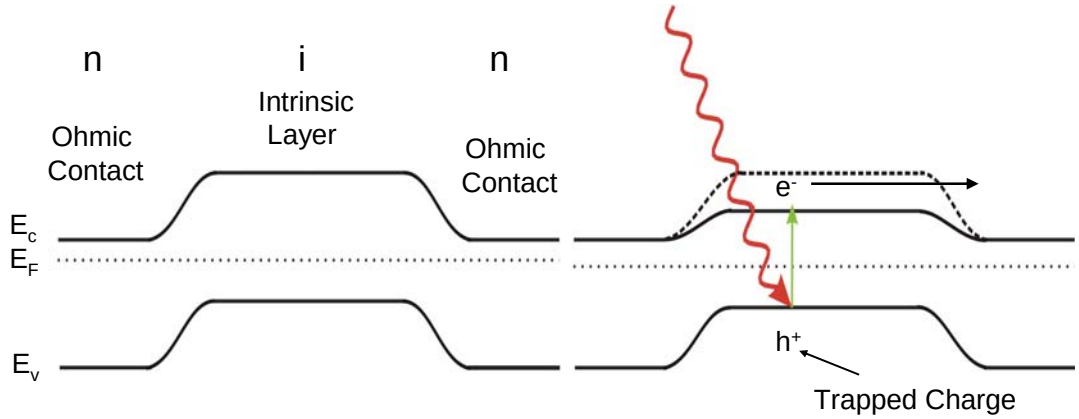

Figure 2.1: Photoconductive gain mechanism. Trapping of one type of charge carrier causes a discrete change in electron concentration in the channel by a simple electrostatic effect. The long-lived electron current passing through the channel over time is responsible for the gain.

The mechanism of photoconductive gain is not dissimilar to the gain mechanisms observed in other devices such as photoconductors and Bi-polar Junction Transistors. A photoconductor is a device that exhibits an internal gain mechanism. The gain in a photoconductor results from the fact that the recombination time of the photo-excited carriers is significantly longer than the transit time through the conductor.

When the photoconductor is illuminated by light with an incident flux of Φ, the photo generated free electrons at steady state is given by $R = \Phi \tau_r$ where 'τ_r' is the recombination life-time of a free electron. Thus, the photocurrent 'I_p' when an external bias is applied across the Ohmic contacts is given by $I_p = \frac{R\,e}{T_t} = \Phi\left(\frac{\tau_r}{T_t}\right)$ where 'T_t' is

the transit time of a free electron between the Ohmic contacts. It is clear that a smaller transit time compared to the recombination time provides for gain in the photoconductor. This can also be perceived as one of the photo-excited carriers, like the hole, getting trapped for the duration of the recombination time, while the photo-excited electron transits across the length of the device. The requirement for charge neutrality forces the Ohmic contacts to provide another electron instantaneously. Hence, for a single absorbed photon a vast number of charges are transported through the channel giving rise to the gain. Likewise, the gain in a BJT is simply derived from the ratio of the long carrier recombination time of carriers injected into the Base region to the short transit time of carriers emitted from the Emitter to the Collector across the thin Base region of the transistor.

In the detector implementation that will be discussed in this dissertation, we have utilized artificially created potential wells to trap and hold single photo-injected electrons and utilize the *Photo-Conductive Gain* mechanism in the channel of an integrated Field Effect Transistor. The FET implemented in the form of a Quantum Point Contact non-invasively senses single photo-electrons added to the artificial quantum dot potential well trap. The FET and the trapping potential well are created electro-statically by negatively biased gate electrodes on the surface of a modulation doped semiconductor heterostructure. The design of the heterostructure, device implementation, fabrication and characterization will be discussed in the following chapters.

2.2. Defining the *Sensitivity* of an Electrometer

The charge on a single electron was determined as early as 1911 by Millikan through a carefully designed experiment that allowed the suspension of charged oil-drops in free space by an external electric field [25]. The experiment, although very successful in indirectly deducing the charge on a single electron, did not actually perform any measurement that required the control over single electronic charges. With the present miniaturization trend in electronics, devices that contain just a few electrons in the active area have already become part of large scale integrated semiconductor chip. It is conceivable that in the near future devices that probe and manipulate single electrons would play a major role in electronic chips. New technologies such as Quantum computing based on the spin degree of freedom of a single electron need un-precedented control over not only the charge, but also the spin of single electrons in semiconductors [26]. Due to the tremendous progress in nano-fabrication techniques, the issue of fabricating such devices capable of addressing and probing single electrons in semiconductors is no longer a matter of great concern. The topic that is still debatable is the most favorable (and relatively simple) technique for detecting, manipulating and controlling single electrons in semiconductors. We make our case for utilizing a conventional field-effect transistor for detecting single electronic events in this chapter.

Single electronic charge detectors are normally characterized in terms of their *Noise Equivalent Charge* (NEC), also known as the *Charge Noise* or *Charge Sensitivity* of the detector expressed in $e/\sqrt{Hz}$. *Charge Noise* represents the minimum detectable charge

δQ_{min} that would result in Signal to Noise Ratio (SNR) of unity in a given bandwidth. In other words, NEC represents the maximum bandwidth that allows the measurement of a single electronic charge with a unity Signal to Noise Ratio. Mathematically, δQ_{min} in units of $e/\sqrt{Hz}$ can be defined as

$$\delta Q_{min} = \frac{\sqrt{\text{Noise Spectral Density}}}{\text{Signal due to a Single Electron}} \frac{A/\sqrt{Hz}}{A/e^-} = \frac{1}{SNR} \frac{e}{\sqrt{Hz}} \tag{2.1}$$

The ultimate limit on the detection of weak signals is inevitably dictated by noise in the measuring device in addition to the noise in the measurement system. Naturally, minimizing noise is crucial for the overall sensitivity of any type of single photon detector. Though extrinsic sources of noise can be reduced by a well-designed experimental set-up, intrinsic noise sources namely, Shot Noise and Thermal Noise, both of which have a white spectral power density, ultimately determine the performance of the device.

In the sections that follow, we discuss a characteristic single electron phenomenon already observed in the channel current of conventional field effect transistors and estimate the ultimate limits on the detection bandwidth of an electrometer limited by just intrinsic noise sources in the device.

2.3. Random Telegraph Noise in a small channel FET

The tremendous progress in nanoscale fabrication techniques, has made it possible to produce electronic devices with an active volume so small that only a small number of charge carriers contribute to the device operation. In this section we introduce the reader to a striking feature observed in the channel current of a narrow channel FET, that provides very strong evidence to the fact that single electronic charges are already detectable in conventional field effect transistors.

As an example of a nanoscale device, with dimensions comparable to quantum mechanical parameters, we consider the case of the state of the art Pentium® processor that has transistors with a gate length of 50nm. The Fermi wavelength 'λ_F' of the electrons in the channel can be estimated as $h / \lambda_F = m^* v_s$ where h is the Planck's constant, m^* is the effective mass of electrons in the conduction band of Silicon ($0.2 \times 9.1 \times 10^{-31}$ Kg), and 'v_s' is the saturation velocity of electrons in the channel (10^7 cm/sec). The above expression yields a Fermi wavelength $\lambda_F \sim 36$nm. Thus, the fabricated gate length is approaching just one Fermi wavelength! A consequence of this drastic device miniaturization is the reduced interaction between the device and it's environment that includes defects and traps in the vicinity of the active area. In Si MOSFETs, the traps that matter the most in impeding device operation are the interface traps at the Si-SiO_2 interface near the inversion channel. A great deal of perfection has been achieved by the silicon industry in the oxidation of Silicon and interface trap density has been reduced to

the order of 10^8 -10^{10}/cm^2-eV [27]. Thus, a device of the size of 1μm^2, would have just about 1-100 defects/eV.

An interesting feature that arises in the source-drain channel current of a sub-micron FET is the random switching behavior of the channel current between discrete levels. Such a fluctuating signal, which is reminiscent of a telegraph communication channel, is known as a Random Telegraph Signal (RTS) or Random Telegraph Noise (RTN) measured in the channel current. A typical example of RTN in the channel current of a narrow channel transistor is shown in Figure 2.2.

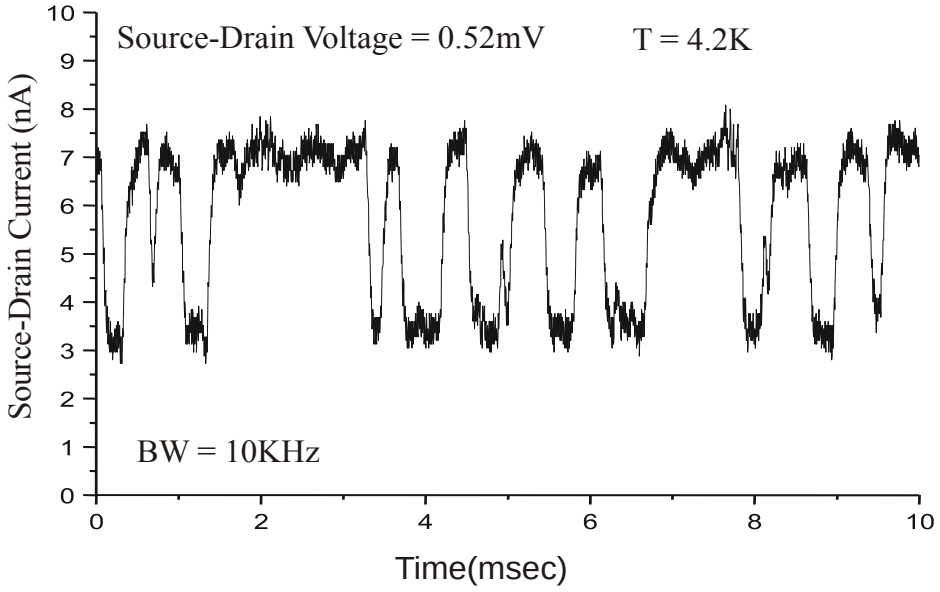

Figure 2.2: Random Telegraph Noise (RTN) in the source/drain current of a narrow channel field effect transistor. The switching reflects the fluctuating occupancy of a nearby *single* electron trap.

Random Telegraph noise is caused by the trapping and de-trapping of single electrons from the channel by defect states at the Si-SiO_2 interface and in the oxide [28]. These traps can be either donor type or acceptor type traps. The alternate charging and discharging of a trap modulates the conductance of the channel by a simple electrostatic interaction.

The observation of Random Telegraph Noise strongly suggests that trapping of charge carriers near the channel of a conventional FET, can provide the required sensitivity for single electron detection and makes unnecessary other sophisticated geometries such as Single Electron Transistors (SETs) specially fabricated to detect single electrons [29-31]. RTN caused by a single electron trap is a signature single electron phenomenon already observable in existing transistors. As discussed in the previous section the figure of merit for a single electronic charge detection mechanism is the Noise Equivalent Charge (NEC) or equivalently the minimum detectable charge δQ_{min} in a given bandwidth.

An experimental value for δQ_{min}, can be estimated from the amplitude of the random telegraph switching noise in Figure 2.2 that is caused by single electron trapping and de-trapping events near the channel. The observed peak-to-peak noise current is 0.25 nA, which corresponds to a RMS noise current of $0.25/2\sqrt{2} = 88.25\text{pA}$. In the measurement bandwidth of 10kHz we get the spectral noise density as $0.8825\,\text{pA}/\sqrt{\text{Hz}}$. The signal step due to a single electron is about 4nA. Plugging the above values into equation (2.1) gives the experimentally observed *Charge Sensitivity* of 2.2 x 10^{-4} $\text{e}/\sqrt{\text{Hz}}$. This simply

implies that the maximum speed of detection beyond which the signal to noise ratio would degrade below unity for the specific FET channel in Figure 2.2 is about 20MHz. In the following sections we derive the theoretical limit on the above detection bandwidth.

2.4. Limits on the speed of single electron detection

The ultimate limit on the detectability of weak signals is limited by Shot Noise and Thermal Noise in the measuring device. Noise is best characterized by it's spectral density, $S_n(f)$ which is the Fourier transform of the time-varying fluctuations in measured signal. Both Shot Noise and Thermal Noise have a white spectral power density as explained below.

Thermal noise in electrical measurements, also known as Johnson noise, is the result of random thermal motion of electrons at non-zero temperatures. This random movement of electrons causes a statistically fluctuating signal in the device even in the absence of any external bias. Mathematically, thermal noise is modeled as a Gaussian random process [32] with a white noise like spectral density given by

$$S_n = \frac{4k_B T}{R} \tag{2.2}$$

where k_B is the Boltzmann constant, T is the absolute temperature and R is the resistance of the device under test. The corresponding mean squared value of the thermal noise current in a frequency range $(0, \Delta f]$, is given by

$$\left\langle I^2 \right\rangle_{Thermal} = \frac{4k_B T \Delta f}{R} \tag{2.3}$$

Shot noise on the other-hand, is a direct consequence of the discreteness of electric charge and results from the fact that the current is not a continuous flow but superposition of discrete pulses in time, each corresponding to the transfer of a single electron. The current through the conductor is a result of the superposition of single quanta of charge '*e*' emitted randomly in time. Its spectral density is proportional to the average current and is also characterized by a white noise like spectrum. Interestingly, Shot noise is absent in macroscopic, metallic resistors because of a smoothing of the current fluctuations that result from the discreteness of the electrons by inelastic electron-phonon scattering, leaving only thermal noise. But in small devices with dimensions comparable to the scattering lengths, fluctuations due to shot noise co-exist with thermal noise. Random events that are uncorrelated in time, as those of the arrival of single electrons into the conducing channel can be described by Poissonian statistics [32]. The mean squared value of shot noise current for such a process is given by

$$\left\langle I^2 \right\rangle_{Shot} = 2e\left\langle I \right\rangle \Delta f \tag{2.4}$$

Without loss of generality, it can be assumed that the current in a transistor channel switches from a 'zero' to a mean value '$\langle I \rangle$' upon sensing the absence of a single electronic charge. From equations 2.3 and 2.4, the total noise current in a bandwidth Δf due to Shot and Thermal noise in the high current state is given by

$$I_N = \sqrt{(4K_B T\,\Delta f)/R + 2e\langle I\rangle \Delta f} \tag{2.5}$$

The Signal to Noise Ratio can hence be written as

$$SNR = \frac{\langle I\rangle}{I_N} = \frac{\langle I\rangle}{\sqrt{(4K_B T\,\Delta f)/R + 2e\langle I\rangle\,\Delta f}} \tag{2.6}$$

Simplifying the above equation using the relation $\langle I\rangle = V_{DS}\langle G\rangle$ where V_{DS} is the applied source-drain voltage across the channel and $\langle G\rangle$ is the average conductance through the channel in the conducting state gives,

$$SNR = \frac{\langle I\rangle}{I_N} = \frac{\langle G\rangle V_{DS}}{\sqrt{(4K_B T\,\Delta f)\langle G\rangle + 2e\langle G\rangle V_{DS}\,\Delta f}} \tag{2.7}$$

Naturally, a large value of V_{DS} would result in a large Signal to Noise Ratio. With increasing V_{DS} and corresponding increase in the device current $\langle I\rangle$, the device operation would shift into the regime wherein fluctuations due to Shot noise dominate over Thermal fluctuations. This regime is reached when $2e\langle G\rangle V_{DS}\,\Delta f >> 4K_B T\langle G\rangle \Delta f$ or $V_{DS} >> 2K_B T/e$. In the Shot Noise regime, equation 2.7 can be further simplified and expressed as:

$$SNR = \frac{\langle I\rangle}{I_N} = \sqrt{\frac{\langle G\rangle V_{DS}}{2e\,\Delta f}} \tag{2.8}$$

Again without loss of generality, it can be supposed that the average channel conductance $\langle G \rangle$ in the conducting state is due to an unknown number of 'N_m' conducting modes in the channel, each contributing a conductance of e^2/h to channel. The conductance e^2/h = *1/13KΩ* is the well-known standard of conductance of an electron waveguide mode in a 1-dimensional channel. The origin of this quantized value of conductance is further elaborated in section 3.5. With this additional simplification equation 2.8 can now be recast as

$$SNR = \frac{\langle I \rangle}{I_N} = \sqrt{\frac{N_m\,(e^2/h)V_{DS}}{2e\,\Delta f}} = \sqrt{N_m}\sqrt{\frac{eV_{DS}}{2h\,\Delta f}} \qquad (2.9)$$

We consider below three geometries of an FET channel to further simply the above Signal to Noise Ratio expression.

2.3.1 FET Channel in the form of a Cylindrical Solid Conductor

A solid cylindrical conducting channel, like a semi-conducting Nanowire transistor, is an interesting channel geometry for estimating the ultimate limit of a charge sensor. As shown at the end of this section, the charge sensitivity can be expressed purely in terms of fundamental constants, with no dependence on actual device geometry. In the calculations that follow, it is assumed that an electron or an ion with a charge '*e*' can be favorably positioned at the center of the channel as shown in Figure 2.3. The Coulomb potential of the ion blocks the flow of current through the channel being driven by the external source drain voltage V_{DS}. To provide a general argument, the presence/absence

of this ion is assumed to switch off/on the channel current by 'N_m' conducting modes through the channel.

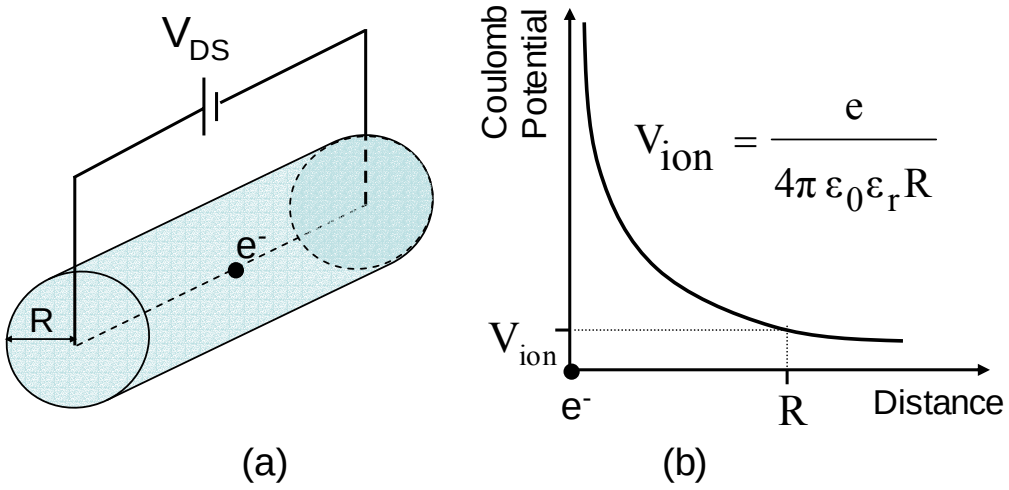

Figure 2.3: (a) FET channel in the form of 2D solid conductor with an immobile ion/electron placed at the center of the channel. (b) Ionic Coulomb potential roll off along the radius of the conductor.

First, the 2D density of states per unit area per eV for a solid wire estimated using running wave boundary conditions is equal to $dN = \frac{m_e}{\pi \hbar^2}$. The number of modes that would be available for conduction in a solid conductor of radius 'R' whose ends are held at a potential difference of V_{DS} is

$$N_m = \left(\frac{m_e}{\pi \hbar^2}\right)\left(\pi R^2\right) eV_{DS} \tag{2.10}$$

In the presence of an electronic charge in the conductor, the ionic Coulomb potential can prevent the propagation of a few available modes. In order to be able to completely

switch off the channel in the presence of the electronic charge, the maximum allowed source-drain voltage V_{DS} is simply equal to the minimum value of this ionic potential, the potential at the radius 'R' of the conductor. This sets the maximum limit on the source drain voltage that can applied across the channel and is given by

$$V_{DS} = e \Big/ 4\pi\varepsilon_0\varepsilon_r R \tag{2.11}$$

Thus, from equation 2.10, the number of modes in the conducting state that is switched off by a single electronic charge positioned in the 2D solid conductor is

$$N_m = \left(\frac{m_e}{\pi\hbar^2}\right)\left(\pi R^2\right)\left(\frac{e^2}{4\pi\varepsilon_0\varepsilon_r R}\right) = \left(\frac{m_e}{\hbar^2}\right)\left(\frac{e^2}{4\pi\varepsilon_0\varepsilon_r}\right)R \tag{2.12}$$

Substituting equations 2.11 and 2.12 in 2.9, we get the Signal to Noise Ratio as

$$SNR = \frac{\langle I \rangle}{I_N} = \sqrt{N_m}\sqrt{\frac{eV_{DS}}{2h\,\Delta f}} = \sqrt{\left(\frac{m_e}{2h\,B}\right)\left(\frac{e^2}{4\pi\varepsilon_0\varepsilon_r\hbar}\right)^2} \tag{2.13}$$

Equation 2.13 can now be recast in more interesting forms as shown below.

$$\mathrm{SNR} = \frac{\langle \mathrm{I} \rangle}{\mathrm{I_N}} = \sqrt{\left(\frac{\mathrm{m_e}}{2h\,\Delta \mathrm{f}}\right)\left(\frac{\mathrm{e}^2}{4\pi\varepsilon_0\varepsilon_\mathrm{r}\hbar}\right)^2} \qquad \text{(a)}$$

$$= \sqrt{\left(\frac{\mathrm{m_e}c^2}{2h\,\Delta \mathrm{f}}\right)\left(\frac{\mathrm{e}^2}{4\pi\varepsilon_0\varepsilon_\mathrm{r}\hbar c}\right)^2} \qquad \text{(b)}$$

$$= \sqrt{\frac{1}{2}\left(\frac{\mathrm{m_e}c^2}{h\,\Delta \mathrm{f}}\right)\alpha^2} \qquad \text{where } \alpha = \frac{\mathrm{e}^2}{4\pi\varepsilon_0\varepsilon_\mathrm{r}\hbar c} \text{ is the fine structure} \qquad \text{(c)}$$

$$= \sqrt{\left(\frac{\mathrm{R_y\,c}}{\Delta \mathrm{f}}\right)} \qquad \text{where } \mathrm{R_y} = \frac{\mathrm{m_e\,e}^4}{8\,\mathrm{c}\,(\varepsilon_0\varepsilon_\mathrm{r})^2 h^3} \text{ is the Rydberg in the channel} \qquad \text{(d)}$$

(2.14)

As seen from expression 2.14 (c), the maximum Signal to Noise Ratio in a measurement bandwidth Δf, is one-half the electron rest-mass energy in the channel times the fine structure constant squared divided by "h Δf". The maximum allowed measurement Bandwidth for detecting single electrons beyond which the Signal to Noise ratio degrades below unity is the value of the Rydberg in the conducting channel times the speed of light, $\Delta \mathrm{f} = \mathrm{R_y\,c}$.

For a 2D conducting cylinder made from Silicon, with an effective electron mass of about 0.2 x 9.1e-31 and a relative di-electric constant of 11.9, this bandwidth limit is about 4.5THz. The corresponding charge sensitivity or δQ_{min} is 4.6 x 10^{-7} e/$\sqrt{\mathrm{Hz}}$.

2.3.2 FET Channel in the form of a Quantum Point Contact

Here we consider the sensitivity limit of a more traditional FET geometry, namely the Quantum Point Contact Transistor that has become a very popular tool in mesoscopic

physics experiments. A Quantum Point Contact (QPC) is a constriction in a transistor channel with a width comparable to the Fermi wavelength of electrons in the channel where transport through the constriction becomes ballistic. A convenient way of creating a QPC is by electrostatic squeezing of the 2DEG in a modulation doped heterostructure by split gate electrodes as shown in Figure 2.4. The key feature in the transport through a Quantum Point Contact is the quantization of conduction in multiples of 'e^2/h' due the formation of 1D waveguide modes by the split gate electrodes. This transport phenomenon is discussed in more detail in section 3.5.

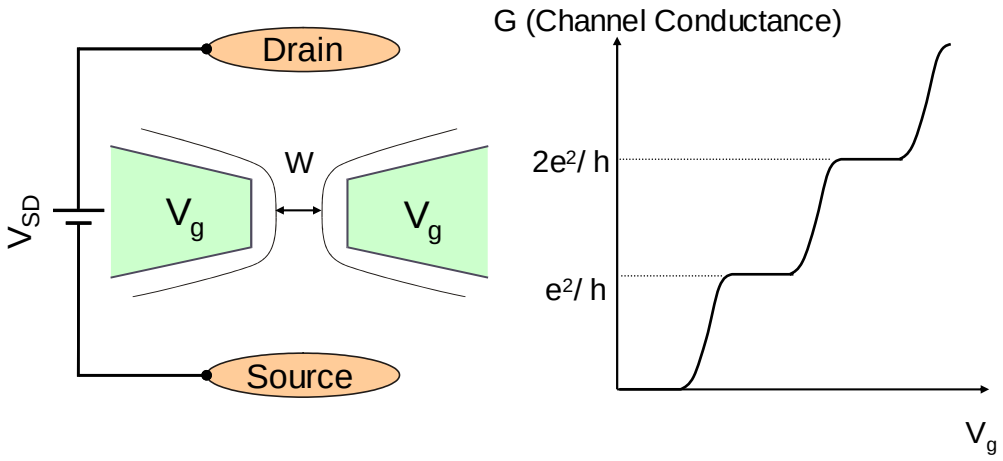

Figure 2.4: (a) Schematic of Quantum Point Contact Constriction (Width 'W') created by split-gate electrodes on the surface of a 2DEG sample (b) Quantization of conductance through the point contact.

In this section we estimate the sensitivity of a Quantum Point Contact with a width equal to just one Fermi wavelength so that each electron waveguide mode is constituted by the transport of one electron through the constriction. As in the previous case, the channel is

assumed to be completely pinched off in the presence of a single ionic charge in the transport path. One waveguide mode is assumed to be opened when it is absent and the conductance changes by one full quantum of e^2/h. The applied source-drain voltage is taken to be equal to the first sub-band spacing $\Delta_{\text{sub-band}}$ to support the transport of the added mode to the channel. Under these assumptions, the Signal to Noise Ratio expression in equation 2.9 becomes

$$\text{SNR} = \frac{\langle I \rangle}{I_N} = \sqrt{\frac{eV_{DS}}{2h\,\Delta f}} = \sqrt{\frac{\Delta_{\text{sub-band}}}{2h\,\Delta f}} \tag{2.16}$$

An estimate for $\Delta_{\text{sub-band}}$ can be made by using the energy level spacing for a particle in a box which gives $\Delta_{\text{sub-band}} = \frac{3\pi^2\hbar^2}{2m_e W^2}$ where 'W' is the width of the point contact. Substituting this value of Δ in the SNR expression of equation 2.16 we get

$$\text{SNR} = \frac{\langle I \rangle}{I_N} = \sqrt{\frac{3h}{16m_e W^2}\frac{1}{\Delta f}} \tag{2.17}$$

Equation 2.17 can be expressed in terms of the Rydberg and the Bohr radius in the channel material into the equation we get,

$$\text{SNR} = \frac{\langle I \rangle}{I_N} = \sqrt{\frac{3\pi^2}{2}\frac{R_y\,c}{\Delta f}\left(\frac{R_B}{W}\right)^2} \tag{2.18}$$

where $R_y = \frac{m_e e^4}{8c(\varepsilon_0\varepsilon_r)^2 h^3}$ is the Rydberg and $R_B = \frac{4\pi\varepsilon_0\varepsilon_r\hbar^2}{m_e e^2}$ is the Bohr radius in the channel material.

Hence in comparison to the case of the solid 2D conductor, the Bandwidth improves as

$$(R_B/W)^2\,,\ \Delta f \propto R_y\ c \left(\frac{R_B}{W}\right)^2 \qquad (2.19)$$

At this point, we would like to compare the performance of the QPC electrometer to that of a Single Electron Transistor, a sophisticated transistor geometry engineered to detect single electronic charges.

A Single Electron Transistor is essentially an FET in which the channel current is constituted by the transfer of single electrons from the source to the drain. The discrete transfer of single electrons is accomplished in a *"Source-Island-Drain"* geometry [30, 31] as opposed to a *"Source-Channel-Drain"* geometry of a FET. The *Island* constitutes a pool of electrons isolated by insulating tunnel barriers from the source and drain electrons. Similar to the FET, a gate electro-statically controls the total charge on the *Island*, that is supplied and removed through the Source and Drain.

As shown in equation 2.18, the maximum allowed bandwidth for the QPC improved as the (Bohr Radius / QPC Width)^2. Similar to the QPC, a limit for the SET can be derived as follows.

The level spacing in an Island of Radius 'R' is estimated from the 2D Density of States as,

$$\Delta E = \frac{1}{\text{DOS x Area}} = \frac{1}{\left(\frac{m_e}{\pi \hbar^2}\right)\left(\pi R^2\right)} = \frac{\hbar^2}{m_e R^2} \tag{2.20}$$

Analogous to the QPC, it is assumed that the presence/absence of a charge near the island switches off/on a Coulomb blockade resonance peak and the maximum allowed V_{SD} is taken equal to ΔE. Replacing $\Delta_{sub\text{-}band}$ by ΔE in the Signal to Noise Ratio expression of equation 2.16, we get

$$SNR = \frac{\langle I \rangle}{I_N} = \sqrt{\frac{\Delta E}{2h\,\Delta f}} = \frac{\hbar^2}{m_e R^2 \left(2h\,\Delta f\right)} \tag{2.21}$$

Equation 2.21 can be expressed in terms of the Rydberg and Bohr radius as

$$SNR = \sqrt{2\pi \frac{R_y\, c}{\Delta f} \left(\frac{R_B}{R}\right)^2} \tag{2.22}$$

Thus the SNR expression for the SET is very similar to that of the QPC expression in 2.16. Thus, a traditional Field effect Transistor in the form of a narrow skinny wire or a Quantum Point Contact transistor, is equally capable of detecting single electronic charges with the bandwidth of detection eventually being limited by fundamental constants.

2.3.3 FET channel in the form of a Cylindrical Hollow Conductor

We conclude this chapter by deriving the limit on the sensitivity of a 1D channel where the only allowed modes are peripheral modes like in a hollow Carbon Nanotube conductor. It is again assumed that an electron or an ion with a charge '*e*' can be favorably positioned in the channel in such a way that the presence/absence of this charge switches off/on the channel current by 'N_m' conducting modes.

The 1D density of states in *k*-space for modes along the periphery of the hollow conductor can be calculated using running wave boundary conditions as

$$dN = \left(\frac{2\pi R}{2\pi}\right) 2\, dk \tag{2.20}$$

Using the dispersion $E = \frac{\hbar^2 k^2}{2m_e}$ we get $dN = \left(\frac{R}{\hbar}\right)\sqrt{\frac{2m_e}{E}}\, dE$. Thus, the number of modes in an energy range defined by V_{DS} is

$$\begin{aligned} N_m &= \int_0^{eV_{DS}} dN = \left(\frac{R}{\hbar}\right)\sqrt{2m_e}\int_0^{eV_{DS}} \left(\sqrt{1/E}\right) dE \\ &= \left(\frac{2R}{\hbar}\right)\sqrt{2e\, m_e V_{DS}} \end{aligned} \tag{2.21}$$

simply equal to the minimum ionic potential, the potential at the radius 'R' of the conductor given by $V_{DS} = e/4\pi\varepsilon_0\varepsilon_r R$.

From equation 2.17, the number of channels that are switched off/on by a single electronic charge present in 1D hollow conductor is given by

$$N_m = \left(\frac{2R}{\hbar}\right)\sqrt{2m_e\left(\frac{e^2}{4\pi\,\varepsilon_0\varepsilon_r R}\right)} \tag{2.22}$$

Substituting equations 2.18 and 2.11 into 2.9, we get the Signal to Noise Ratio for the case of a hollow conductor as

$$SNR = \frac{\langle I\rangle}{I_N} = \sqrt{N_m}\sqrt{\frac{eV_{DS}}{2h\,\Delta f}} = \sqrt{\left(\frac{2R}{\hbar}\right)\sqrt{2m_e\left(\frac{e^2}{4\pi\,\varepsilon_0\varepsilon_r R}\right)^3}\left(\frac{1}{2h\,\Delta f}\right)} \tag{2.19}$$

Upon further simplification equation 2.19 can be expressed in the following forms:

$$SNR = \frac{\langle I\rangle}{I_N} = \left(\frac{1}{\Delta f}\sqrt{\alpha^2\left(\frac{2m_e c^2}{h^2}\right)\left(\frac{e^2}{4\pi\,\varepsilon_0\varepsilon_r R}\right)}\right)^{1/2} \quad \text{where } \alpha \text{ is the fine structure constant}$$

$$= \left(\frac{2}{\Delta f}\sqrt{R_y\,c\left(\frac{1}{h}\frac{e^2}{4\pi\,\varepsilon_0\varepsilon_r R}\right)}\right)^{1/2} \quad \text{where } R_y \text{ is the Rydberg in the conducting channel} \tag{2.23}$$

Equation 2.20 can be recast in terms of the Bohr radius 'R_B' in the conducting material as

$$SNR = \left(\frac{2}{\Delta f}\sqrt{\frac{R_y}{(2\pi)}\frac{\hbar\,c}{m_e}\left(\frac{1}{R_B R}\right)}\right)^{1/2} \quad \text{where } R_B = \frac{4\pi\,\varepsilon_0\varepsilon_r\hbar^2}{m_e e^2} \text{ is the Bohr radius in the channel} \tag{2.24}$$

Thus the SNR for the present case of a 1D hollow conductor with peripheral modes is dependent on the Radius of the conductor, although weakly as $(1/R)^{1/4}$.

CHAPTER 3 Photo-detector Implementation

3.1. Choice of semiconductor materials

The distribution of quantum entanglement over long distances using single photons requires a single photon photo-detector with a capability to accomplish the transfer of photon polarization information directly to the photo-excited electron spin. A detector with just single photon sensitivity is not enough. It is crucial to transfer quantum information from photon spins to electrons spins to allow for storage and necessary quantum logic operations required in the implementation of the teleportation algorithm illustrated in Figure 1.2 and Figure 1.3. Optical selection rules have now been well-established in high-optical efficiency III-V semiconductor heterostructures that permit the transfer of photon polarization information to photo-electron spin [33]. The key guiding principle for the coherent transfer of information from photons to electrons in semiconductors is that the 'g-factor' which controls the Zeeman energy splitting of spin degenerate levels can be engineered similar to the more common practice of semiconductor band-gap engineering creating novel heterostructure devices. There is a whole range of III-V semiconductor heterostructure compositions and strains that can create a rich variety of g-factor engineered devices for coherent photo-detection [34]. We have thus chosen to implement the single photon detector for Quantum Repeaters in engineered III-V heterostructures, which could eventually be integrated onto a SiGe technology to leverage on the long (~60msec) T_2 electron spin decoherence lifetimes in Silicon [35], useful for storage and computation on single electron spins. It has already

been experimentally observed that electrons can be coherently transferred across hetero-interfaces preserving spin information [36, 37]. Single Photon detection experiments in two material systems will be discussed in this thesis, namely the AlGaAs/GaAs and the InAlAs/InGaAs heterostructures both of which have the potential for the development of a Spin Coherent Single Photon Detector [33].

The devices in both the material systems were fabricated in modulation-doped heterostructures grown epitaxially on semi-insulating substrates by Molecular Beam Epitaxy. Modulation-doped heterostructures readily provide a confined 2-dimensional sheet of electrons at the hetero-junction of the semi-conducting materials. This sheet charge can be further confined by electrostatic squeezing using negatively biased electrodes, thus providing a means of artificially creating lower dimensional structures such 1-D Quantum Wires and 0-D Quantum Dots. These nanostructures form the basic building blocks of the photo-detector that will be described in this thesis. The following sections first describe the hetero-layers make-up of the epi-wafers used to fabricate the devices for photo-electron trapping, storage and detection.

3.2. *AlGaAs/GaAs* Heterostructure

A very well-studied and common semiconductor heterostructure is that of the ternary III-V compound $Al_yGa_{1-y}As$. $Al_yGa_{1-y}As$ with $y \leq 0.3$ is lattice matched to GaAs. Further, the thermal expansion coefficients of the two materials are identical resulting in an almost perfect interface between the two materials. However, the band gap of GaAs is

1.4eV and that of $Al_{0.3}Ga_{0.7}As$ is 1.7eV at room temperature with 60% of the difference taken up by the conduction band energies. This band gap difference between the two materials can be put to practical use and the possibility of band gap engineering makes this system very attractive for a variety of novel electronic and optoelectronic applications.

For a detailed study of semiconductor band-gap engineering, the reader is referred to texts on modern semiconductor devices such as [38]. A brief description of modulation doping in band-gap engineered devices is provided here. A Modulation doped Field Effect Transistor (MODFET) is a specially designed heterostructure device achieving a very high mobility channel through band-gap engineering. In such a transistor, also commonly known as a High Electron Mobility Transistor, a spatial separation between the mobile electrons and the ionized donors is accomplished by an intrinsic spacer layer. Figure 3.1 shows the basic device structure of a MODFET.

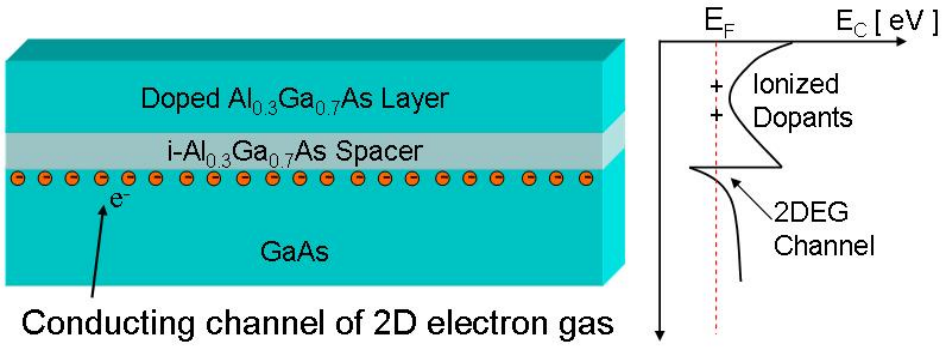

Figure 3.1: Modulation doping in a Field effect transistor and associated conduction band diagram. The band offset between AlGaAs and GaAs results in a confined

two-dimensional electron gas (2DEG) at the heterointerface. The spacer layer reduces dopant scattering leading to high channel mobilities.

In a modulation doped AlGaAs/GaAs heterojunction transistor, the dopants reside in the barrier AlGaAs layer. Due to the conduction band offsets between AlGaAs and GaAs, a triangular potential well is formed at the hetero-interface as shown in Figure 3.1. Electrons from the donors in the AlGaAs layer drop down into the GaAs layer and remain trapped in the potential well. These electrons become confined in the growth direction but remain free to move about in the plane of the hetero-interface. This gives rise to a 2-dimensional sheet charge or a 2-Dimensional Electron Gas (2-DEG) at the interface. The un-doped spacer layer between the doped AlGaAs and GaAs also reduces scattering by ionized dopant potentials resulting in extremely high mobilities for the channel electrons. Mobilities as high as 10^7 cm^2/V-sec have been observed in modulation doped transistors at low temperatures.

The AlGaAs/GaAs epitaxial layer structure and the associated band diagram of the wafer used in our experiments (henceforth identified as GO3) are shown in Figure 3.2. The layer sequence, on top of a semi-insulating GaAs substrate, consists of an un-doped GaAs buffer layer, an i-$Al_{0.3}$ $Ga_{0.7}As$ spacer layer 30 nm thick, a Silicon doped n-$Al_{0.3}Ga_{0.7}As$ layer 60 nm thick and a Silicon doped GaAs cap layer 5 nm thick.

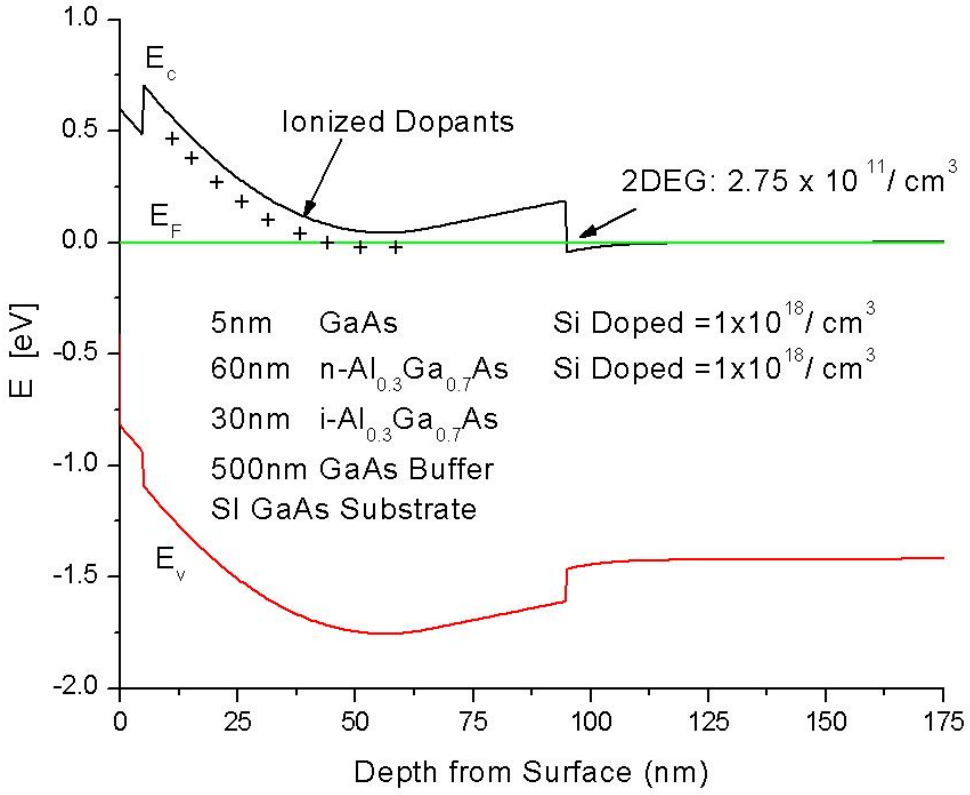

Figure 3.2: AlGaAs/GaAs 2DEG heterostructure and simulated energy band diagram for zero voltage bias on the surface at 1.4K.

Due to the band offsets, the 2-Dimensional Electron gas is formed at the interface of the i-AlGaAs spacer layer and the undoped GaAs buffer layer. Figure 3.3 presents the Shubnikov-de Haas oscillations and the Quantum Hall measurement data taken on G03 at 1.4K. The 2DEG density and mobility, calculated from the observed oscillations is 2.75 $x10^{11}/cm^2$ and 262,000 cm^2/V-sec respectively.

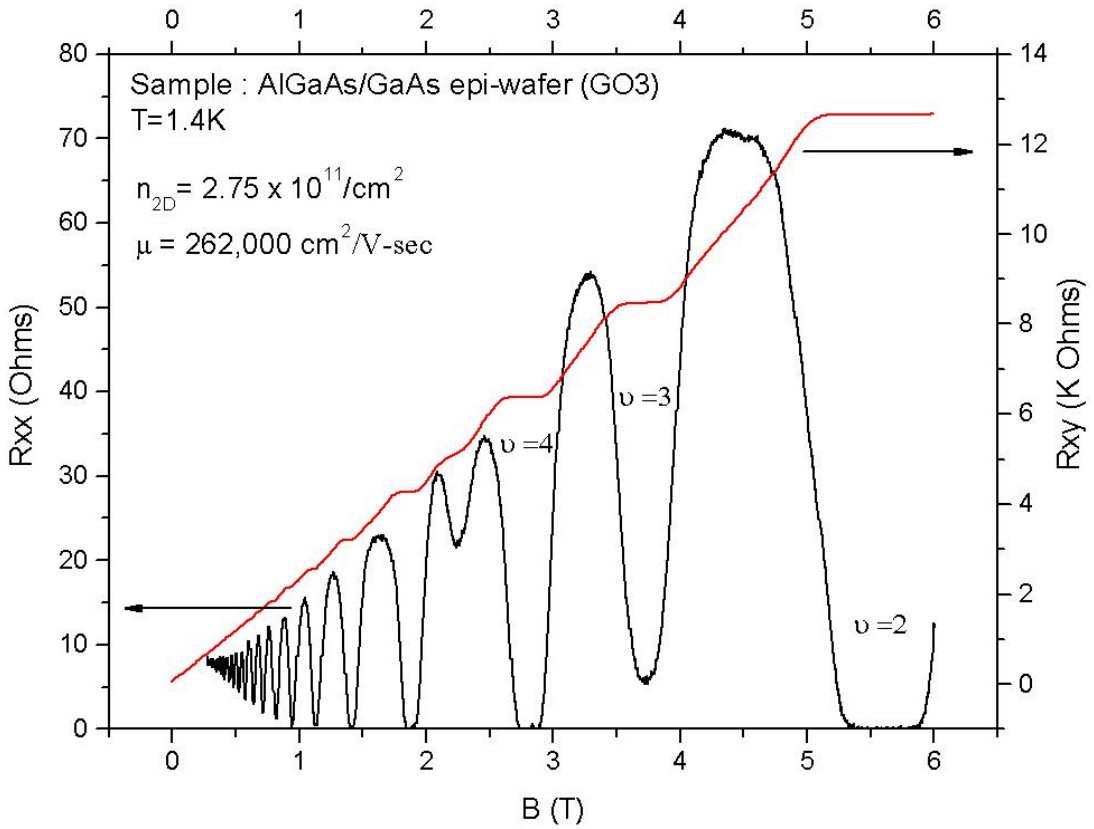

Figure 3.3: Shubnikov-de Haas oscillation and Quantum Hall measurements on AlGaAs/GaAs heterostructure sample (G03).

3.3. *InAlAs/InGaAs* Heterostructure

Apart from the simple and conventional AlGaAs/GaAs heterostructure described in the previous section, devices were also fabricated and characterized in a more sophisticated heterostructure built in InAlAs/InGaAs material system. InGaAs provides the added advantage of operating in the low-loss 1.3μm/1.55μm fiber window that would enhance the operating data rate for sharing entangled EPR pairs over the tele-communications channel.

The epi-layer sequence consisted of a nominally un-doped 100nm thick InP buffer layer, an un-doped $In_{0.52}Al_{0.48}As$ buffer layer 1000nm thick, a Si-doped ($5x10^{17}/cm^3$) n-$In_{0.52}Al_{0.48}As$ layer 10nm thick, an i-$In_{0.52}Al_{0.48}As$ lower spacer layer 30nm thick, an i-$In_{0.53}Ga_{0.47}As$ channel layer 10nm thick, an i-$In_{0.52}Al_{0.48}As$ barrier layer 20nm thick, an i-InP cladding layer 10nm thick, an i-$In_{0.53}Ga_{0.47}As$ absorption layer 4.5nm thick, an i-InP cladding layer 10nm thick, an i-$In_{0.52}Al_{0.48}As$ capping layer 60nm thick. All layers were grown by gas source molecular beam epitaxy on Fe-doped semi-insulating InP substrate.

The higher band-gap barrier layers for the heterostructure were formed by $In_{0.52}Al_{0.48}As$, lattice matched to $In_{0.53}Ga_{0.47}As$. $In_{0.52}Al_{0.48}As$, has a larger conduction band offset with $In_{0.53}Ga_{0.47}As$ of 0.5eV, as opposed to the 0.23eV offset between the more conventional lattice matched InP/$In_{0.53}Ga_{0.47}As$ system [39]. The higher band offset material was chosen to reduce leakage of trapped electrons from the upper photo-absorption $In_{0.53}Ga_{0.47}As$ quantum well to the lower $In_{0.53}Ga_{0.47}As$ quantum well containing the channel electrons obtained by modulation doping. Further, $In_{0.52}Al_{0.48}As$ helps in the formation of low-leakage metal Schottky contacts required in the formation of gate electrodes. The upper i-$In_{0.53}Ga_{0.47}As$ photo-absorption quantum well is sandwiched between 10nm thick InP cladding layers to achieve an effective zero electron g-factor in the upper quantum well. A small electron g-factor and a large hole g-factor accomplishes the transfer of photon polarization information perfectly to electron spin polarization without any entanglement with the hole spins [33]. InGaAs has a negative electron g-

factor of -4.5, while InP has a positive g-factor of +1.2. Sandwiching a thin layer of InGaAs between InP layers, results in the trapped electron wavefunction sampling negative and positive g-factor materials, thus enabling the accomplishment a net effective g-factor of zero with suitable layer thickness [40]. The energy band diagram of the heterostructure, simulated by a 1-dimensional self-consistent Schrödinger-Poisson equation solver is shown in Figure 3.4.

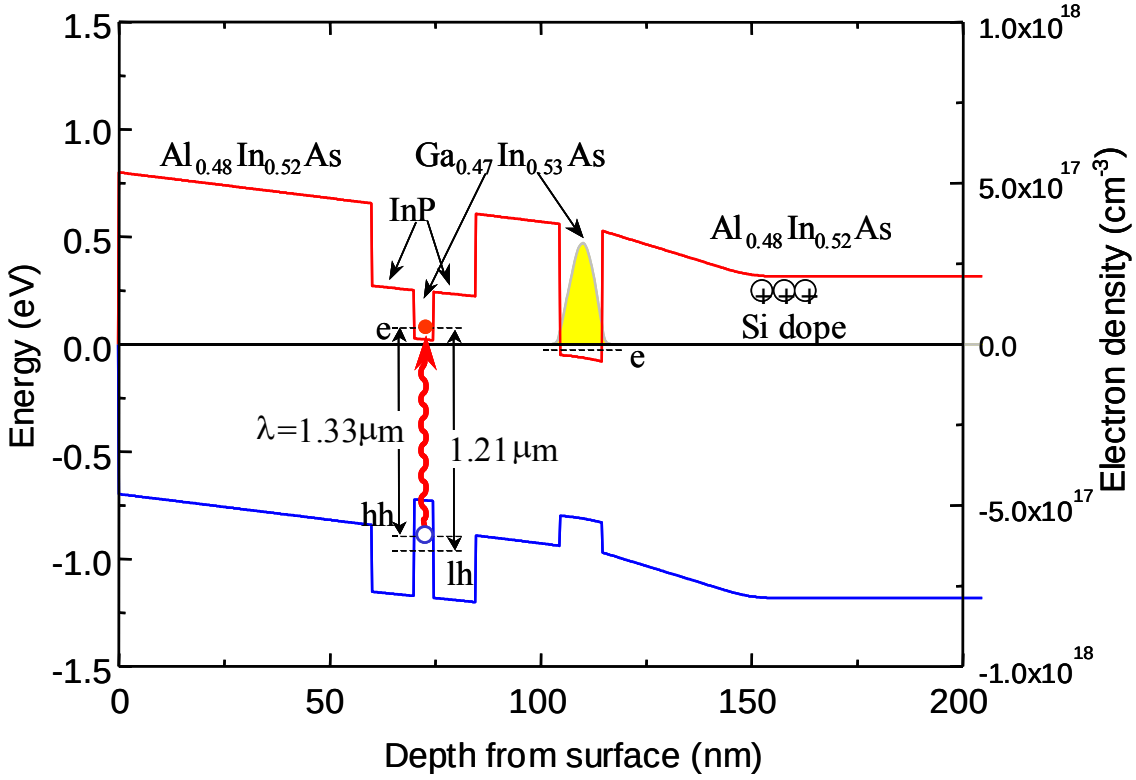

Figure 3.4: Simulated Energy-band diagram of the double-QW InAlAs/InGaAs heterostructure for single photon detection at trapping at 1.3μm. The $In_{0.53}Ga_{0.47}As$ QW closer to the surface is designed to accomplish inter-band absorption in the 1.3μm low-loss fiber window, while at the same time accomplish a zero electron g-factor desired for the coherent transfer of quantum information to photo-excited

electron spin states. The lower $In_{0.53}Ga_{0.47}As$ QW is designed to confine the 2-dimensional electron gas forming the channel of the charge sensing field effect transistor.

3.4. Gate Electrode Geometry

The basic elements of a non-invasive Single Photon Detector are a potential trap (Quantum Dot) for photo-excited carriers, preferably an artificially created trap, and a skinny FET channel whose electron density can be modulated by the Photo-conductive Gain mechanism. We have implemented these low dimensional structures by electro-statically squeezing the electron gas in the modulation doped heterostructure samples with gate electrodes fabricated by e-beam lithography on the heterostructure surface. A detailed description of the fabrication procedure will be provided in the next chapter. A Scanning Electron Micrograph showing the layout of the two key elements is shown in Figure 3.5.

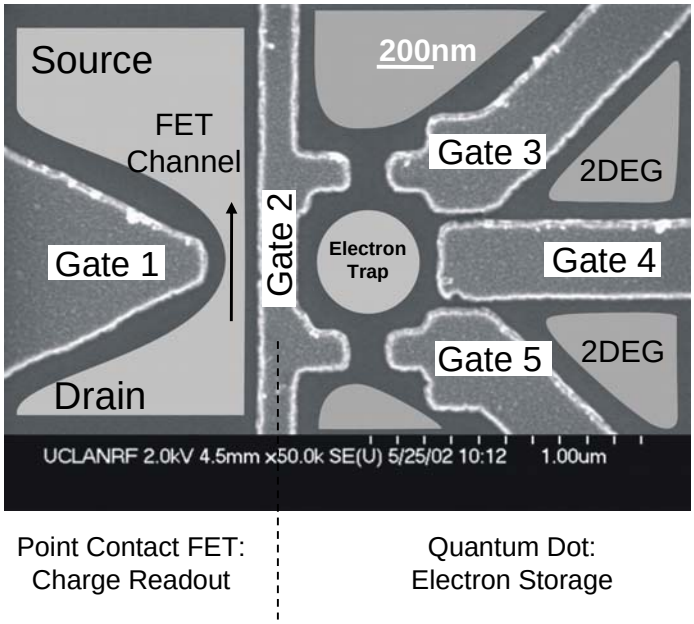

Figure 3.5 Device Layout for photon detection and capture of associated photo-excited electron. SEM shows fabricated Gate electrodes on the surface of a modulation doped heterostructure sample containing a 2D Electron Gas (2DEG) at the hetero-interface. The false coloring in the regions between the gates shows the electro-statically squeezed 2DEG by negatively biased gates.

As illustrated in Chapter 2, a conventional narrow channel field effect transistor is very capable of measuring single charges. A convenient method of creating highly sensitive small FET is by a split-gate technique on the surface of a modulation doped high mobility 2-dimensional electron gas heterostructures. In Figure 3.5, the narrow channel of the charge sensing FET is defined at the constriction between gate electrodes 1 and 2. This constriction having a width comparable to the Fermi wavelength of electrons in the channel is popularly known as a Quantum Point Contact. The essential features of transport through such a small Point Contact FET relevant to this dissertation have been

discussed in section 3.5. The central gate electrode (Gate 2) serves to isolate the Quantum Dot from the channel of the FET. The potential well of the Quantum Dot for trapping and storing photo-injected electrons is created between negatively biased gate electrodes 2, 3, 4 and 5. A major advantage towards using such artificial gate defined quantum dots as opposed to self-assembled quantum dots, is that the potential well can be controllably emptied and prepared before the arrival of single photons over the channel.

3.5. Quantum Point Contact (QPC) Transistor

A QPC is split-gate transistor on the surface of a modulation doped heterostructure with gate spacing comparable to the Fermi wavelength of electrons in the 2DEG. The QPC transistor has evolved over the past two decades as a very basic device for studying transport phenomena at the nanoscale [41, 42]. In the set of experiments that will be presented in this dissertation, the QPC transistor has been used to non-invasively sense the charge state of the quantum dot used to trap photo-injected charges. In the AlGaAs/GaAs 2DEG devices, a lateral QPC geometry has been utilized, while in the more sophisticated InAlAs/InGaAs 2DEG devices with two quantum wells, a vertical geometry in which the QPC channel is defined below the Quantum Dot.

To bring forth the essential features of transport through QPCs relevant to this dissertation, a brief discussion on point contacts in semiconductor heterostructures is provided below. Transport through QPCs and Quantum Dots is currently a very rich field

of study in mesoscopic physics and is being actively pursued by many research groups; a comprehensive review of the field can be found in [43].

Point Contacts in semiconductor devices such as FETs are short narrow constrictions in the electron channel with dimensions comparable to the mean free path of electrons in the channel. The characteristic length scale L, is much shorter than or comparable to the electron phase coherence length L_p, enabling the study of coherent processes in electron transport. Accessing this transport regime in semiconductors had remained elusive, till recent advances in nanofabrication techniques and high-quality epitaxial growth of semiconductor heterostructures. In a classical conductor like a long-channel FET, the electrons are randomly scattered during transport due to interactions with phonons and ionized impurities. Scattering randomizes the electron transport path in the channel, and sets an upper limit on mean scatter-free transport length in the channel. This inherent random scattering, results in a saturation of the drift velocity given by channel mobility times the electric field. With the advances in nanofabrication techniques, it has become possible to fabricate and study conductors with length scales shorter than the mean scattering length, a regime where electron transport becomes 'ballistic' and both quantum and classical effects play important roles. In high electron mobility semiconductor samples (~ 1 x10^6 cm^2/V-sec) the mean scattering length at low temperatures (<4.2K) can be larger than 10μm, making it relatively simple to fabricate 'ballistic' Quantum Point Contacts with length scales shorter than the scattering length in conventional field effect transistors.

A characteristic feature of ballistic electron transport is the quantization of channel conductance in steps of $2e^2/h \sim 1/13K\Omega$ [44,45], the factor of 2 arising due to the spin degenerate transport in the absence of an external magnetic field.

Figure 3.6 shows the conductance of a ballistic conductor versus voltage on the two split-gate electrodes which define a point contact transistor. The I-V_g measurement presented in Figure 3.6 is taken at 400mK on a device with a split-gate spacing of 250nm defined by e-beam lithography on the AlGaAs/GaAs heterostructure described in section 3.2. The relevant 2DEG parameters of the wafer, are as follows. The experimentally measured mobility μ of the 2-DEG is 262,000 cm^2 /V-sec (**Figure 3.3**). This corresponds to a mean scattering time of 10ps given by $\tau = m^* \mu / e$ where m^* =0.067 x 9.1e-31 is the effective electron mass in GaAs. The velocity of electrons at the Fermi energy V_f is given by $hk_f / 2\pi m^*$ where k_f is the Fermi wave-vector given by $\sqrt{2\pi n}$ for an electron density of '*n*' in the 2-DEG. This gives a Fermi velocity of 2.27 x 10^5 m/sec corresponding to a scattering length $l_e = V_f \tau = 2.27\mu m$. The Fermi wavelength λ_f is given by $2\pi / k_f$ and corresponds to ~ 48 nm. The spacing between the gates of 250nm defined by electron beam lithography achieves the conditions for the observation of conductance quantization in a ballistic conductor.

In Figure 3.6, as the gate voltages are made increasingly negative, the width of the channel decreases and the electron momentum in the direction perpendicular to the

transport takes on discrete quantized values analogous to the quantization due to spatial confinement in the growth direction. In the transport direction, the electron momentum takes on continuous values giving sub-bands of energies with a one-dimensional density of states.

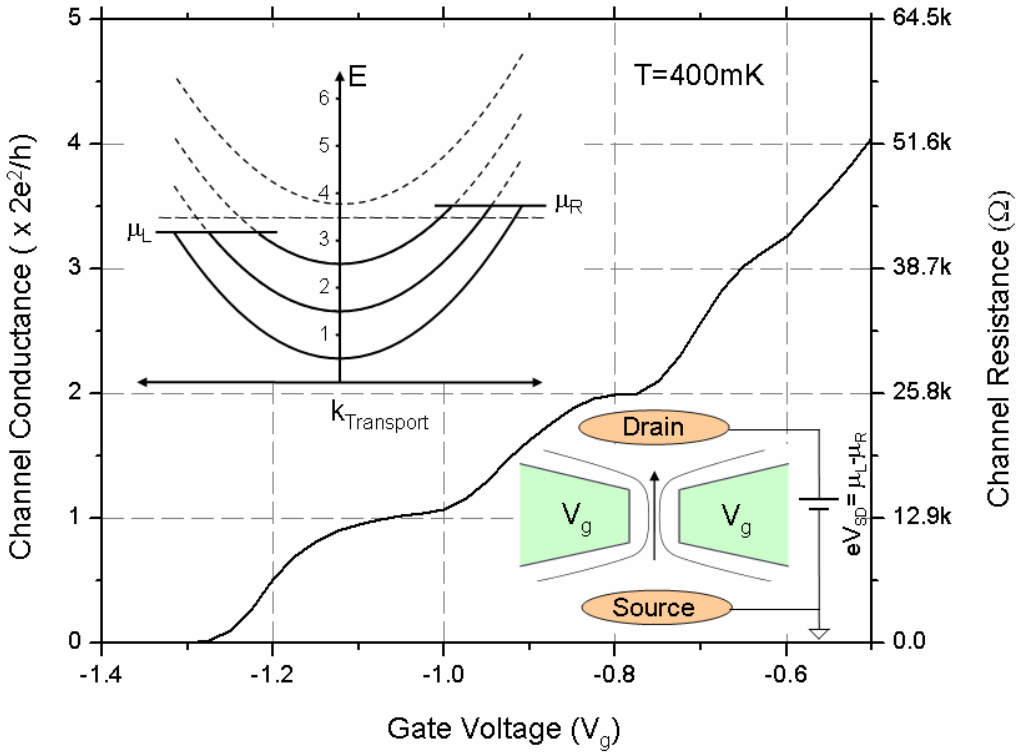

Figure 3.6: Quantized Conductance values of a ballistic conductor in the form of a split-gate Quantum Point Contact. As the gate voltage is made increasingly negative, the width of the point contacts decreases and the number of propagating modes at the Fermi level decreases stepwise due to the successive removal of 1-D energy sub-bands as shown in the top inset. Every propagating mode contributes a channel conductance of $2e^2/h$.

The sub-band energies increases as the gate voltage becomes increasingly negative and the sub-band closest to the Fermi level gets depopulated. As the width is continuously narrowed, the levels successively depopulate and the conductance of the one-dimensional channel decreases in steps of $2e^2/h$ (1/12.9KΩ) with the factor of 2 arising due to spin. This step-wise decrease can also be thought of as due to the successive removal of "electron wave-guide modes" from the channel with each mode contributing a resistance 12.9KΩ.

A simple derivation for the origin of the quantum of resistance is as follows. This derivation is due to Prof. Supriyo Datta of Purdue University. The current through a conductor can be expressed as the electronic charge **'e'** times the frequency **'γ'** at which the electrons are being shared across the ends of the conductor.

$$\mathbf{I = e\,\gamma}$$

Now, in a ballistic conductor where the electron transport is perfectly adiabatic, there is no energy lost in the channel. The number of electrons that are transported per second across a conductor whose ends are held at a potential difference **V** can simply be expressed as $\gamma = \frac{\mathbf{e}V}{h}$. This simple insight gives the conductance of a single mode ballistic channel as

$$G = \frac{I}{V} = \frac{e^2}{h}$$

or $2e^2/h$ for spin degenerate channel. An important aspect of ballistic transport is the independence of conductivity on the number of electrons in the channel and the geometry

of the split gate. Conductance in this regime purely depends on the number of occupied sub-bands.

CHAPTER 4 Device Fabrication

This chapter presents the processing steps leading to the fabrication of the devices in the AlGaAs/GaAs and InAlAs/InGaAs epi-wafers described in the previous chapter. The AlGaAs/GaAs wafer was obtained from IQE Inc., PA and the InAlAs/InGaAs wafer was grown at NEC Research Corporation, Japan. The devices were fabricated in the Nanoelectronics Research clean room facility at UCLA.

The fabrication process consisted of the following key steps. Details about each of the steps will be given in the sections that follow.

Step 1: *Mesa Etching for device isolation* (Photo-lithography + Wet Etching).

Step 2: *Alloyed Ohmic Contact Formation* (Photo-lithography + e-beam evaporation + Rapid Thermal Annealing).

Step 3: *Schottky Gate electrodes Formation* (e-beam Lithography + e-beam evaporation).

Step 4: *Bonding pads deposition for wire-bonding* (Photo-lithography + e-beam evaporation).

Step 5: *Opaque Metallic Photo-Mask deposition over device active area* (Photo-lithography + e-beam evaporation).

Step 6: *Aperture creation in Photo-Mask* (e-beam Lithography + Metal Dry Etching).

Step 7: *Deposition of Photo-Mask grounding interconnect* (Photo-lithography + e-beam evaporation).

Step 8: *Chip-level basic electronic device performance testing at room temperature.*

Step 9: *Packaging and wire-bonding individual devices for low temperature characterization.*

(Steps 5 through 7 are specific to AlGaAs/GaAs devices and were not part of the process flow in the fabrication of InAlAs/InGaAs devices)

Figure 4.1 shows the top-view and cross-section view of the final fabricated devices.

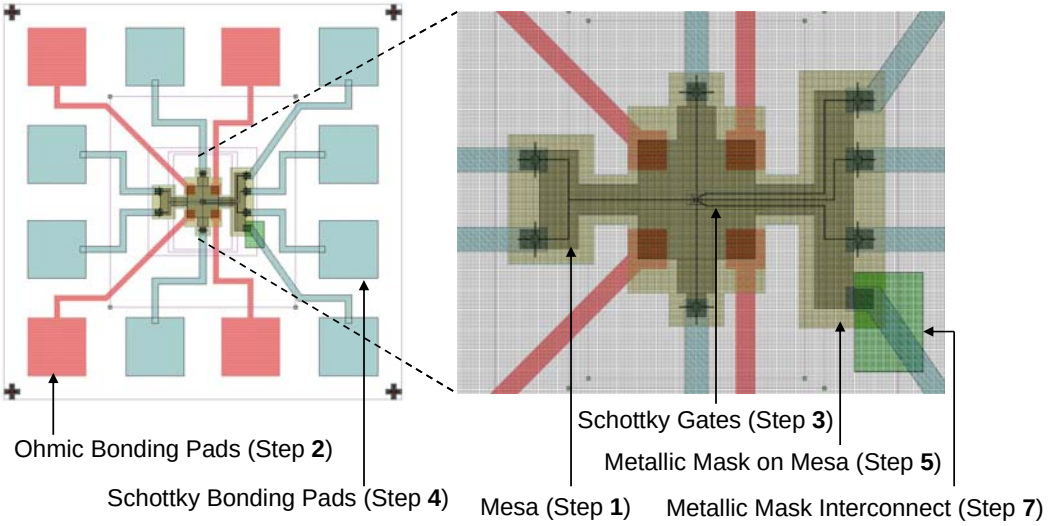

(a)

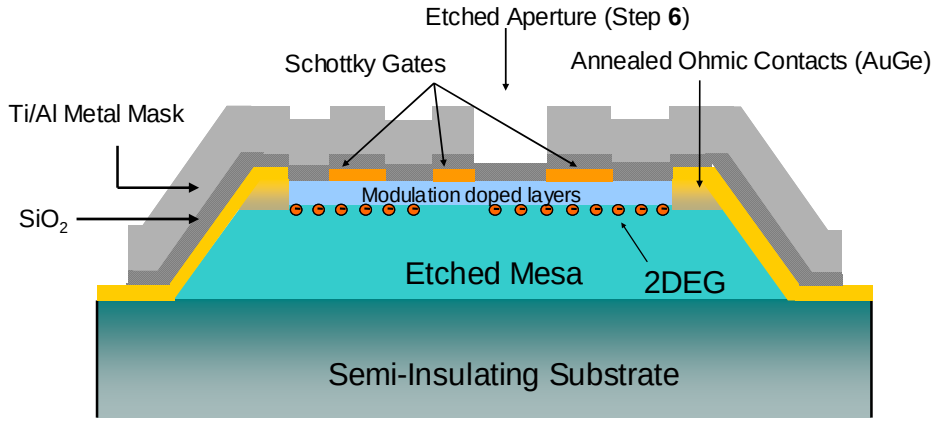

(b)

Figure 4.1: (a) Mask Level Device Layout (LEDIT Software pattern) and (b) Schematic device cross-section

4.1. Mesa etching for trench Isolation

Devices were processed on chips of dimensions ~1cm x 1cm, cleaved from the 3-inch epi-wafers. The cleaved chips were first cleaned using a three solvent degreasing procedure in *Acetone* followed by *Methanol* followed by *Isopropyl Alcohol* for 3 min in each solvent and rinsed in running DI water for 5 min. Organic solvents are extremely effective in removing oils, greases, waxes and organic material. Devices were formed as mesas isolated by trenches etched upto the semi-insulating substrate by a wet chemical etching process.

Wet chemical etching proceeds through either "Diffusion limited" or "Reaction limited" mechanisms that determine the final etch rate, etch profile and surface morphology. Diffusion limited etchants tend to be more isotropic with respect to crystal orientation, while reaction limited etchants tend to be highly anisotropic in selectively etching crystal planes through masking patterns. In a non-planar process such as ours, an anisotropic etching profile is very crucial to achieve mesa step-coverage of deposited metal stacks in subsequent processing steps. The Silicon processing industry overcomes this problem through Chemical Mechanical Polishing (CMP) of the surface of a partially processed wafer to achieve a high degree of global planarization. CMP of III-V materials on the other hand, is a very risky process, due to their excessive brittleness compared to Silicon. In order to maintain a high yield and reduce processing steps, we rely on the anisotropic

etching properties of the wet chemical etchants to obtain the angled side walls in specific crystallographic directions of etched mesas that is needed to achieve the desired step-coverage of deposited metallic contacts.

Fortunately, the Zinc-Blende crystalline structure of III-V materials such as GaAs, InAs and InP based compounds leads to anisotropic etching in almost all cases. The anisotropy results from the lack of symmetry in the lattice and dependence of etch rate on crystal orientation [47]. Figure 4.2 shows the etched side-wall profile of the InAlAs/InGaAs wafer etched in a Phosphoric acid based etchant. The wafer was grown on a (100) substrate which is by far the most commonly used wafer orientation for device fabrication. (100) wafers have two natural cleavage directions perpendicular to each other. These are the {110} planes identified by the primary and secondary flats along the wafer edges. Devices were oriented with mesa edges along these directions while patterning using photo-lithography. Step coverage for the metallic electrodes was achieved along the [**0 1 $\bar{1}$**] direction.

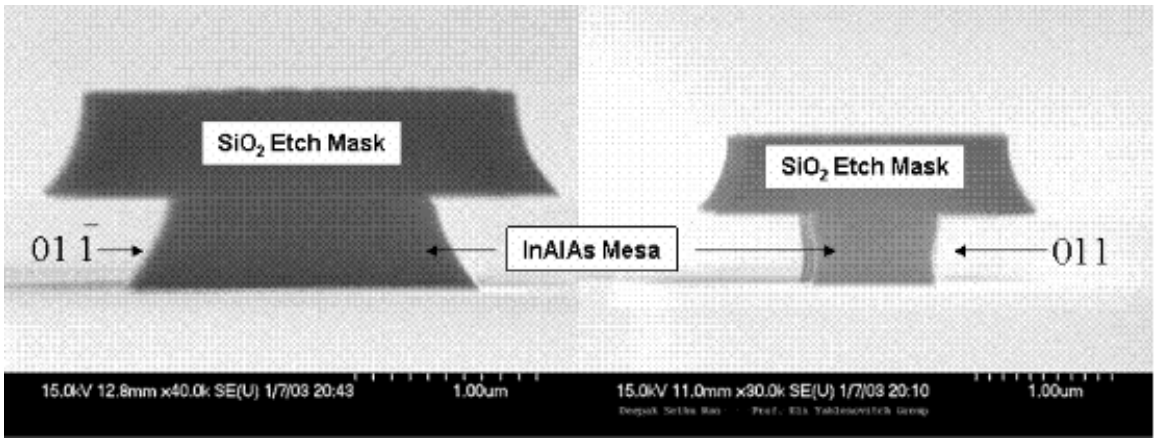

Figure 4.2: Anisotropic Wet Etching of III-V semiconductors achieves the angled side-wall profile needed for metal step-coverage.

Patterning for mesa formation was done using positive photo-resist AZ5214E-IR by UV photo-lithography using standard contact printing through a chrome mask. The basic pattern transfer process following a solvent degreasing and cleaning step are shown in Figure 4.3.

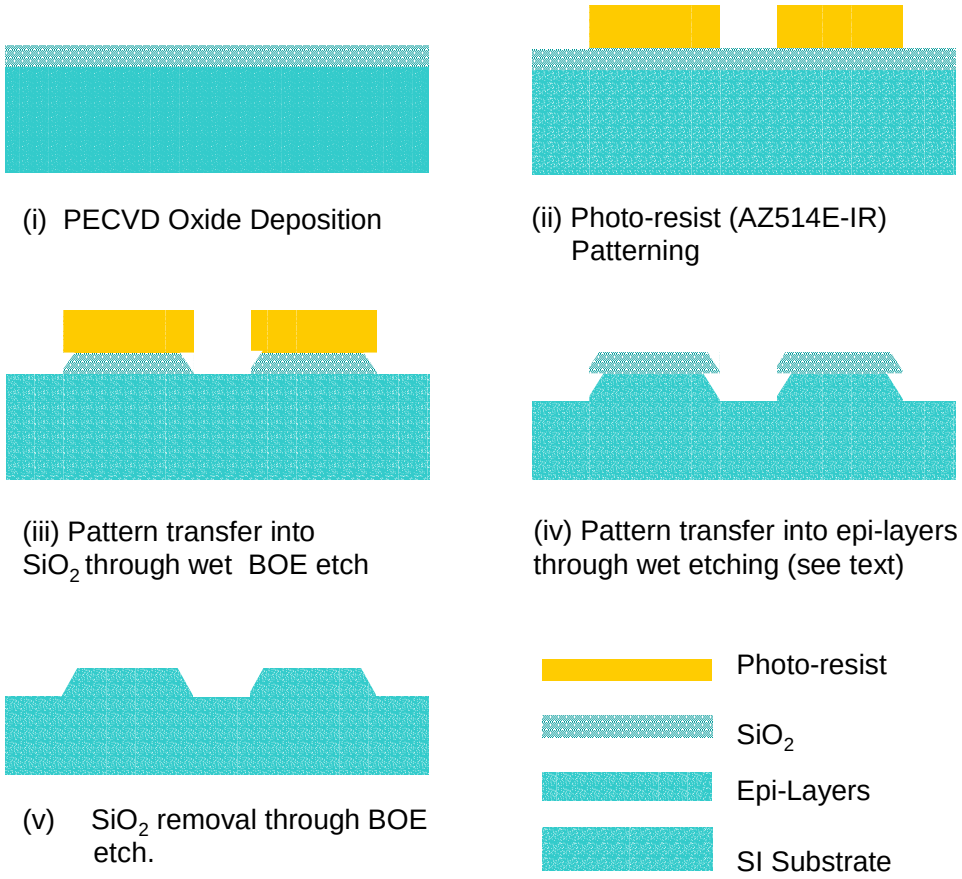

Figure 4.3: Wet etching pattern transfer process for Mesa isolation.

Step (i): Etch Mask Deposition: A layer of 500Å thick SiO_2 deposited through PECVD is used as an etch mask layer. Although plain photo-resist can also be used as mask layer for etching, SiO_2 was found to be more robust to the treatment of a variety of acids and prevented surface pitting on top of mesas, particularly in the etching of InAlAs/InGaAs wafers.

Step (ii) & Step (iii): Photo-lithography and pattern transfer into SiO_2:

Photo-resist AZ5214E-IR was coated on the sample through a two-step spinning process at 500rpm and 5000rpm for 5sec and 30sec respectively (~1.4μm thick resist); Prior to spinning the resist the sample was exposed to vapors of a adhesion promoter (HMDS-Hexamethlydisilazane) for 10 min to promote the adhesion of photo-resist to the surface of SiO_2. The resist is soft-baked at 105°C for 80 sec and exposed through the photo-mask at λ = 305nm, 8mW for 14sec. The exposed regions of the resist were developed in a 1:4 mixture of AZ400K:H_2O for 45 sec. Residual photo-resist in the developed regions was removed in an O_2 Plasma etcher operating at 200W for 2 min. The resist pattern was transferred into SiO_2 through a wet etch in BOE and the photo-resist removed through the standard solvent cleaning process using Acetone/Methanol/IPA and DI water;

Step (iv): Wet Chemical Etching

Wet etching proceeds by first oxidizing the surface of the semiconductor and then dissolving the oxide. Hydrogen Peroxide is used as the oxidizer in our etch mixture and the acid acts as the dissolving agent. The etching was performed at room temperature.

The table below gives the chemical etchants used to finally transfer the mesa patterns into the heterostructure epi-layers.

InAlAs/ InGaAs Heterostructure (Figure 3.4**)**			
Etch Mixture	*Etch Stop layer(s)*	*Etched Layer(s)*	*Etch Rate(300K)*
H_3PO_4:H_2O_2:H_2O (1ml: 4ml: 45ml)	InP	$In_{0.52}Al_{0.48}As$ (Barriers, Spacer and Buffer)	120nm/min
HCl:H_2O (20ml: 10ml)	$In_{0.52}Al_{0.48}As$ $In_{0.47}Ga_{0.53}As$	InP (Cladding Layers)	25nm/sec
HBr:H_2O_2:H_2O (20ml :0.2ml :20ml)	----	InP (Buffer)	2000nm/min
AlGaAs/ GaAs Heterostructure (Figure 3.2**)**			
H_2SO_4:H_2O_2:H_2O (1ml : 8ml : 100ml)	----	AlGaAs Barrier and GaAs Buffer	500nm/min

Table 4.1: Wet Chemical Etchants for etching Mesas in GaAs and InAlAs wafers.

The AlGaAs/GaAs heterostructure (G03) was etched in a mixture of H_2SO_4: H_2O_2: H_2O::1:8:100 for 2 min at an etch rate of ~500nm/min. The double quantum well InAlAs/InGaAs wafer (layers detailed in Figure 3.4) was etched using a combination of three etchant mixtures described in Table 4.1. Although the HBr solution is capable of

etching all the layers in the heterostructure namely $In_{0.52}Al_{0.48}As$, $In_{0.47}Ga_{0.53}As$ and InP, it was found that HBr gives a very steep side-wall etch profile as shown in Figure 4.4. This resulted in the failure of metal step-coverage in subsequent processing. The thin InP cladding layers were etched in HCl, instead of HBr since $In_{0.52}Al_{0.48}As$ acts as an etch stop layer for HCl based etchants. The $In_{0.52}Al_{0.48}As$ barrier layer were subsequently etched in the H_3PO_4 based etchant.

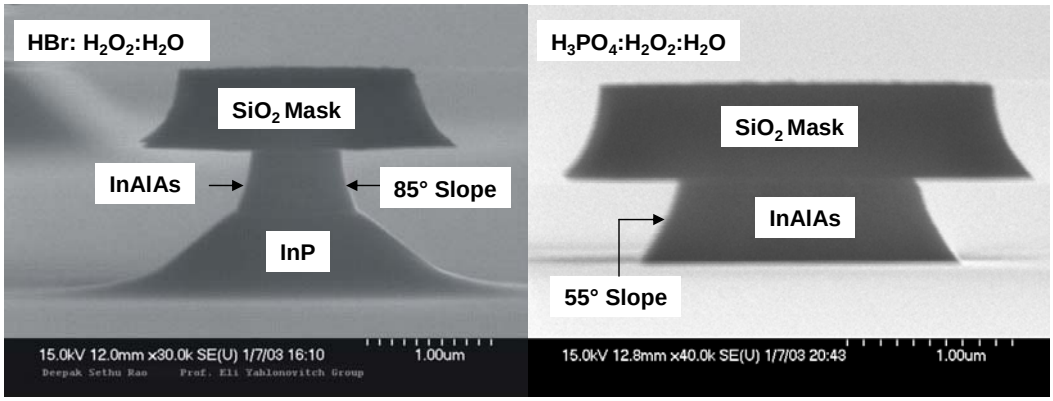

Figure 4.4: InAlAs side-wall profile etched in HBr and H_3PO_4 based etch mixtures.

4.2. Alloyed Ohmic Contact formation

Ohmic contacts are non-rectifying contacts that enable the injection of current into a semiconductor following Ohms's law. Simply placing a metal over a wide-bandgap semiconductor material such as III-Vs leads to a rectifying rather than Ohmic behavior due to the difference in the work function of the metal and semiconductor. The formation of Ohmic Contacts to our 2DEG epi-wafers consisted of doping the contact regions heavily by Ge, which can act as an n-type dopant in III-Vs. The dopant was introduced by alloying a eutectic mixture of AuGe in the contact regions by rapid thermal annealing.

AuGe is a commonly used alloy to make n-type Ohmic contacts to III-V materials [48]. Au and Ge form a eutectic mixture at a composition comprising of 88% Au and 12 % Ge which melts at a temperature of 360°C. Ge can actually acts as the dopant and AuGe is chosen for it's low eutectic melting point. Upon heating past the melting point the metal film melts with some co-melting of the semiconductor surface resulting in the mixing and diffusion of the eutectic alloy. In the specific case of GaAs, the Au reacts with the substrate Ga atoms to form various alloys, leaving behind Ga vacancies in the host lattice. Ge diffuses into the lattice, occupying the Ga sites and thus doping the material n-type [49].

Following the mesa etching steps, the substrate was prepared by the standard 3-solvent/ DI water clean, followed by UV photo-lithography using resist AZ5214E-IR detailed in the previous section. Ohmic metal stack comprising of 1500Å AuGe, 300Å Ni and 2000Å Au was deposited in an e-Beam evaporator chamber maintained at a vacuum of 3 x 10^{-6} Torr.

AuGe, as mentioned above is the main material in the metal stack for achieving Ohmic contacts to III-V devices. Nickel is an impurity added to enhance the diffusion of Ge and also serve as a wetting agent which prevents balling up of the metal. The diffusivity of Ge in III-Vs is observed to be strongly affected by the presence of impurities [50]. The top layer of Au is to enable the ease of bonding gold wires to make connection to external

circuitry for measurements. Following the evaporation, the metal was lifted off in a warm bath of Acetone maintained at 45°C.

The contact metal stack was annealed in a nitrogen atmosphere in a Rapid Thermal Annealer slightly above the melting point. The anneal ramp rate, anneal dwell time and anneal temperature were optimized for each heterostructure to obtain the minimum contact resistance. The AlGaAs/GaAs samples were annealed at 425°C for 60 sec and the InAlAs/InGaAs samples at 450°C for 4 min yielding minimum resistances of 2.7KΩ and 3.3 KΩ at room temperature.

4.3. Schottky Gate Electrodes

Rectifying Schottky metal-semiconductor contacts [38] are extremely crucial towards achieving Quantum Dots and Quantum Wires through electrostatic squeezing of a 2-Dimensional Electron Gas. Figure 4.5 shows SEM images of the fabricated Schottky gate electrode geometry defining the Quantum Dot and QPC on the AlGaAs and InAlAs heterostructures.

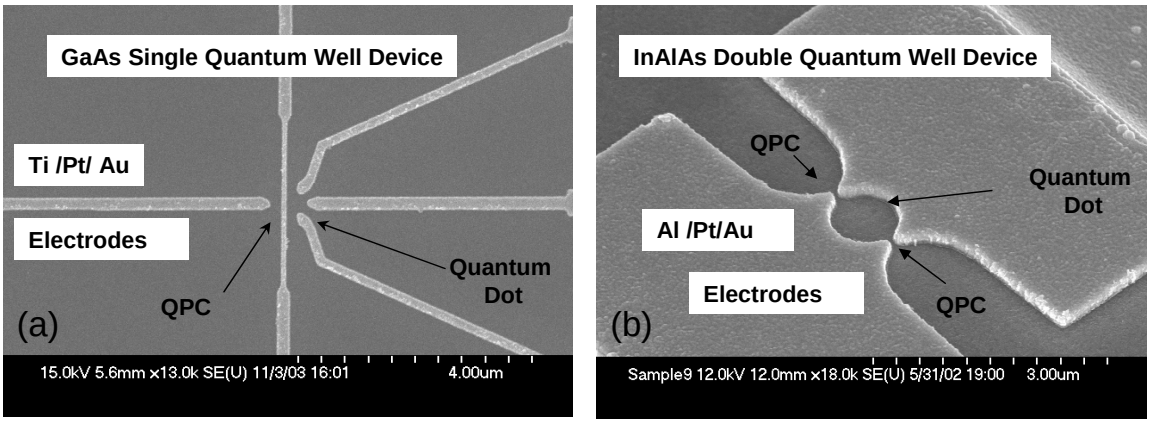

Figure 4.5: SEM of Gate Electrode Geometry: a) Multi-electrode lateral geometry for defining QPC channel to the side of the Quantum Dot in single quantum-well device (GaAs sample) b) Split- Gate geometry for defining QPC channel below Quantum Dot in a Double quantum-well device (InAlAs Sample)

Various considerations that go into the creation of non-leaky Schottky contacts include the choice of the metal with the correct work-function, surface preparation and cleaning before metal deposition and a minimum overlap area between the gate lines and semiconductor mesa. The Schottky gates were fabricated in a two step process: *Step 1* comprised of patterning the fine-line gate electrodes defining the Quantum Dot and QPC on the mesa surface through e-Beam lithography and *Step 2* involved the patterning of bonding bonds through standard photo-lithography to enable wire-bonding and establish electrical connection to the e-Beam gate lines.

Schottky contacts are rectifying contacts formed due to the bending of bands in the semiconductor when a metal comes in intimate contact with its surface. Band bending

occurs due to the difference in work functions of the metal (Φ_m) and the semiconductor (Φ_s) which results in a potential barrier (Φ_b) for the flow of carriers at the interface. The case for an n-type Schottky contact is shown in Figure 4.6.

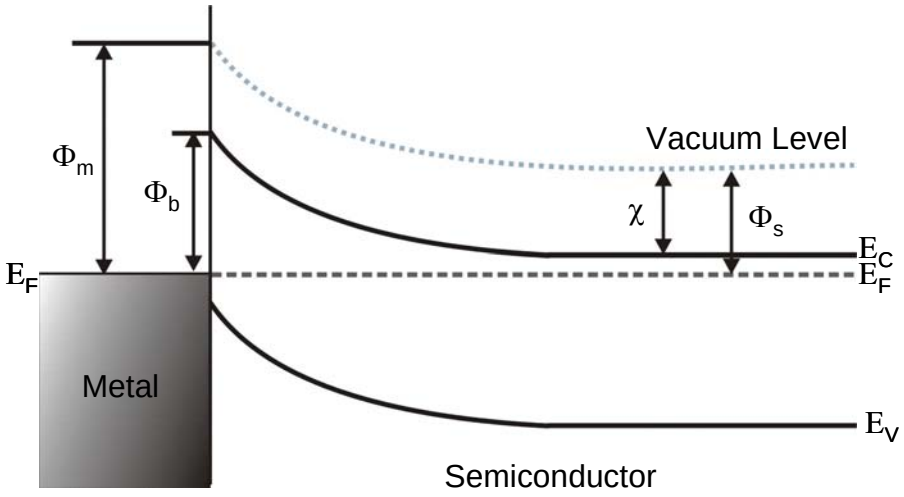

Figure 4.6: Rectifying Schottky barrier on an n-type semiconductor surface due to the work function difference between the metal and semiconductor.

The potential barrier for electron flow from the semiconductor to the metal is $\Phi_m - \Phi_s$ and the barrier for flow from the metal to the semiconductor is $\Phi_b = \Phi_m - \chi$. Here Φ_m is the work function of the metal; Φ_s is the work function of the semiconductor and χ is the electron affinity of the semiconductor. Although this suggests that Schottky barrier heights would be a strong function of the metal work function, it has been determined experimentally that on a GaAs surface, irrespective of the metal used, a rectifying contact with a Schottky barrier close to 0.8 eV is formed [51]. A large density of surface states at the interfacial layer is responsible for this fixed Schottky barrier [52]. These defect states

pin the Fermi Level at ~0.8 eV below the conduction band at the surface of GaAs [53] which results in the pinning of the barrier.

Although almost any metal that is placed on GaAs will yield a rectifying Schottky contact, the metal must also exhibit two other characteristics: i) Good adhesion and ii) Thermal stability. Titanium is the most commonly used metal meeting both the above criteria. We have used a metal stack comprising of e-beam evaporated 'Ti/Pt/Au' with thickness of 200Å/100Å/300Å to form the file line e-beam Schottky gates on the GaAs devices. The Gold over lay layer is only to reduce the resistance of the gate lines. The *Pt* is used as a barrier layer and prevents diffusion of the Gold through the Schottky Titanium layer to the surface of the semiconductor.

In the InAlAs/InGaAs 2DEG devices, an important consideration that went into the choice of InAlAs as the large band-gap barrier material was the higher Schottky barrier it exhibits with common metals [54]. $In_{0.52}Al_{0.48}As$ which is lattice matched to both InP and $In_{0.53}Ga_{0.47}As$ has a band-gap of 1.46 eV at 300K and has been observed to give relatively higher Schottky barrier heights compared to InP. We have used Aluminum with a barrier height of ~0.8eV as the gate metal in our InAlAs devices. As in the case of GaAs, the *Al* layer was capped with layers of *Pt* and *Au*. The evaporated metal stack comprised of 100Å of *Al*, 400Å of *Pt* and 500Å of *Au*.

4.4. Photo-Masking with pin-hole aperture

A common phenomenon during the exposure of semiconductor samples to light is the increase in the conductivity of the sample with light exposure. This photo-induced increase in conductivity or "Positive Photo-conductivity" is highly undesirable in a detector for quantum tele-communications that relies on the transfer of information from photon spin states to electron spin states. Although the process of information transfer can be achieved in suitable engineered devices utilizing optical selection rules [33], it is crucial to have the ability to detect the photo-excitation and trapping of single electrons with reasonable quantum efficiency.

Positive photo-conductivity is caused by the trapping of photo-excited holes in defects or un-ionized donor atoms in the bulk of the sample leading to an increase in the channel electron density. Detailed discussion about hole-trapping will be provided in Chapter 5. Here we discuss the device fabrication steps to suppress the trapping of photo-holes and "filter out" individual photo-electron trapping events. This is particularly essential in the AlGaAs/GaAs 2DEG devices due to the high concentration of negatively charged hole-trapping defects at low temperatures [55]. As presented in Chapter 5, we have also experimentally detected the trapping of individual photo-holes by such defect centers that eventually leads to the addition of conductivity modes to the channel of a QPC [56].

Positive photo-conductivity is suppressed in our devices by a metallic mask deposited over the device mesas. The highly opaque mask is achieved by evaporating a thick layer of Aluminum, a metal with a good electrical conductivity and consequently a small skin

depth over the entire active area of the mesa. The imaginary part of the refractive index (K) for Aluminum is 8.6 at 760nm, the wavelength at which inter-band photo-electrons are excited in GaAs in our experiments. The corresponding $^1/e$ skin depth given by $Z_{1/e} = c/(2\pi\lambda K) = 140Å$. A thickness of 1500Å is used to significantly suppress light transmission through the mask. The Aluminum metal layer is separated from the metallic gate electrodes by a 700Å thick insulating layer of SiO_2, deposited by e-Beam evaporation along with the Aluminum masking layer. A 15nm thick adhesion layer of Ti is deposited on the SiO_2 layer to promote the adhesion of Al to SiO_2.

Following evaporation of the photo-mask and lift-off, a pin-hole aperture of radius equal to 200nm was defined by e-Beam lithography right above the quantum dot region. The Aluminum layer in the aperture region was removed by dry etching in an inductively coupled plasma Cl_2 etcher using Cl_2/BCl_3 dry etch chemistry.

A schematic of the device layout with metallic opaque photo-mask over active mesa area and etched pin-hole aperture over quantum dot are shown in Figure 4.7.

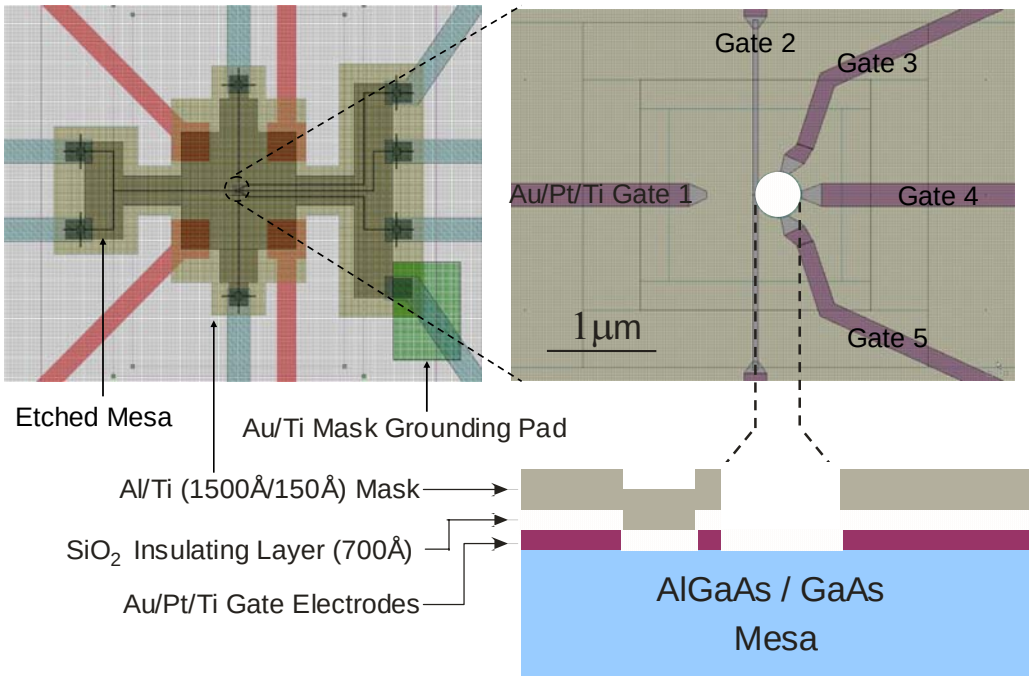

Figure 4.7: Schematic device layout of devices in AlGaAs/GaAs with metallic opaque photo-mask over active mesa area and etched pin-hole aperture over quantum dot.

The final step in the fabrication process before packaging the device involved an evaporation of 500Å of Ti and 2500Å of Au to make electrical contact between the Aluminum mask and a wire-bonding pad to allow for grounding the mask during optical exposure. Grounding the mask prevents a charge build-up due to prolonged exposure which would otherwise cause an undesirable drift in the operating point of the device. The fabricated devices were mounted onto a chip carrier using an electrically conductive silver epoxy (H20E from EPO-TEK) and wire-bonded using an ultrasonic wedge bonder. An SEM of a bonded device glued onto a chip carrier is shown in Figure 4.8.

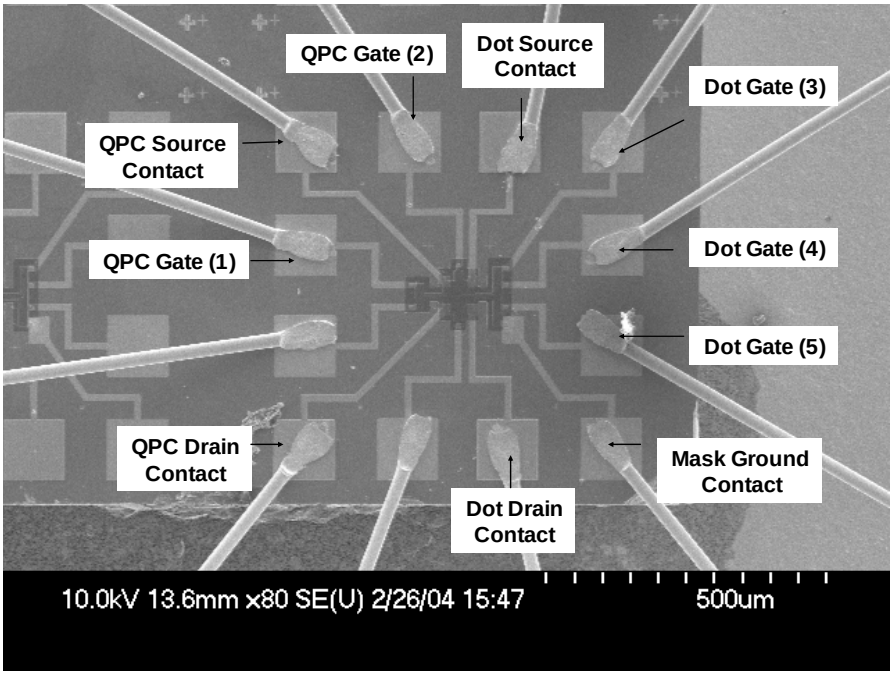

Figure 4.8: SEM of final bonded device. The device is mounted onto a chip-carrier for characterization using electrically conductive silver epoxy.

CHAPTER 5 Photoconductance Quantization in a AlGaAs/GaAs MODFET Single Photon Detector

This chapter describes the characterization of the QPC-Quantum Dot devices fabricated in the AlGaAs/GaAs modulation doped heterostructure (GO3) described in section 3.2. As mentioned earlier, tele-communications of quantum information using single photons requires a detector that detects a single photo-exited electron with a non-invasive gentle gain mechanism that provides for storage of the photo-excited carrier, preferably the photo-electron in artificial traps designed to hold just one electron.

A set of experimental results towards the realization of such a detector will be presented in the current and the following two chapters of this dissertation. First, conventional positive photo-conductivity in AlGaAs/GaAs heterostructures is discussed with results on the detection of single photon initiated positive steps in conductivity. Positive photo-conductivity, which is caused by the trapping of photo-holes, is an undesirable effect in a quantum tele-communications detector designed to transfer photon spin information to electron spin information. The signature of electron trapping is negative photo-conductivity. A second set of experimental results on the trapping and detection single photo-electron in an artificial electrostatic quantum dot, accomplished through the suppression of the dominant positive photoconductive will be discussed in the next chapter.

5.1. Measurement Set-up

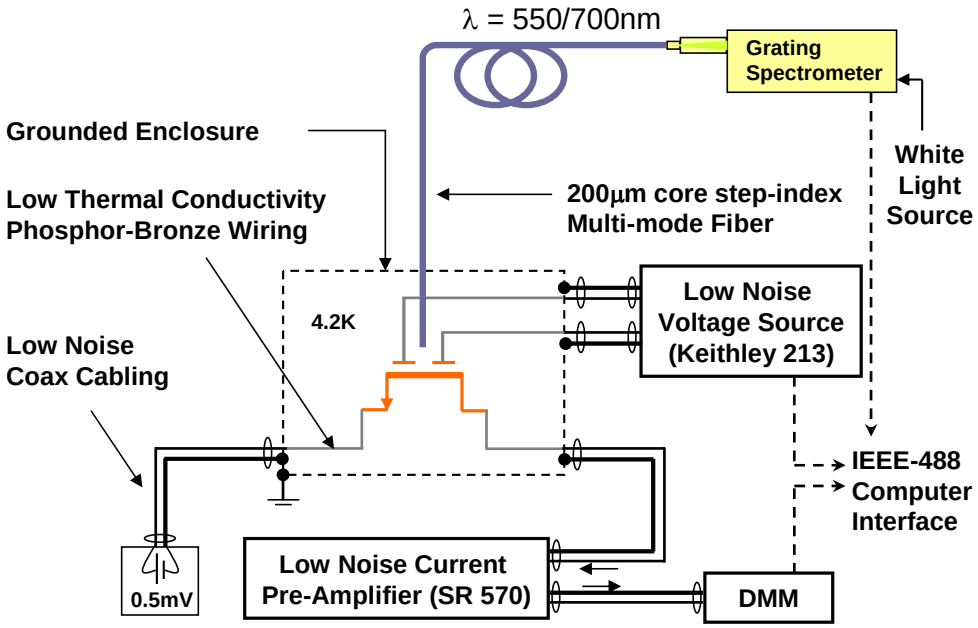

Figure 5.1: Measurement set-up for electrical and optical characterization of a split-gate point contact transistor.

The experimental arrangement for low noise characterization of the point-contact FET structure is shown in Figure 5.1. Figure 5.2 shows a schematic of the device operation. White light from a Tungsten lamp is diffracted by a grating spectrometer (1200 grooves/mm, 0.15 nm resolution). Monochromatic light at λ = 550nm (or 700nm) from the spectrometer was attenuated by a 20dB neutral density filter and focused onto a 200μm core step-index glass fiber to illuminate the sample kept cold at 4.2K in a liquid Helium-4 dewar. The fiber was carefully shielded to block extraneous photons from leaking in through the outer jacket. A simple end-fire coupling technique is used to focus

light on to the sample with a spot size of 1mm diameter. The region sensitive to single photo-carrier absorption, is the area between the two split-gates having lithographic dimensions of 100 nm by 300 nm (active area of 3 x 10^{-10} cm^2), shown in the schematic in Figure 5.2. Assuming a Gaussian profile for the incident spot on the device, with a FWHM of 1mm diameter, the actual photon flux in the small active area between the split gates is 7 x 10^{-9} times smaller than the total incident flux. The power at the end of the fiber was calibrated by a Si detector and adjusted to be about 9 pW at 550nm, to achieve a very mild photon flux in the sensitive area between the split gates [(9pW x 7 x 10^{-9}) /hν at 550 nm = 0.175 photons/sec].

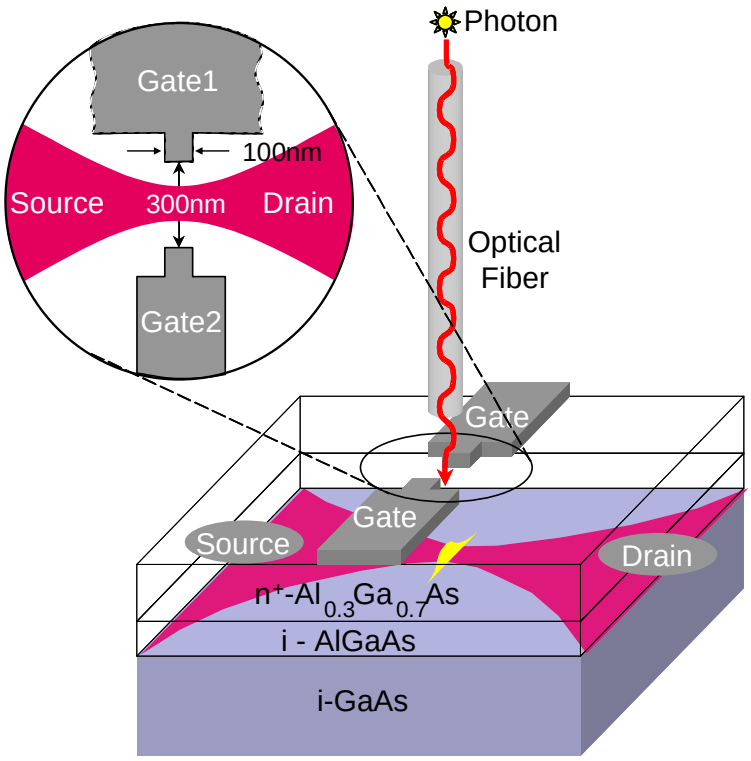

Figure 5.2: Schematic diagram of the device operation. A nearly pinched off point contact channel in a 2D electron gas at an $Al_yGa_{1-y}As/GaAs$ interface can act as a sensitive photo-detector.

The electrical measurement consisted of the DC setup illustrated in Figure 5.1. The device is biased with a constant source-drain voltage of 0.5 mV. Shielded low noise BNC cables are used for all external cabling at room temperature. Access to the 4.2K sample is provided by twisted pair cryogenic Phosphor-Bronze (PB) wires. PB wires have lower thermal conductivity than copper and reduce the heat load to the sample space. A low noise room temperature current pre-amplifier (SR 570) with a gain setting of 50nA/V is used to amplify the source-drain current and the output voltage is read through a precision digital multimeter. A low-noise quad voltage source from Keithley instruments (Keithley-213) is used to bias the split gate electrodes. The gate voltage source, the digital multi-meter and the spectrometer were computer controlled through standard IEEE-488 computer interface bus.

5.2. Natural photo-hole trapping sites in AlGaAs/GaAs

In this section we briefly describe the origin of the positive increase in conductivity that is commonly observed in semiconductors upon exposure to light. A physical insight into this effect is necessary to explain the various interesting features of the experimental results that will be presented in the subsequent sections.

Donor atoms in semiconductors normally exist either in the neutral state d^0 or the ionized state d^+. However, donors in $Al_yGa_{1-y}As$ with $y > 0.2$ can exist in a third stable state at low temperatures with an excess trapped electron, namely the d^- state which is also known as the DX or the DX^- center. Being negatively charged the DX center acts a very efficient hole trapping center. The DX center was first thought to consist of a substitutional donor atom and an unknown lattice defect like vacancy [55]. Thus, the name DX center was coined, the D as a shortcut for the donor and the X for the unknown defect. But it has been observed that shallow donor atoms in $Al_yGa_{1-y}As$ with $y < 0.2$ change spontaneously into DX centers under the application of hydrostatic pressure [59]. This observation led to the proof that the DX center consists of a substitutional donor atom only and it's special behavior is connected to the band structure of the host lattice [60]. Thus, the DX center is nothing but a negatively charged donor atom resulting from the reaction $2d^0 \rightarrow d^+ + DX^-$ where d represents a substitutional donor atom such as Si.

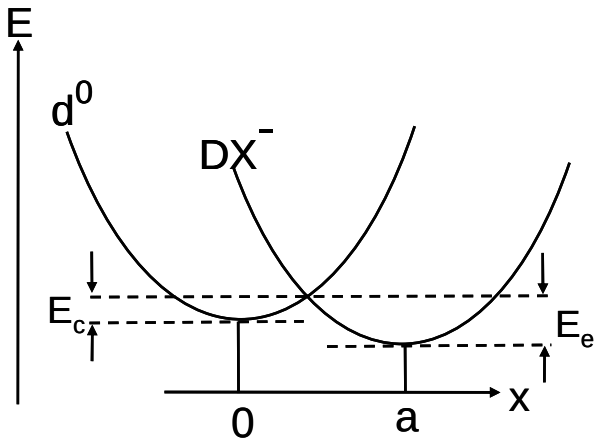

Figure 5.3: Configuration Co-ordinate diagram of a DX^- center, caused by the trapping of an electron by a neutral donor atom followed by a lattice relaxation lowering the total energy of the system.

Normally, the energy of a donor atom increases upon the capture of two electrons making such a capture highly unlikely. But in lattices like $Al_yGa_{1-y}As$ with $y>0.2$ or under large hydrostatic pressure even with $y<0.2$, a donor atom undergoes a spontaneous large lattice distortion when occupied with two electrons which reduces the energy of the system. The large lattice distortion consists mainly of a displacement of the donor atom off the regular site in the direction of a crystal cubic position towards an interstitial site [61]. The total energy of the system, which consists of the electron energy and the elastic energy, is reduced due to this displacement resulting in a stable negatively charged donor state, as shown in the configuration co-ordinate diagram in **Figure 5.3**.

At low temperatures, a donor remains frozen either in the DX^- state or in the d^+ state in the absence of sufficient phonon energy to over the barriers E_c (or E_e.) At room temperature, a donor normally exists in the ionized d^+ state. As the temperature is lowered, two electrons are captured by an ionized donor, followed by a lattice relaxation, which reduces the total energy giving the stable DX^- state. No electrons are left in the conduction band and the sample shows greatly reduced conductivity immediately upon cooling.

Now, upon illumination with light of photon energy sufficient to ionize the DX^- state, a persistent emptying of the DX^- centers occurs, transferring electrons into the conduction band that enhances the conductivity of the sample. This conductivity persists for hours after the light is switched off at temperatures below 100K [62]. This Persistent Photoconductivity (PPC) is a common characteristic phenomenon associated with the presence of DX centers. Photo-ionization of DX centers is also possible by the capture of a photo-excited hole due to inter-band absorption in AlGaAs. Such a hole capture is believed to be the cause for slow photoluminescence transients in silicon doped AlGaAs. The photoluminescence shows a slow build-up due to the initial capture of photo-excited holes by DX centers associated with silicon doping and reaches a maximum value once the DX centers are saturated [63].

In conclusion, due to the presence of negatively charged donors that trap photo-excited holes, persistent positive photoconductivity is common in AlGaAs/GaAs devices. In the following sections, we present the experimental measurements detecting individual photo-hole trapping events. A point contact FET, is used to sense these individual events that are cumulatively responsible for the positive increase in channel conductance.

5.3. Photo-Conductance Quantization

It is now well-know that the conductance of a ballistic conductor such as a Quantum Point Contact changes in steps in response to external stimuli that can

enhance/reduce the conductivity of the channel. A widely studied phenomenon is the conductivity quantization induced by the modulation of voltages on gate electrodes coupled electro-statically to the ballistic conductor [44-46]. In this section, we present the results of the first observation of optically induced addition of conductivity modes to the channel of a quantum point contact leading to a quantized increase in photo-conductance. The results that will be discussed here have been published in [56].

Figure 5.4 presents the the source-drain conductance of the quantum point contact transistor (Length = 100nm, Width = 300nm) fabricated in the AlGaAs/GaAs heterostructure (GO3) described in section 3.2. The graph plots the conductance as a function of two external stimuli: (i) The voltage applied on the two QPC split-gates and (ii) Exposure to weak light at two wavelengths, λ = 700 nm and 550 nm.

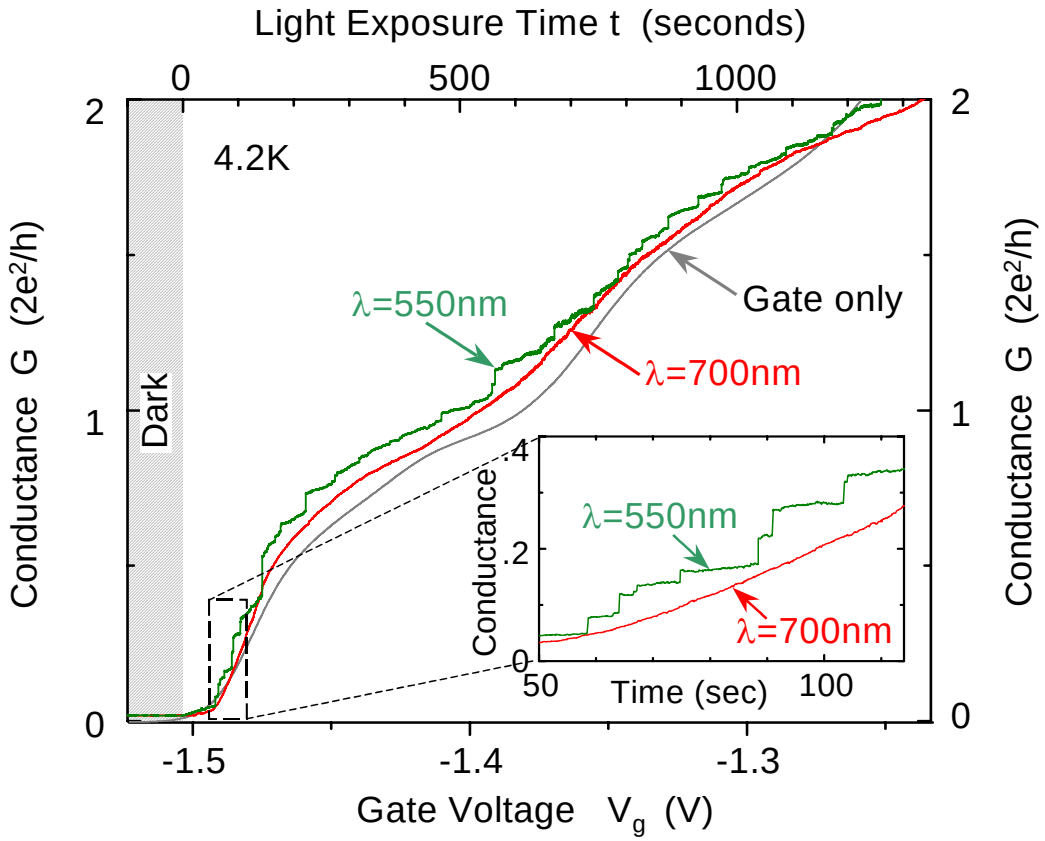

Figure 5.4: The source/drain channel conductance of a QPC induced by a modulation of a gate voltage and by light exposure for a period of time. The conductance quantization plateaus at multiples of $2e^2/h$ are practically identical. With light at $\lambda = 550$ nm, there is the additional feature of individual small conductance steps associated with single photons.

As the gate voltage is made increasingly negative in Figure 5.4, the device conductance decreases in steps as expected due to the successive removal of electron wave-guide modes constituting the QPC channel. Two conductance steps, one near $2e^2/h$ and the other near 2 x $2e^2/h$ are shown in the curve. The sharpness of the steps is consistent with

the temperature of 4.2K at which the device was operated. In addition, there is a well-know shoulder of conductance 0.7 x $2e^2/h$ thought to be associated with the electron exchange interaction effects [57, 58].

The remarkable feature of the results shown in Figure 5.4 is that there are two different physical phenomena, producing almost identical source/drain conductance on the vertical axis. The horizontal axis at the top measures the net positive charge in terms of optical exposure time from a weak beam, and the horizontal axis at the bottom measures positive increase of gate voltage. The curve labeled "gate only" shows that positive gate voltage, above the -1.5 Volt gate threshold, opens up the electron channels producing conductance steps. Likewise, exposure to a weak light source of wavelength λ = 700 nm, at a fixed bias voltage produces trapped positive charge that also opens up the electron waveguide channels, producing exactly the same conductance steps. In either case, positive net charge opens up the source/drain electron current channels, leading to the observed electron conductance steps.

The photo-exposure begins at time t = 0 in **Figure 5.4**, to the right of the crosshatched dark region where the conductivity begins as a constant. If the photo-exposure is prematurely terminated, the conductance becomes constant again, persisting at the new value for weeks. Positive photoconductivity is essentially caused by the trapping of positive charges near an electron channel. The absorption of photons near the channel creates localized positive charges, which cumulatively add up to reduce the negative gate

voltage seen by the channel. In AlGaAs/GaAs heterostructures, persistent photo-conductivity is caused by the trapping of positive charges by neutral donor sites or negatively charged defect centers at low temperatures know as DX^- centers. The increased conductivity caused by the trapping of positive charges (photo-holes) is retained even after the light is switched off. This persistence of photoconductivity in AlGaAs/GaAs heterostructures is a phenomenon known to occur at temperatures lower than 100K [64, 65].

5.4. Detection of single inter-band photons

The second key result in **Figure 5.4** is the appearance of single photon steps when the excitation wavelength is set to $\lambda = 550$ nm. The band gap of $Al_{0.3}Ga_{0.7}As$ at a temperature of 4.2K is close to 1.9 eV corresponding to $\lambda = 653$ nm. At $\lambda = 700$ nm, only a persistent smooth increase in conductivity with the reproduction of the conductance quantization steps is observed. But the additional phenomenon of single photon steps is seen when the sample is exposed to $\lambda = 550$ nm photons with an energy well beyond the band gap of $Al_{0.3}Ga_{0.7}As$ at 4.2K. The green curve in **Figure 5.4** depicts the detection of single photon events. The curve still follows the overall shape of the quantized conductance steps, but the curve itself consists of many smaller steps that, in aggregate, produce the quantized conductance shape, including the 0.7 ($2e^2/h$) feature. The smaller steps, we attribute to absorption of individual photons, and the corresponding capture of a single photo-hole by trapping sites (DX centers or neutral donor atoms) close to Quantum

Point Contact constriction conducting source/drain channel. Since the traps are at variable distances from the source/drain channel, each photon produces a different step height. Unlike the violent gain mechanism of an avalanche photo-diode, the gain in our device is derived from the sensitive conductivity of the QPC channel to nearby single trapped charges.

This demonstration of single photon detection events is similar to an experiment by Shields et al.,[66] who have trapped photo-excited holes in self-assembled InAs Quantum dots. The InAs quantum dots, assembled near the 2-DEG have bound states lying lower in energy than the conduction band edge of the GaAs channel and act as trapping centers for the photo-excited holes. Though the results are similar, the InAs quantum dots are not necessary for the capture of single photo-excited holes. The naturally occurring DX centers in a conventional AlGaAs/GaAs modulation doped field effect transistor can act as hole trapping centers.

In Figure 5.5, we plot the differential change in conductance, dG/dV_g, with voltage on the split gate electrodes. Also on the same figure is plotted the change in conductance δG due to light exposure. As expected the discrete photon steps for $\lambda = 550$ nm are taller where the conductance curve is steeper, due to greater sensitivity to electrostatic charge changes when dG/dV_g is larger.

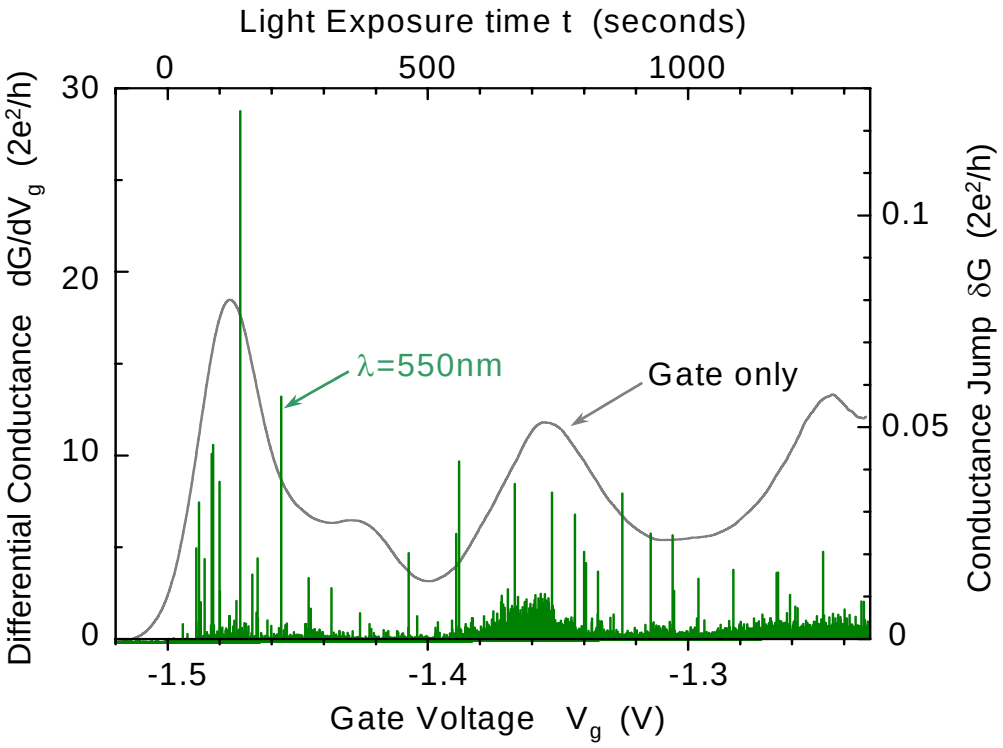

Figure 5.5: Differential channel conductance as a function of gate voltage and individual photon conductance jump height as a function light exposure.

In Figure 5.6, we test for proper photon statistics by plotting a histogram of the time intervals between photon events. The intervals should fall on a decaying exponential for random photon events, as is appropriate for un-squeezed photon statistics. We can count about 70 individual discrete photon steps in the λ=550 nm curve in Figure 5.6. As expected the intervals fall on an exponentially decaying curve with a mean arrival time of 18 seconds.

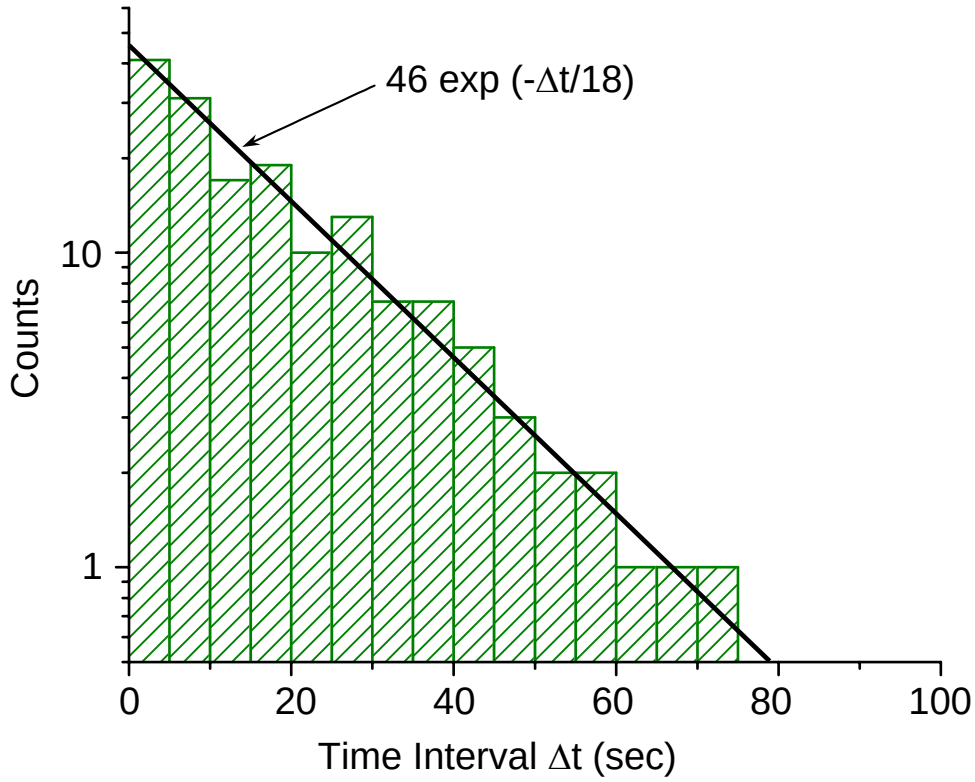

Figure 5.6: Histogram of time intervals between photon detection events.

The low photon detection rate is consistent with the small detection area of 3 x 10^{-10} cm^2. The optical power at the end of the fiber is ~9 pW which corresponds to a photon flux of 25 x 10^6 photons/sec at λ = 550 nm. As specified earlier, due to the small area of detection, the flux absorbed in the active area is 7 x 10^{-9} times smaller which is 0.175 photons /sec. The total light exposure time is ~1300 sec and the total number of photons incident on the device is ~227 photons. Hence the 70 discrete photon steps observed in this period corresponds to a quantum efficiency of 30%.

5.5. Wavelength dependence of Single Photon Detection

The onset of single photon steps was observed at wavelengths shorter than 650 nm and pronounced at λ = 550 nm. The wavelength dependence of the appearance of discrete single photon steps is strongly correlated to the band gap of $Al_{0.3}Ga_{0.7}As$ at 4.2 K, which is 1.9 eV corresponding to λ = 653 nm. The single photon steps are not seen with below band gap photons at λ =700 nm. The DX centers, which are responsible for the capture of photo-excited holes, reside in n-doped AlGaAs layer. A model for single photon detection is shown in Figure 5.7.

Photons with energy greater than 1.9eV are absorbed in the $Al_{0.3}Ga_{0.7}As$ layer above the 2-DEG where photo-excited holes are trapped by DX^- centers. Alternatively, holes can also be trapped by neutral donors. In either case, due to the proximity of these centers to the 2-DEG, the extra positive charge leads to the observation of single photon steps and a persistent increase in the channel current. The photo-excited electron on the other hand ends up in the channel and just contributes to the current flowing between the source and drain Ohmic contacts of the device.

Below band gap photons with λ > 650 nm can cause direct optical ionization of DX centers or can be absorbed in the nominally undoped GaAs buffer layer. The photoionization cross-section of DX centers has been experimentally measured by Brunthaler et al. [67] for photons with energies below and above the band gap of AlGaAs. This ionization cross-section directly describes the efficiency of conversion of

DX centers due to illumination with different photon energies. It has been found that the ionization cross-section increases by about three orders of magnitude when the photon energy exceeds the band-gap.

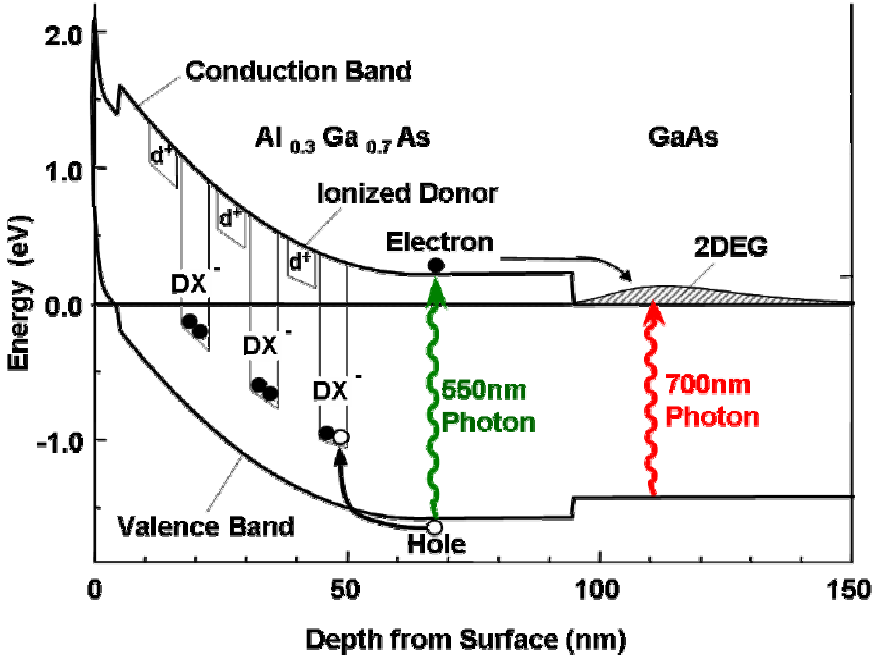

Figure 5.7: A model for the single-photon detection, carrier capture, and the photoconductive gain mechanism. A photo-hole is trapped at either a DX^- center or a neutral donor d^0. The net positive charge increases the channel conductance. The long-lived electron current passing through the channel over time is responsible for the photoconductive gain mechanism.

Because of a reduced DX center ionization cross-section, below band gap photons are mostly absorbed in the nominally undoped GaAs buffer layer, which is weakly n-type. The photo-excited hole trapping sites in GaAs are the residual neutral donors which are very dilute and not in close proximity to the channel. Hence they do not produce any

discernible discrete jumps in current. But they do produce the overall persistent increase in photoconductivity and reproduce the conductance quantization steps as shown in **Figure 5.4** for λ = 700 nm.

The conductance versus gate voltage and light exposure in **Figure 5.4** has been plotted up to two conductance plateaus. Above this conductance level, the gate-induced and photo-induced conductances do not match. The gate-induced conductance continues to show more plateaus but the photo-induced conductance rise shows a decreasing trend and saturates above this point.

The decrease in photo-induced conductance with prolonged exposure can be explained by the experimentally observed fact that DX centers exhibit strong spatial correlation [68]. During the initial build-up of inter-band persistent photoconductivity, spatial correlation leads to the formation of DX^- - d^+ dipoles upon ionization of a DX^- center to an ionized donor d^+ leading to a reduced density of isolated DX^- centers. Since these dipoles have a considerably smaller hole capture cross section the photoconductivity increases at a slower pace with exposure. The dipoles eventually get destroyed when all the isolated DX^- centers have been exhausted. In the small active area of 3 x 10^{-10} cm^2, only about 100 trapping centers are present near the active region, explaining the saturation in photoconductance. At a channel capacitance of ~0.1femto-Farad, the 70 charges produce about the same electric field as the gate voltage change of ΔV_g =0.2 volt that was

required to reach the 2 x $2e^2/h$ conductance plateau. The eventual saturation of the photo-induced conductance is simply due to the saturation of hole trapping sites.

CHAPTER 6 Photo-electron trapping, storage and detection in artificial single-electron quantum dots in a AlGaAs/GaAs MODFET

In Chapter 5, we discussed the phenomenon of photo-hole trapping in naturally occurring trapping centers in AlGaAs/GaAs heterostructures and experimentally showed that the conductance of a quantum point contact FET can be extremely sensitive to trapped photo-carriers near the channel. The photo-electron though ended up in the conducting channel of the QPC transistor and was swept away by the source/drain electric field. Rather than trapping the photo-excited hole, quantum tele-communications requires the trapping and storage of photo-electrons. Electrons in semiconductors have the long spin coherence times required for quantum information storage and processing [35]. 'g-factor' engineering allows for quantum information transfer from photon spin states to electron spin states without leaving behind any information in the hole [33, 40]. Thus, in a single photon detector designed for quantum tele-communications it is essential to trap and store the photo-excited electron in artificially engineered single-electron traps that would allow for spin measurement and manipulation. In this section we experimentally demonstrate the injection, detection and storage of individual photo-excited electrons into an empty quantum dot defined electrostatically by metallic gates on the surface of the AlGaAs/GaAs heterostructure.

The signature of photo-electron trapping is negative photo-conductivity - a drop in the current through the QPC transistor upon illumination. Negative photo-conductivity is commonly not observed in GaAs heterostructures, and a persistent photo-induced increase in conductivity has been well known for some time now [62]. As explained in section 5.4, positive photo-conductivity is a result of the trapping of photo-excited holes predominantly by negatively charged defects at low temperatures known as DX centers leading to an increase in the 2D electrons gas (2DEG) density. Persistent negative photo-conductivity at low temperatures has been reported only after the saturation of hole trapping centers, most likely ionized donors, and only at short wavelengths causing photo-excitation in the doped AlGaAs barrier layer [69, 70]. On the other hand, photo-excitation in GaAs has always shown a positive increase in conductivity. Now, by creating an artificial electron trap defined by electrostatic metal gate electrodes, we have been able to detect the addition of a single photo-excited electron into the electron trap. A QPC field-effect transistor is integrated adjacent to the dot serves to detect the injected photo-electron in a non intrusive way. When an electron is injected into the quantum dot, the increased electrostatic repulsion causes a negative conductivity step in the QPC transistor current. Scanning electron micrographs of the device layout and Schottky gate geometry on the device mesa designed to create an electrostatic quantum dot, adjacent to a point contact transistor is shown in Figure 6.1.

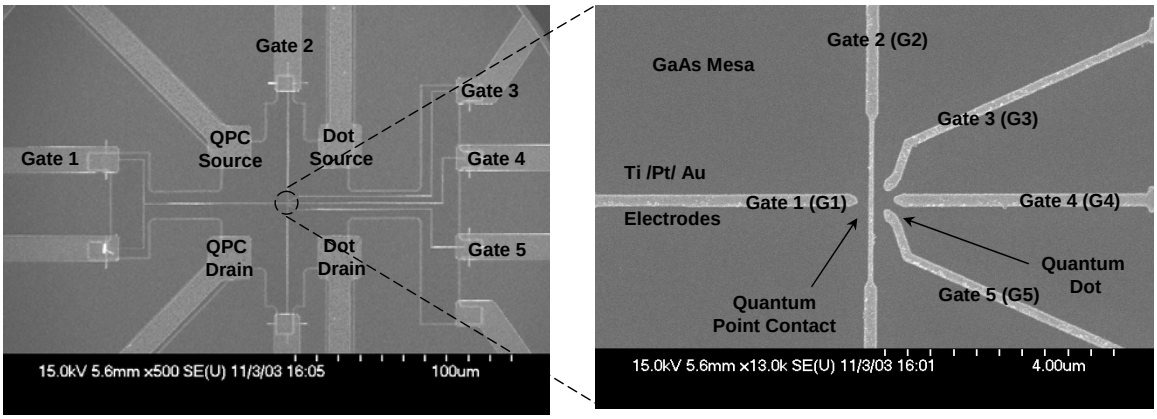

Figure 6.1: Scanning Electron Micrographs of device and Schottky Gate Electrode geometry. Gate 1 and Gate 2 define the point contact transistor. Gates 3, 4 and 5 create a quantum dot potential well region for photo-electron trapping and storage.

The device was fabricated on the GaAs heterostructure described in section 3.2, the same heterostructure layout as the one used in the photo-hole trapping experiments. In addition to the extra gate electrodes needed to define the quantum dot region, a key modification to the device compared to the one used for single photo-hole detection experiments is the deposition of a shadow mask on the device mesa with an etched aperture over the electrostatic quantum dot as shown in the SEM of Figure 6.2. The photo-mask comprises of a metallic Aluminium layer designed to be nearly opaque at the photo-excitation wavelength of λ=760nm. The detailed construction of the masking layer has been provided in section 4.4. This modification accomplished the suppression of the usually dominant positive photo conductivity and permitted photo-excitation only in the immediate vicinity of the electrostatic quantum dot.

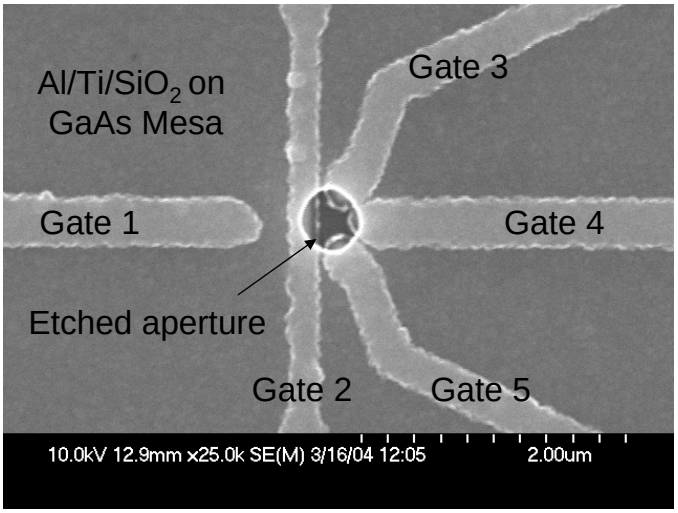

Figure 6.2: SEM of device with an Aluminium mask designed to be nearly opaque at the photo-excitation wavelength of λ=760nm, to suppress photo-excitation in the device expect in the small pin-hole aperture region etched over the quantum dot. For a cross-section view of the Al mask above the device, please see Figure 4.7.

6.1. Lateral QPC-Quantum Dot: Electrical characterization

The integrated electrostatic quantum dot-point contact transistor structure shown in Figure 6.1 is formed by a set of five Schottky gate electrodes. Gates 1 and 2 (G1 and G2) define a quantum point contact (QPC) between the left source and drain Ohmic contacts. Adjacent to this point contact transistor, a circular quantum dot with a lithographic radius of 200nm is defined by gates G3, G4 and G5. The quantum dot is formed by electrostatic squeezing the 2DEG by these surface metallic gates.

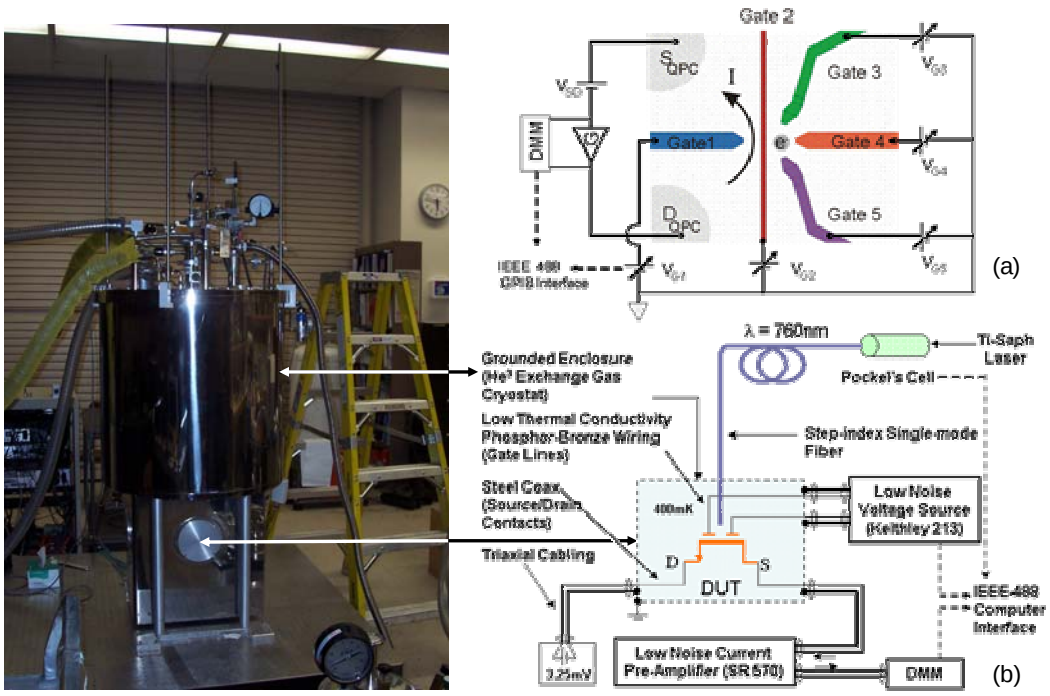

Figure 6.3: (a) Device biasing schematic (b) Measurement set-up for low-noise electrical and optical characterization.

Negative voltages on the five surface gates isolate a puddle of electrons in the 2DEG adjacent to the point contact transistor as shown in the schematic in Figure 6.3 (a). Gates G3 and G5 together with G2 control the tunnel coupling of the electrons in the dot to the external 2DEG reservoirs, while gate G4 is used as a plunger to push electrons out of the dot one at a time down to the last electron, thus creating an empty dot just before exposure to light.

In Figure 6.4, we plot the I-V curves depicting the current through the point contact versus the voltage on the plunger gate G4. Following the cooling of the device to 0.43K, gates G1 and G2 are first set negative to define the channel of the point contact transistor.

Subsequently gates G3 and G5 are made negative to set the tunnel barriers to the dot and finally the plunger gate G4 is set negative to scoop electrons into a puddle adjacent to the point contact. It is now well known that the conductance of an electrostatic quantum dot oscillates periodically due to single electron tunneling in response to a continuous potential change of a gate electrode capacitively coupled to the dot [71]. These single electron tunnel events, known as Couloumb blockade oscillations, can be observed in the transport of current through the quantum dot. In our experiments, it is important that the photo-electric charge be detected by means of an adjacent transistor, rather than by invasively passing current through the dot. Such a non-invasive charge measurement technique was first experimentally demonstrated by Field et al., [72] and has become a powerful technique to study the electronic properties of such gate defined quantum dots [73-75]. The I-V curve in Figure 6.4 plots the conductance of the QPC channel as the plunger is made exceedingly negative to enable trapped electrons to overcome the tunnel barriers set by gates G3/G5 and eventually escape the dot.

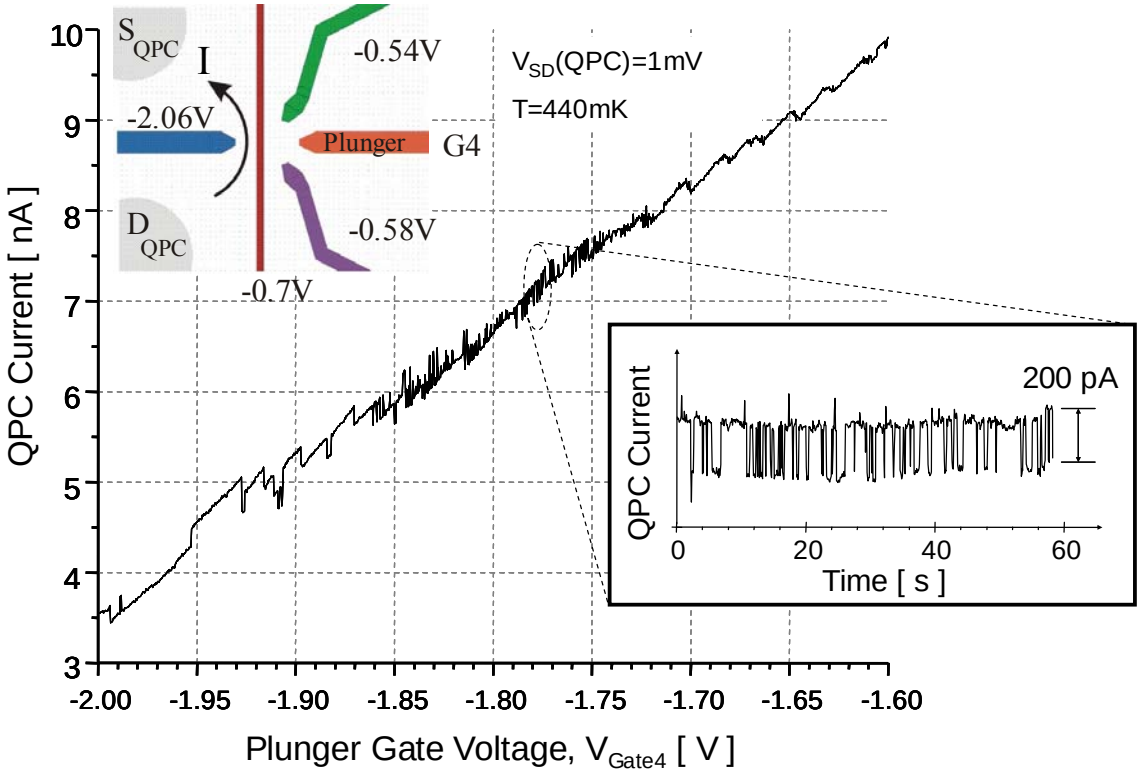

Figure 6.4: Single electron tunneling through the dot detected by the QPC transistor.

Beginning at the top right corner, the QPC current shows smooth steps on a falling background. This background slope is simply a result of the coupling between the point contact and the plunger voltage. The interesting features are the smooth steps and random telegraph like switching events that are superimposed on the background. These features are caused by single electron tunneling through the dot detected by the QPC.

The plunger is swept in increments of 1mV starting from -1.6V. With increasing negative voltage on the plunger, the electronic energy levels in the dot rise with respect to the

Fermi level in the surrounding 2DEG and the dot potential becomes more negative. When the top most occupied electronic level comes within the range of the external Fermi level by an average value less than the charging energy of the dot, the electron begins to tunnel out. An example energy level alignment for the case where the dot is occupied 50% of the time is shown in Figure 6.5.

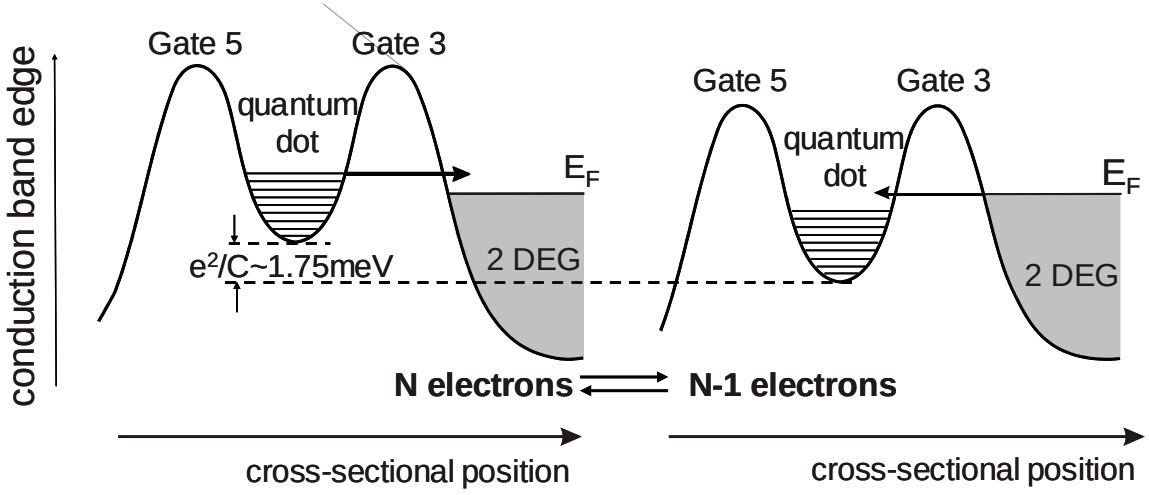

Figure 6.5: Potential landscape across the dot and tunnel barriers (set by gates G3 and G5), at a favorable plunger voltage setting that gives a Dot-2DEG tunneling with a 50% duty cycle.

When electrons tunnel back and forth between the dot and the external 2DEG reservoir, the dot potential fluctuates by an amount equal to the charging energy of the dot. The dot acts as a 2D metallic disk of radius 100nm when the gates are biased, and we estimate the charging energy of the dot, e^2/C, to be 1.75meV. As the plunger voltage becomes more negative, the top most dot electron spends longer time durations in the 2DEG reservoirs

until eventual it escapes. The point contact transistor senses the average electrostatic potential of the dot reflecting the percentage time the electron is in the dot. Each smooth step corresponds to the life-time of the top-most electron in the dot. The maximum change in conductance or the peak in the modulation steps occurs at the 50% duty cycle condition shown in Figure 6.5.

Now, with increasing negative voltage on the plunger, the dot shrinks in size and simultaneously the transparency of the tunnel barriers reduces, i.e the potential barriers near the tunnel exits at gates G3 and G5 become thicker. As a consequence, the tunneling rate slows down and the fluctuation in the dot potential transitions into more detectable random telegraph-like switching events (lower portion of the I-V plot in Figure 6.4). If the plunger voltage is held fixed at a transition point, the point contact current fluctuates between two states corresponding to a charge of N and N-1 electrons on the dot.

6.2. The single-electron Quantum Dot regime

The purpose of the electrical calibration procedure before optical exposure is determine the operating gate voltages at which the single electron dot state can be achieved for a given device geometry upon cool-down. In order to access the few-electron dot regime at a reasonable plunger gate voltage, an operating point different from that described in section 6.1 is chosen. The voltages on gates G2, G3 and G5 are made more negative while still maintaining operating tunnel barriers. The I-V curve and the gate voltages in the few-electron dot regime are shown in Figure 6.6.

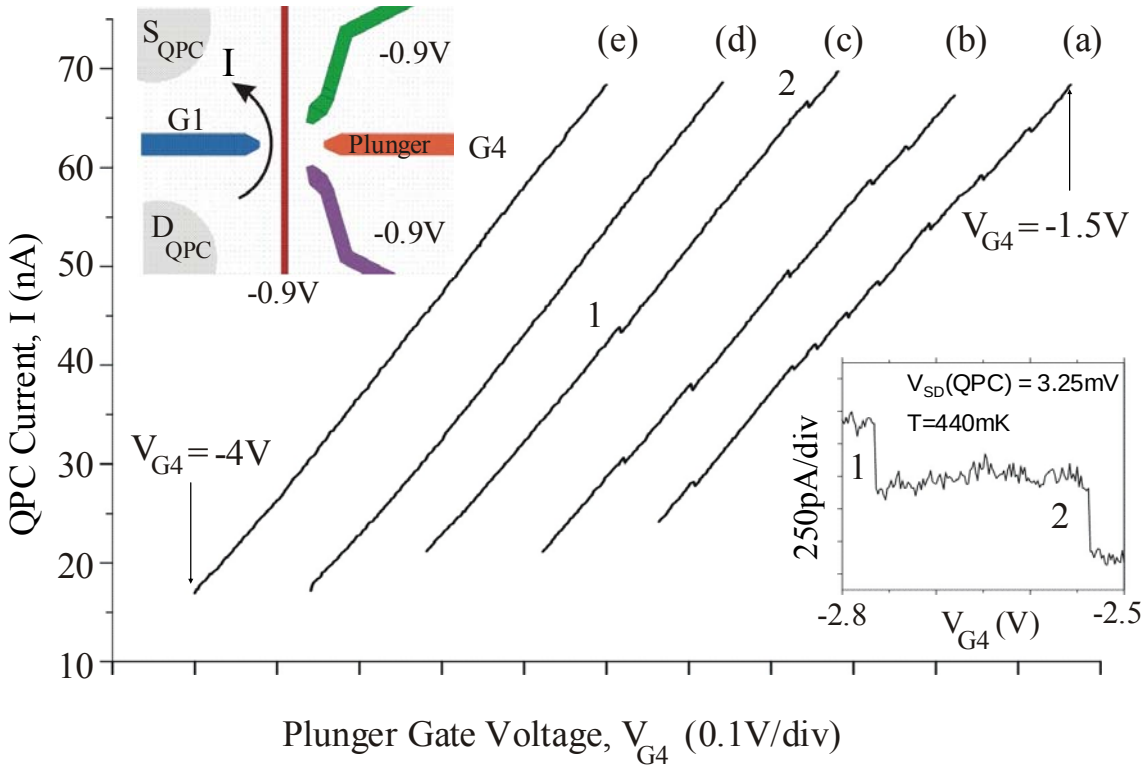

Figure 6.6: Single electron escape from the dot detected by the QPC transistor.

The plunger gate voltage, V_{G4}, is swept from -1.5V to -4V with a scan rate of 4mV/sec starting at curve marked (a) and ending at (e) with each curve spanning 0.5V. Gates G2, G3 and G5 are held at -0.9V while G1 is changed in-between each curve, to reset the QPC current. The curves have been offset along the voltage axis to fit on one graph. The point contact current is now seen to vary in a saw-tooth fashion as opposed to the smooth modulations and random switching that were observed in Figure 6.4. A small discrete positive step is seen for each electron ejected. The occurrence of such sharp discrete steps is explained by the non-equilibrium potential diagram shown in Figure 6.7. Upon

formation, a few excess electrons remain trapped in a long-lived meta-stable state. The plunger gate sweep cycle from -1.5V to -4.0V completely expels all electrons trapped in the dot potential. The last electron emission event occurs on curve (c) at a voltage of about G4=-2.75V on the plunger gate. In order to ensure that the absence of further steps is not due to very slow tunneling times, the barrier gate voltage G3 was raised just after the last detected step to allow any remaining electrons to escape. Only a smooth increase in the QPC current could be observed due to the capacitive coupling between the point contact and the tunnel barrier gate with no evidence for any remaining electrons. The lower inset to Figure 6.6 shows the steps corresponding to the last two electrons after subtracting out the background slope. The observed single electron step size is about 500pA with a signal to noise ratio of nearly 10.

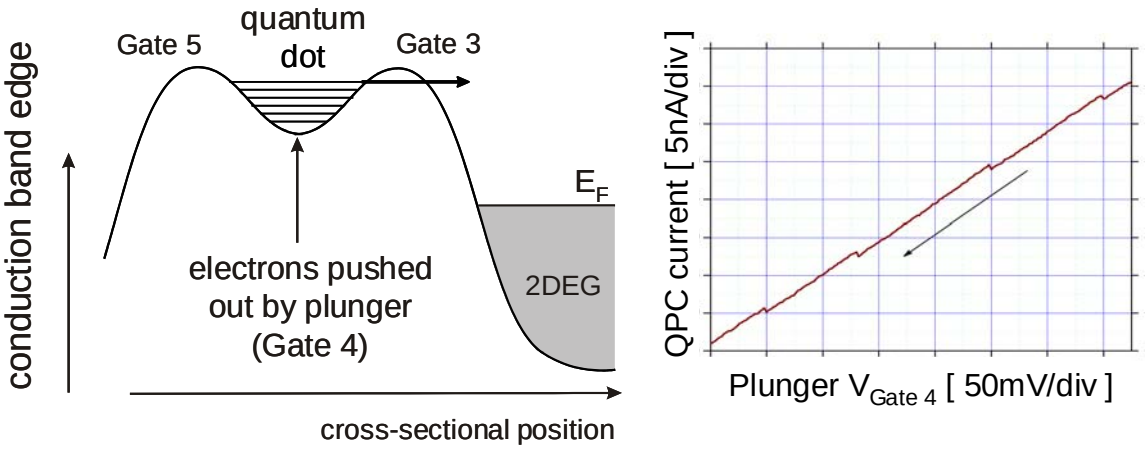

Figure 6.7: Single electron escape from the meta-stable dot catalyzed by the plunger voltage.

Upon sweeping the plunger gate from -4.0V back to -1.5V at the same scan rate as in the forward direction, no electrons were observed to re-enter the dot. This comes about when the last few electrons remain trapped at energy levels far above the Fermi level in the surrounding 2DEG, as shown in Figure 6.7. Strongly isolated dots can trap electrons in long-lived non-equilibrium state for durations exceeding tens of minutes. However, they may be expelled from the dot by forcibly pushing them over the tunnel barriers with a sufficiently large repulsive voltage on the plunger, and they cannot subsequently re-enter. Cooper et al., [76] have studied the decay of electrons from such artificial dots and the decay simply mimics the alpha decay from a radioactive nucleus. In fact, electrostatic quantum dots can also be thought of as artificial atoms [77] and a periodic table of artificial elements can be constructed [78].

6.3. Single photo-electron trapping, storage and detection

The calibration of the device upon cool-down described in the preceding two sections, allows for a precise determination of the gate voltages required to prepare the desired empty state of the dot, prior to optical exposure. The device preparation steps consist of cycling the plunger between the voltage levels that transition the dot from the long-lived non-equilibrium filled state to the equilibrium empty state. The charge state of the dot is read-out from the QPC transistor channel. Figure 6.8 illustrates the behavior in the QPC transistor current associated with the emission of electrons from the dot in a plunger cycle.

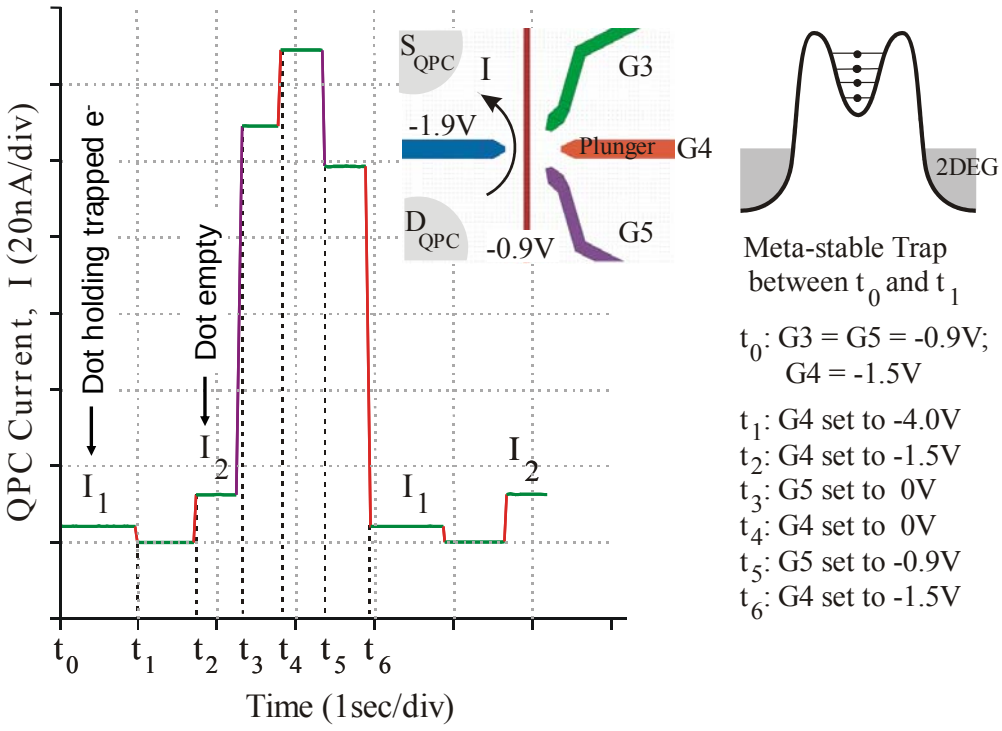

Figure 6.8: Hysteresis measured in the current through the QPC transistor, associated with the transition of the dot from the meta-stable filled state to the equilibrium empty state.

Immediately following time t_0, and equivalently time t_6, the dot exists in the meta-stable state with excess trapped electrons. The thick tunnel barriers formed in our geometry when G3 and G5 are at -0.9V prevent fast tunneling of the trapped electrons although the dot potential resides above the surrounding Fermi level, as shown in the top right inset to Figure 6.8. At t_1, the setting of gate V_{G4} = -4.0V is so extreme that it overwhelms the barriers and the well trapping potential becomes a repulsive potential forcing the electrons out within the fall-time of the plunger voltage. They do not subsequently re-

enter when the potential well is re-created at t_2, owing to the thick barriers and the dot created in the equilibrium empty state. In the cycle from t_0 to t_2, the QPC current switches from lower level I_1 to the upper level I_2 reflecting the charge removal from the adjacent quantum dot. When the barriers are re-opened and closed in the cycle from t_3 to t_6, electrons remain trapped in the dot restoring the current to I_1. The color of the vertical transitions is coded to the color of the corresponding gate switch for that transition. Level I_2 represents the desired empty state of the dot, at which it is ready to accept and trap photo-injected electrons.

The sample was illuminated using a Ti-Sapphire laser running CW at 10mW and tuned to 760nm. The output was pulsed through a Pockel's cell with an extinction ratio of ~550 and driven by a timed pulse generator. The pulsed output from the Pockels cell was further attenuated using a neutral density filter set and coupled into a single mode step index fiber and focused onto a spot size 100μm diameter on the sample. The Aluminum mask blocks almost all of the incident photon flux except directly above the dot where the 200nm radius pin-hole aperture is etched. Assuming a Gaussian profile for the incident spot over the illumination area of radius 50μm, and given the 200nm radius of the electrostatic dot, the photon flux into the dot is reduced by a factor of 10^{-5} compared to the total incident flux.

Figure 6.9, which plots the QPC transistor current versus time, presents a typical experimental result of exposure to a series of consecutive pulses after emptying the dot,

prior to the first pulse. During this experiment, the incident photon flux was maintained at 0.1 photons/pulse within the dot area.

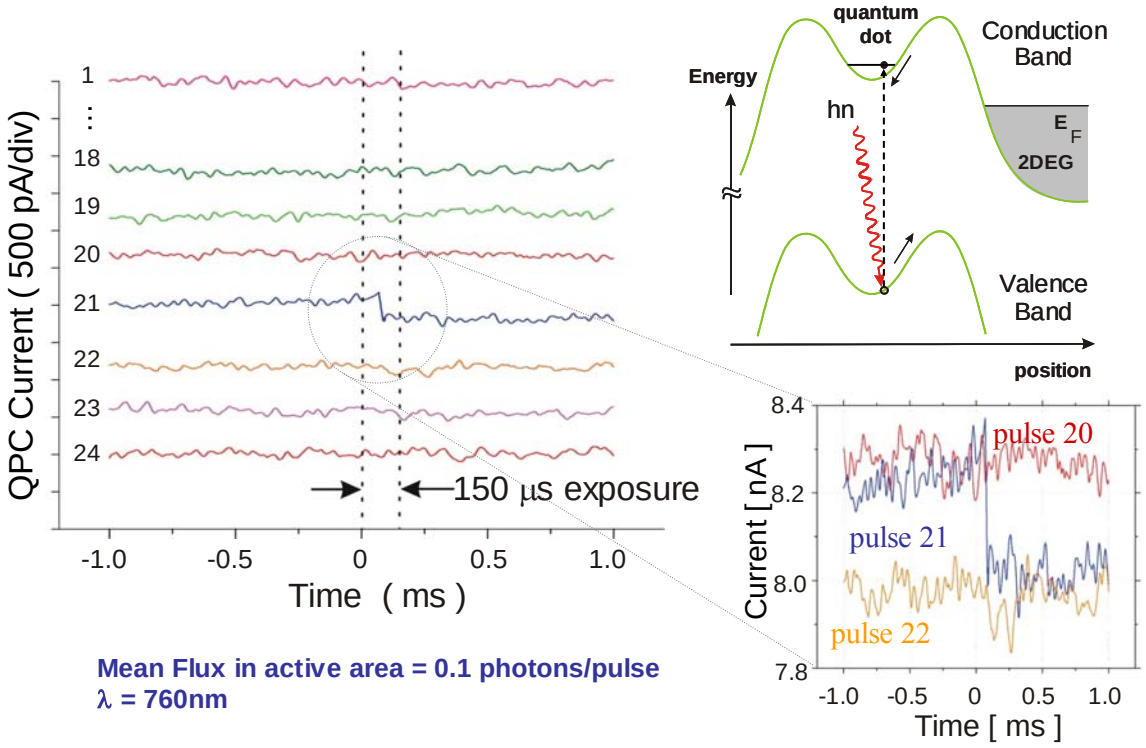

Figure 6.9: Photo-electron trapping in the quantum dot potential well flagged by adjacent point contact transistor.

Time t = 0 in Figure 6.9 marks the time at which the Pockels cell is opened, for a pulse duration of 150μsec. When a photon is absorbed within the active area, and the photo electron gets trapped in the dot, a sharp drop in transistor current is seen as for pulse 21 in the series. The current step size is consistent with the expected single electron steps determined from the electrical characterization in Figure 6.6. After emptying the dot by the plunger gate G4, if even any one of the gates G3, G4 or G5 is grounded, the quantum

dot is open and negative photo conductivity steps were not observed. We thus rule out the possibility of negative photo conductivity steps due photo-electron trapping in donors, DX-centers and traps in the SiO_2 layer. The fall time associated with the single electron signal is 20μsec, consistent with the speed of the pre-amplifier that is used. The signal-to-noise ratio for single electron detection is about 6 as seen in the inset to Figure 6.9. The 20kHz bandwidth of the detection circuit, limited by the pre-amp, leads to a single electron charge sensitivity of 10^{-3} e/$[Hz]^{1/2}$.

Increasing the photon flux over the dot increases the frequency of occurrence of negative photo-conductivity steps. Figure 6.10 shows a series of traces for a photon flux of 1.2 photons/pulse into the dot with no reset to empty the dot between pulses. Based on the frequency of occurrence of photo-detection events, we estimate the photo-electron trapping quantum efficiency to be about 10%. Interspersed among the negative steps, some positive steps were occasionally seen, as in the 34^{th} pulse. Such positive signals were seen with a 1% occurrence rate and can be attributed to the photo-ionization of residual neutral donors close to the quantum dot. The occasional positive steps were more noticeable when the dot held several photo-electrons, possibly due to the additional mechanism of photo-electron ionization or photo-hole annihilation within the dot. The positive steps are rare since almost all the photo-holes are swept away by the surrounding negatively biased gate electrodes.

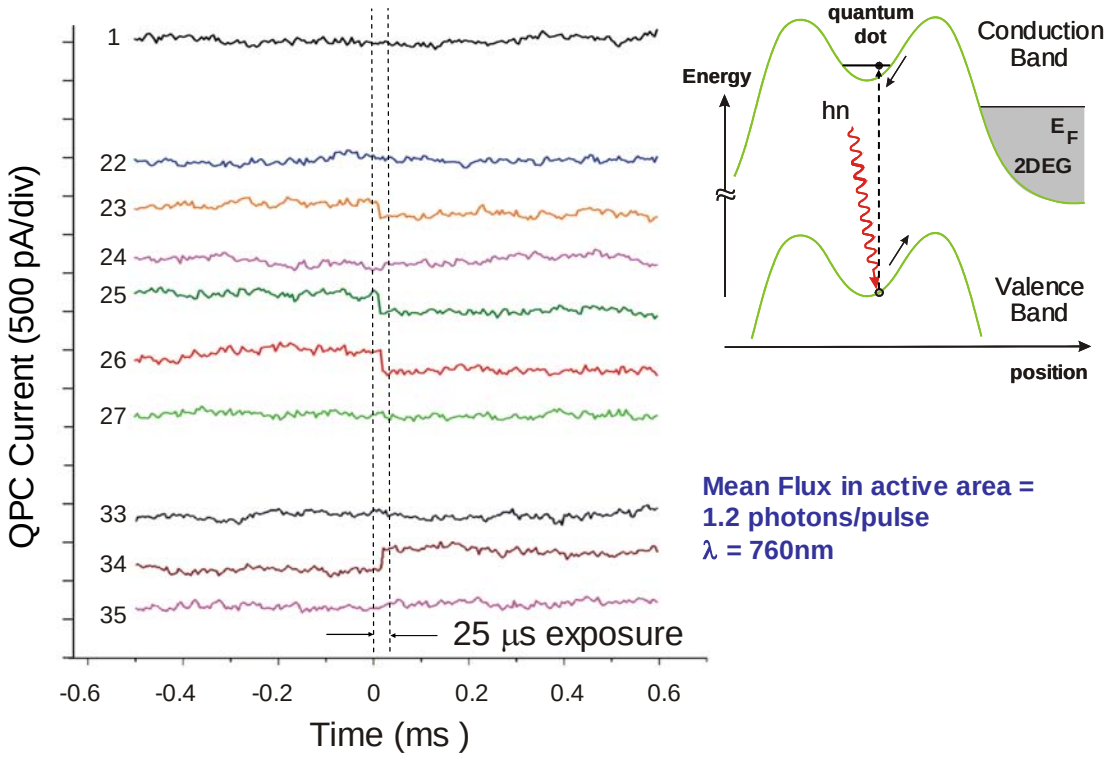

Figure 6.10: Optical exposure with an increased average flux within the dot area. Occasional positive steps in the exposure window can be attributed to the photo-ionization of a residual neutral donor, or the annihilation of a photo-hole within the dot.

CHAPTER 7 Photo-electron trapping, storage and detection in a InGaAs/InAlAs MODFET

In Chapter 6, we discussed the realization of a single electron quantum dot with an integrated point contact transistor for photo-electron injection, storage and detection in a conventional GaAs modulation doped FET. The GaAs material system is a superior and well-studied system compared to other III-V materials. A nanoscale single photon detector with photo-electron storage in GaAs would enable easy integration of a detector for optically injected spins with other purely electronic single spin devices, which have reached quite a mature stage in GaAs [80].

In addition to the implementation of individual photo-electron trapping and storage in GaAs, we have also made experimental progress towards devices in the InGaAs family of materials, another very promising III-V material system. With InGaAs, it becomes possible to operate at wavelengths in the 1.3 μm or the 1.55 μm low-loss windows of optical fibers. In this chapter, we discuss the implementation of single photon detection and photo-electron storage in an InGaAs based modulation doped FET. The results presented in this chapter can also be found in reference [ ]

7.1. Vertical QPC-Quantum Dot configuration

Unlike the AlGaAs/GaAs MODFET, we have studied the implementation of a QPC-Quantum dot arrangement in a vertical configuration created in a double quantum well heterostructure. This configuration simplifies the gate geometry, while the complexity is transferred into the heterostructure makeup. At this time though, we do not claim the superiority of one configuration over the other. Each configuration has it's own merits and can be optimized to obtain the desired control over photo-electron trapping and detection. A detailed description of the layer structure and band alignment has been provided in section 3.2. Two InGaAs quantum wells formed between InAlAs higher band-gap barrier layers have been used as shown in Figure 7.1 (a). In Figure 7.1 we show a schematic description of the double quantum well heterostructure we have used and the gate electrode layout to achieve the vertical QPC-quantum dot situation.

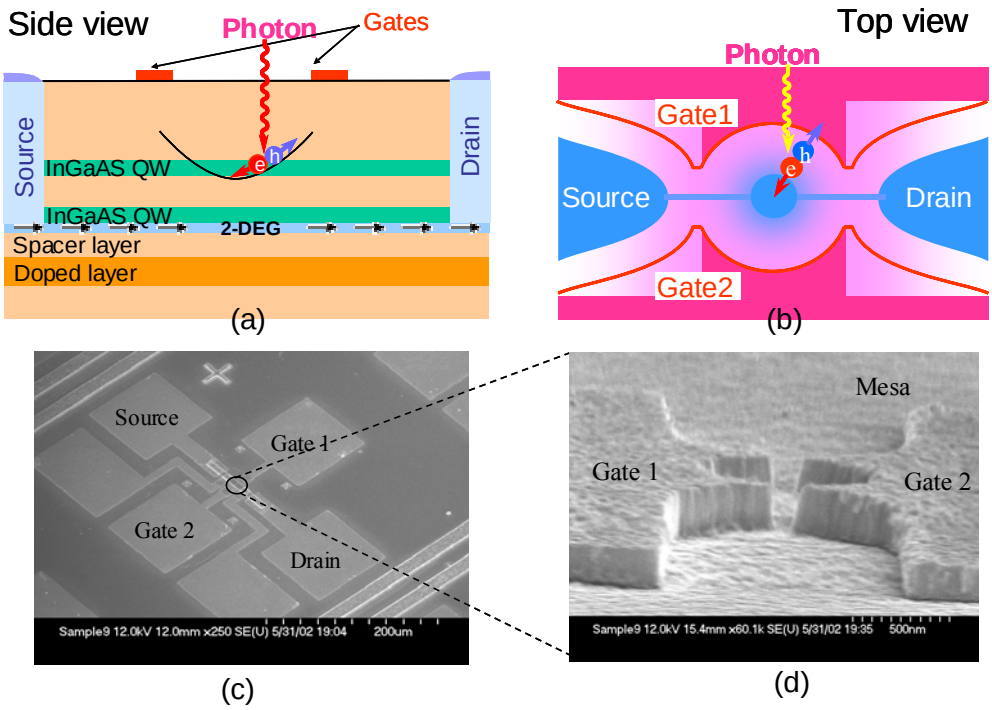

Figure 7.1: Split electrode geometry over a double QW heterostructure designed to create an electrostatic quantum dot vertically above the sensing QPC channel.

The upper InGaAs quantum well serves as the photo-absorption layer with a band-gap corresponding to 1.3 μm. This layer is situated above the source/drain 2DEG channel layer in the lower quantum well, separated by a barrier layer made of $In_{0.52}Al_{0.48}As$. $In_{0.52}Al_{0.48}As$ is chosen as the barrier layer as opposed to the more conventional InP barriers due to a relatively higher conduction band offset between InAlAs and InGaAs (0.5eV vs. 0.23eV).

A split-gate electrode geometry with a circular window, 1 μm in diameter, is used to create an electrostatic quantum dot vertically above the sensing QPC channel. The gate metal surrounding the circular window masks out unnecessary light exposure and fixes the potential at the edges surrounding the window. When negative voltages are applied to the two split gates, the energy bands in the heterostructure are pulled up and a 2-dimensional potential minimum is created at the center of the gates in the upper quantum well as shown schematically in Figure 7.1 (b). This potential well is used to trap photo-electrons in the upper quantum well. The electric field in the electrostatic potential well separates out the electron-hole pair created by a photon. The photo-electron naturally has a tendency to move towards the potential minimum at the center, while the hole is pulled towards the negative gates as schematically shown in Figure 7.1 (b). Simultaneously, the constrictions in the 2DEG are created at the edges of the circular gates which act as

sensitive point contact FET transistors, capable of sensing single charges trapped in the potential well. In Figure 7.1 (c) and (d) we show scanning electron micrographs of the device and split circular gates on the surface, fabricated as explained in **Error! Reference source not found.**.

7.2. Single photo-electron trapping, storage and detection

A striking feature of the experimental results to be discussed in this section, is the wavelength dependence of photo-electron and photo-hole trapping phenomena as opposed to the GaAs devices where a positive persistent increase in conductivity is common. Thus, a separate opaque photo-mask to suppress positive photo-conductivity and filter out negative steps, as in the case of the GaAs devices is un-necessary in these devices. The upper quantum well, designed to have an inter-band transition gap at 1.3μm, provides a clear wavelength dependent enhancement in negative photo-conductivity steps. 1.77 μm light produces positive photoconductivity effectively doping the channel, while 1.3 μm light produces negative photoconductivity steps caused by photo-electron trapping.

First, we discuss the spectral dependence of channel conductivity shown in Figure 7.2. The source/drain channel current is measured at a constant voltage drop V_{SD} = 0.5 mV, at a temperature of 4.2 K. We begin with an un-pinched channel initially, and sweep the wavelength from 1 μm up to 1.8 μm over an 80 s time period. First, the current monotonically decreases with increasing wavelength, with no further decrease at around

1.3 μm, the band gap of the InGaAs quantum wells. Beyond 1.3μm, the conductivity reverses trend and begins to increase with wavelength. Negative photoconductivity is explained by an increase in concentration of negative trapped charges with exposure that cumulatively have the effect of pinching the channel current. At wavelengths shorter than 1.3 μm, inter-band absorption occurs in photo-absorption InGaAs quantum well and in the lower channel layer. The photoelectrons in the conducting channel are mobile, and thus cannot contribute to trapped charge. The negative steps thus must originate from photoelectrons produced and trapped in the absorption layer near the sensitive point contact constrictions of the gate electrodes.

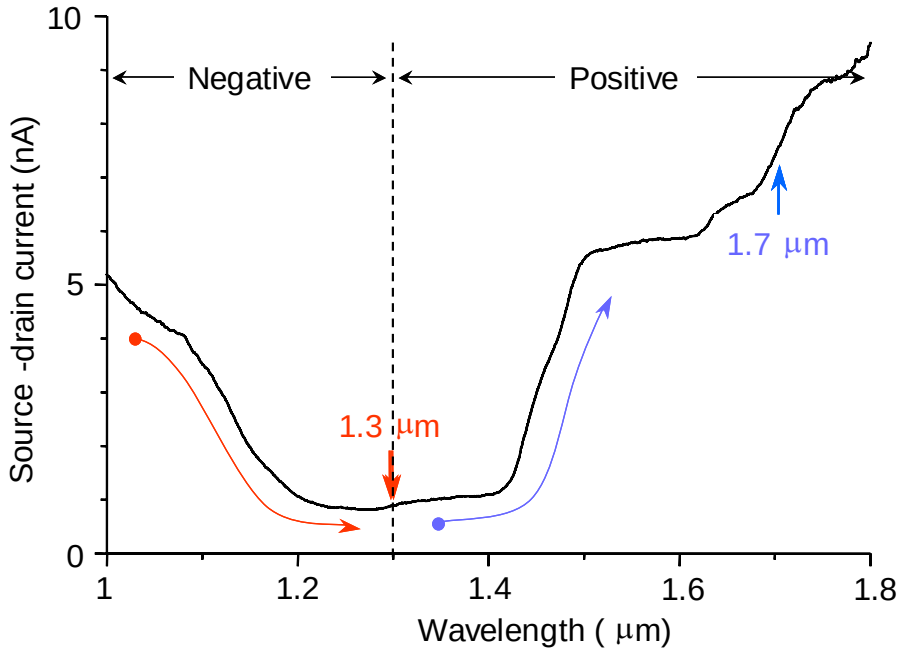

Figure 7.2: Spectral dependence of the conductivity of the QPC channel.

The positive photoconductivity beyond 1.3μm is due to the enhancement in 2DEG density in the channel caused by photo-ionization of frozen donors in the n-InAlAs doped layer. As a normal practice in the single photon experiments in these devices, we initially prepare the photo-detectors for use after cooling down to 4.2K, by means of a deep soak using 1.77 μm light, to fully ionize the donors and to populate the source/drain channel.

In Figure 7.3, we show the result of exposure of a freshly prepared device to highly attenuated light at two wavelengths. The sample is illuminated by monochromatic light through a large core glass fiber that is carefully shielded to block any photons from the outer jacket with the same experimental set-up described in CHAPTER 5. The light is created by a tungsten lamp and then filtered by a monochromator, a long-pass filter passing wavelengths > l000 nm, and a 30-dB neutral density filter. The fiber was end-fire coupled to the device and the illumination area in the plane of the device was about 5 mm in diameter. The most likely and favorable region for persistent trapping of photo-electrons is the 2D potential well region encircled by the gate electrodes with a total diameter of 1μm and an active area of 7.9×10^{-9} $cm^{2.}$ Assuming a Gaussian profile for the incident spot on the device with the measured 2.5mm radius FWHM spot, we estimate the actual light power in the active area to be 2.8×10^{-8} times smaller than the total incident power. The photon flux specified in the following experimental results is estimated by multiplying the measured flux in the 5mm spot by this scaling factor.

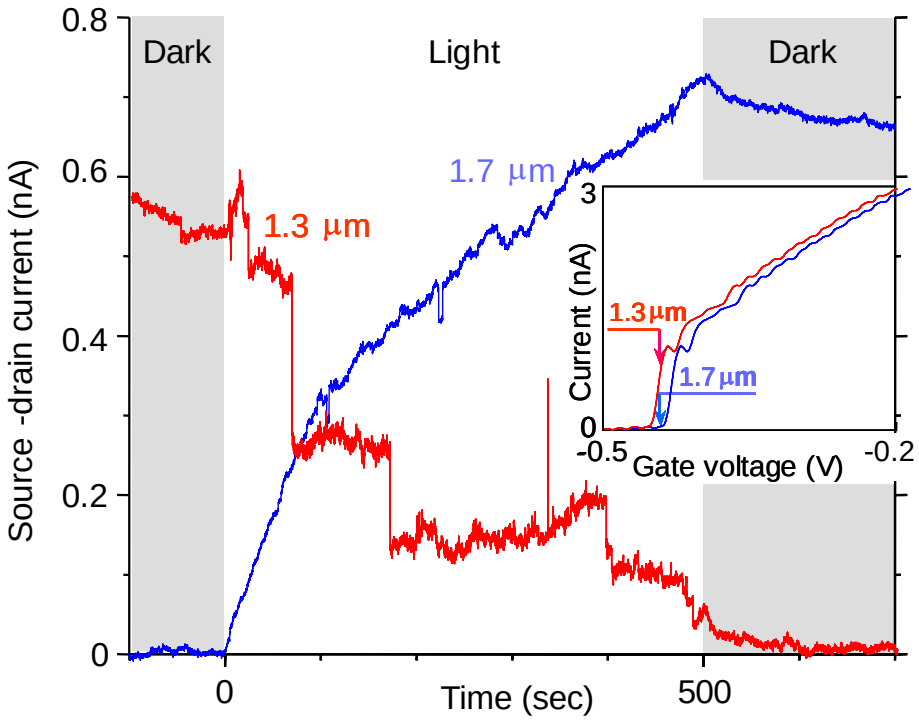

Figure 7.3: Photo-electron trapping induced negative persistent photoconductivity steps at the 1.3 μm inter-band transition gap of the InGaAs quantum well.

The pinch-off behavior in the source-drain conductance (I_{SD}-V_g curve) is shown in the inset to Figure 7.3. The left-most I-V curve in the inset corresponds to full modulation doping after a sustained exposure to 1.77 μm light. After the deep soak at 1.77 μm, to produce full channel doping, the gate voltages are adjusted for a current around 0.6 nA. The device is then exposed to a photon flux of 100 photons/sec in the active area at a wavelength of 1.3 μm (red curve labeled 1.3 μm). The photon exposure causes the current to drop inexorably, step by step, except for occasional upward spikes. The current drop means that the net negative charge is trapped near the source/drain channel. The

occasional spikes we associate possibly with de-trapping and re-trapping of photoelectron, an effect that is seen also in Figure 7.4. Thus, as a result of trapped photoelectrons, the current is again pinched off, and due to the excess negative charge near the point contacts, the I_{SD}-V_g curve is shifted toward positive gate voltages, as shown in the right-most curve of the inset. At the pinch-off condition, if the device is again exposed to 1.77 μm light, the channel current is restored (blue curve labeled 1.7 μm). The incident photon rate in the active window area for both wavelengths is about 100 photons/s. Since the absorptivity in the absorption quantum well is about 1%, on average 1 photon/sec is absorbed in the window area. Thus the quantum efficiency for producing negative steps from the observed 4 trapping events in the 500sec exposure window is about 0.01%. The difference in the magnitude of jumps in the current can be ascribed to the different positions where photoelectrons are trapped. Similar effects are seen for photo-hole trapping events [56, 66]. The exposure to 1.77 μm photons can energetically cause only photo-ionization of neutral donor atoms, since photon energy is smaller than any of the band gaps. Photo-ionization mostly occurs in the n-doped InAlAs layer and photo-exited electrons end up increasing the 2DEG channel density.

We would like to emphasize the point that the negative photo-conductivity steps see at 1.3μm could be caused by the trapping of electrons by ionized donors, although very dilute in concentration, in the 2D potential minimum region between the circular gates. Hence by having an incomplete initial soak at 1.77 μm, we can set-up the device with un-ionized neutral donor atoms. The amount of "soaking" which enhances the 2DEG density

is calibrated against the achieved channel pinch-off voltage. We can control the pinch-off voltage between -0.5 V and +0.1 V. Now, when the pinch-off voltage is set nearly to zero, the 1.3 μm photocurrent still shows steps, but they are equally likely to be either positive or negative. The incomplete photo-ionization of donors in the initial state allows a balance between photo-electron trapping and photo-ionization. To make this phenomenon clear, we exposed the sample periodically to pulses maintaining the device in a balanced condition biased at ~0 V. The resulting QPC current behavior for 10 sec pulses every 50 seconds is shown in Figure 7.4.

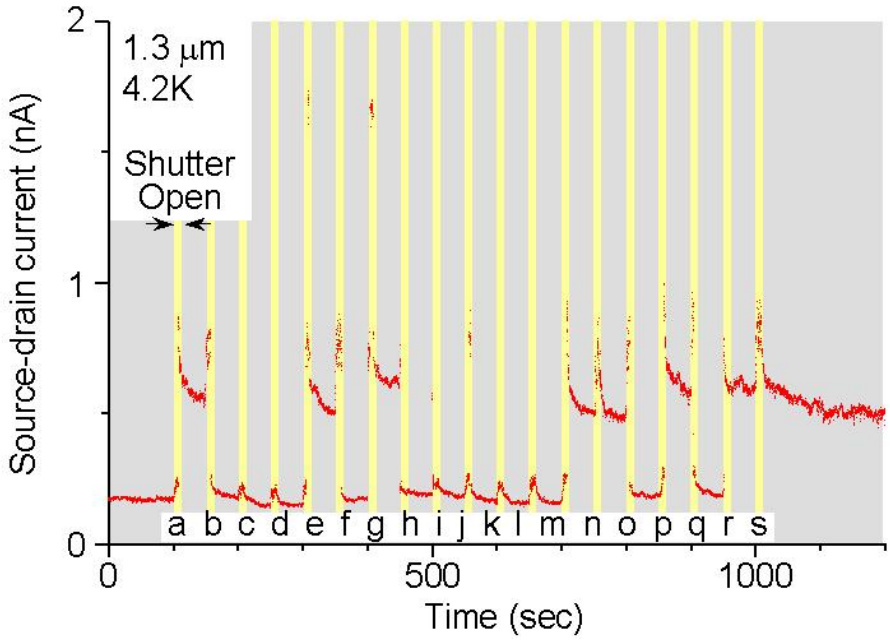

Figure 7.4: QPC current switching due to two competing single photon processes: Electron trapping and photo-ionization, obtained by a partial donor ionization at 1.77 μm prior to exposure at 1.3 μm.

The pulses are incident on the sample in time slots labeled a, b, c, etc. The photon number in the active area was maintained at an average value of 30 photons in the 10 sec interval. As seen, optical exposure can cause either electron trapping (negative step) or photo-ionization (positive step), alternating depending on the previous state. Sometimes, multiple optical pulses are required before the state would alternate. Within the 10 sec optical exposure interval, there might be a transient thermal response, as in time slot g; but such quick transients return to either of the two alternating states after the pulse. In the dark, the states were stable for more than 1 hour.

The switching behavior in Figure 7.4 is due to photoelectron trapping/detrapping located either in (i) the shallow circular potential well between the window gates in the absorption layer, or (ii) at donor sites. In case (ii) the donors that could contribute to trapping/detrapping are the residual donors in the absorption layer rather than those in the modulation doped layer. The modulation-doped donors, are located far below the channel, to produce the desired step in photo-conductivity. They can cumulatively produce smooth increase in conductivity by photoionization as was seen in Figure 7.3 for 1.77 μm light. As mentioned above, the two possible mechanisms for the positive steps in Figure 7.4 are the photo-ionization of the trapped electron, or annihilation of the trapped electron by injected holes. The photo-ionization mechanism would require a specific photo-ionization cross section to be consistent with the rough equality between trapping and de-trapping rates. On the other hand, annihilation by photo-holes would require a hole trapping rate that is roughly coincident with the electron trapping rate. Such a

favorable adjustment may have been made by the incomplete soaking of the device during preparation.

In conclusion, the implementation of a single photon detector suitable for quantum telecommunications at an optical frequency corresponding to a vacuum wavelength of 1.3μm has been discussed in this chapter. The device utilizes a specially engineered InAlAs/InGaAs double quantum well heterostructure: The quantum well closer to the surface traps photo-excited electrons in a 2D potential minimum created by circular e-beam lithography defined Schottky gate electrodes; the lower quantum well, which is modulation doped, contains the integrated point contact FET channel for non-intrusively sensing single trapped electrons and thus flagging the arrival of a single photon over the channel.

CHAPTER 8 Conclusions

This dissertation has presented the implementation of a Single Photon Detector utilizing the principle of Photoconductive Gain in a conventional Field Effect Transistor. Photoconductive Gain as opposed to other gain mechanisms such as avalanche multiplications processes provides a gentle and benign way of detecting single photons, where the original photo-excited electron can be safely preserved upon detection. The safe storage of the photo-excited electron and it's internal spin state is crucial for the electron spin based nanoscale semiconductor devices for emerging new applications such Quantum Cryptography and Quantum Teleportation.

The photo-detector has been implemented in conventional modulation doped high electron mobility devices with a 2-Dimensional Electron Gas at the hetero-interface. Electrostatic squeezing of the electron gas by negatively biased surface gate electrodes allows for the creation of lower dimensional structures such as one-dimensional Quantum Wire FETs and zero-dimensional Quantum Dot potential wells. The integrated FET-Electrostatic Quantum Dot geometry allows for precise control and read-out of the charge state of the quantum dot.

The single photo-electron trapping and storage has been accomplished in an empty electrostatic quantum dot in the AlGaAs/GaAs material system (Chapter 6) that can be controllably created prior to photo-excitation of inter-band electrons. Recently,

experiments demonstrating the electrical measurement of a single electron spin inserted in a similar electrostatic dot [80] and in a commercial Silicon field effect transistor [81] have been reported. The successful trapping and detection of photo-electrons reported in this dissertation, in spite of the usually dominant positive photo conductivity, would enable the implementation of a detector for an optically injected spin.

Specially engineered heterostructures such as the InGaAs/InP/InAlAs heterostructure discussed in chapter 7 allows for transfer of quantum information from photon spin to photo-electron spin without leaving behind any information in the photo-excited hole state. By combining the single photon detection implementation discussed in this dissertation, with the single spin measurement techniques based on a spin-to-charge conversion [80, 81], it would be possible to convert a flying qubit (photon) into a stationary qubit (trapped electron) and to read-out the spin state. A Single Photon Detector based on non-invasive gain mechanisms such as Photoconductive Gain could enable the implementation of opto-spintronic devices for emerging applications in quantum information science.

BIBLIOGRAPHY

1. Simon Singh, "The Code Book: The Science of Secrecy from Ancient Egypt to Quantum Cryptography", Delacorte Press, New York, 2002.

2. C.E. Shannon, "A mathematical theory of communication", Bell Systems Technical Journal, Vol 28, p 656, 1949.

3. R.L. Rivest, A. Shamir, L. Adleman, "A method for obtaining digital signatures and public-key cryptosystems", Communications of the ACM, vol.21, no.2, pp.120-6, Feb. 1978.

4. P.W Shor, "Polynomial-time algorithms for prime factorization and discrete logarithms on a quantum computer", SIAM Journal on Computing, vol.26, no.5, pp.1484-509, Oct. 1997.

5. A. Ekert, "Quantum Keys for keeping secrets", New Scientist, pp.24 – 28, Jan 1993.

6. C.H. Bennett, and G. Brassard, "Quantum Cryptography: Public key cryptography and coin tossing", in Proc. Int. Conf. Computer Systems and Signal processing, Bangalore, India, pp.175-179, 1984.

7. R.J. Hughes, G.L. Morgan, C.G. Peterson, "Quantum key distribution over a 48 km optical fibre network", Journal of Modern Optics, vol.47, no.2-3, pp.533-47, March 2000.

8. http://www.idquantique.com

9. A. Zeilinger, **"**Quantum teleportation", Scientific American, vol.282, no.4, pp.50-9. April 2000.

10. A. Einstein, B. Podolsky, N. Rosen, "Can Quantum-Mechanical Description of Physical Reality be considered complete?", Physical Review, vol 47, pp 777-780, May 1935.

11. Stuart J. Freedman and John F. Clauser, "Experimental Test of Local Hidden-Variable Theories", Physical Review Letters, Vol 28, pp 938–941, April 1972.

12. Alain Aspect, Philippe Grangier, and Gérard Roger, "Experimental Tests of Realistic Local Theories via Bell's Theorem", Physical Review Letters, Vol 47, pp 460–463, Aug 1981.

13. Paul G. Kwiat, Klaus Mattle, Harald Weinfurter, and Anton Zeilinger, “New High-Intensity Source of Polarization-Entangled Photon Pairs”, Physical Review Letters , Vol 75, pp 4337–4341, Dec 1995.

14. W. Tittel, J. Brendel, H. Zbinden, and N. Gisin, “Violation of Bell Inequalities by Photons More Than 10 km Apart”, Physical Review Letters , Vol 81, pp 3563–3566, Oct 1998.

15. Gregor Weihs, Thomas Jennewein, Christoph Simon, Harald Weinfurter, and Anton Zeilinger, “Violation of Bell's Inequality under Strict Einstein Locality Conditions”, Physical Review Letters, Vol 81, pp 5039–5043, Dec 1998.

16. Bennett CH and Wiesner SJ, “Communication via one- and two-particle operators on Einstein-Podolsky-Rosen states” Physical Review Letters, vol.69, no.20, pp 2881-2884, Nov. 1992.

17. D. Bouwmeester, A Ekert, A. Zeilinger, “The Physics of Quantum Information: Quantum Cryptography, Quantum Teleportation, Quantum Computation”, Springer, New York, 2000.

18. Michael A. Nielsen and Isaac L. Chuang, “Quantum computation and quantum information”, Cambridge University Press, New York, 2000.

19. Amnon Yariv, “Optical Electronics” Oxford University Press, New York, 1997.

20. Stuart J. Freedman and John F. Clauser, “Experimental Test of Local Hidden-Variable Theories”, Physical Review Letters, vol. 28, no. 14, pp 938–941, April 1972.

21. M. Zukowski, A. Zeilinger, M. A. Horne and A. K. Ekert, “Event-ready-detectors: Bell experiment via entanglement swapping”, Physical Review Letters, vol. 71, no. 26, pp 4287–4290, Dec1993.

22. S. Bose, V. Vedral, and P. L. Knight , “Multiparticle generalization of entanglement swapping”, Physical Review A, vol 57, no. 2 pp 822–829, Feb 1998.

23. Duan L-M, Lukin MD, Cirac JI, Zoller P “Long-distance quantum communication with atomic ensembles and linear optics”, Nature, vol.414, no.6862, pp.413-18, Nov. 2001.

24. “Concepts in Photoconductivity and Allied Problems”, edited by A. Rose, Krieger, Huntington, New York, 1978.

25. Millikan R.A, Physical Review, Vol 32, p 349, 1911; http://en.wikipedia.org/wiki/Oil-drop_experiment

26. Rutger Vrijen, Eli Yablonovitch, Kang Wang, Hong Wen Jiang, Alex Balandin, Vwani Roychowdhury, Tal Mor, and David DiVincenzo, "Electron-spin-resonance transistors for quantum computing in silicon-germanium heterostructures", Physical Review A, vol 62, no. 1, pp 012306-15, July 2000.

27. Schulz M, "Interface states at the SiO_2-Si interface", Surface Science, vol.132, no.1-3, pp.422-55, Sept. 1983.

28. Ralls KS, Skocpol WJ, Jackel LD, Howard RE, Fetter LA, Epworth RW, Tennant DM, "Discrete resistance switching in submicrometer silicon inversion layers: individual interface traps and low-frequency (1/f) noise", Physical Review Letters, vol.52, no.3, pp.228-31, Jan. 1984.

29. T.A Fulton, G.J Dolan, **"**Observation of single-electron charging effects in small tunnel junctions", Physical Review Letters, vol.59, no.1, pp 109-112, July 1987.

30. M.H. Devoret, H. Grabert in Single Charge Tunneling, Plenum Press, New York 1992.

31. Michel H. Devoret and Robert J. Schoelkopf, "Amplifying quantum signals with the single-electron transistor", Nature, Vol 406, pp 1039-1046, Aug 2000.

32. Silvano Donati, "Photodetectors: Devices, Circuits and Applications", Prentice Hall, New Jersey, 2000.

33. R. Vrijen, E. Yablonovitch, "A spin-coherent semiconductor photodetector for quantum communication", Physica E, vol.10, no.4, pp.569-75, June 2001.

34. H. Kosaka, AA. Kiselev, F.A. Baron, Ki Wook Kim, E. Yablonovitch, "Electron g factor engineering in IlI-V semiconductors for quantum communications", Electronics Letters, vol.37, no.7, 29 March 2001, pp.464-5.

35. A.M. Tyryshkin, S.A. Lyon, A.V. Astashkin, A.M. Raitsimring, "Electron spin relaxation times of phosphorus donors in silicon", Physical Review B, vol.68, no.19, 15 Nov. 2003, pp.193207-1-4

36. D. D. Awschalom, J. M. Kikkawa, "Electron spin and optical coherence in semiconductors", Physics Today, vol.52, no. 6, pp.33-38, June1999.

37. I. Malajovich, J.M. Kikkawa, D.D. Awschalom, J.J. Berry and N. Samarth, "Coherent Transfer of Spin Through a Semicondutor Heterointerface" Phys. Rev. Lett. 84, 1015, 2000.

38. S.M. Sze, "Physics of semiconductor devices", Wiley, New York, 1981.

39. Y. Kawamura, K. Nakashima, H. Asahi, "Improvements of electrical and optical properties of InAlAs grown by molecular beam epitaxy", Journal of Applied Physics, vol.58, no.8, 15 Oct. 1985, pp.3262-4.

40. A.A. Kiselev, K.W Kim, E. Yablonovitch, "Designing a heterostructure for the quantum receiver", Applied Physics Letters, vol.80, no.16, April 2002, pp.2857-9.

41. T.J. Thornton, M. Pepper, H. Ahmed, D. Andrews, G.J. Davies, "One-dimensional conduction in the 2D electron gas of a GaAs-AlGaAs heterojunction", Physical Review Letters, vol.56, no.11, 17 March 1986, pp.1198-201.

42. H.Z. Zheng, H.P. Wei, D.C. Tsui, G. Weimann, "Gate-controlled transport in narrow GaAs/AlGaAs heterostructures", Physical Review B, vol.34, no.8, pt.2, 15 Oct. 1986, pp.5635-8

43. H. van Houten, C. W. J. Beenakker, B. J. van Wees, Quantum point contacts, in Nanostructured Systems, M. A. Reed, Ed. (Academic Press, San Diego, 1992), vol. 35, pp. 9-112.

44. D.A. Wharam, M. Pepper, H. Ahmed, J.E.F Frost, D.G. Hasko, D.C. Peacock, D.A. Ritchie, G.A.C. Jones, "Addition of the one-dimensional quantised ballistic resistance", Journal of Physics C, vol.21, no.24, pp.L887-91, Aug. 1988.

45. R. Landauer, "Spatial Variation of currents and fields due to localized scatterers in metallic conduction", IBM Journal of Research and Development, vol. 1, no. 3, pp. 223-231, July (1957).

46. van Wees BJ, van Houten H, Beenakker CWJ, Williamson JG, Kouwenhoven LP, van der Marel D, Foxon CT. "Quantized conductance of point contacts in a two-dimensional electron gas", Physical Review Letters, vol.60, no.9, 29 Feb. 1988, pp.848-50

47. Williams, Ralph, "Modern GaAs processing methods", Artech House, Boston 1990.

48. Nebauer E, Lohse U, “Lamp furnace-annealed Au/Ni/AuGe ohmic contacts for GaAs MESFETs”, Physica Status Solidi A, vol.115, no.2, 16 Oct. 1989, pp.K171-3

49. J.H. Pugh, R.S. Williams, “Entropy-driven loss of gas phase group V species from gold/III-V compound semiconductor systems”, Journal of Materials Research, vol.1, no.2, March-April 1986, pp.343-51

50. A. Christou, “Solid phase formation in Au:Ge/Ni, Ag/In/Ge, In/Au:Ge GaAs ohmic contact systems”, Solid-State Electronics, vol.22, no.2, Feb. 1979, pp.141-9

51. A. G. Milnes and D. L. Feucht, “Heterojunctions and metal-semiconductor junctions” Academic Press, New York, 1972.

52. E.J. Mele, J.D. Joannopoulos, “Intrinsic surface states and Fermi-level pinning at metal-semiconductor interfaces”, Journal of Vacuum Science and Technology, vol.15, no.4, pp.1370-3, July-Aug. 1978.

53. G. Myburg, W.E. Meyer, F.D. Auret, H. Burger, W.O. Barnard, S.A. Goodman, “Fermi level pinning by metal Schottky contacts on n type GaAs”, Materials Science and Technology, vol.14, no.12, pp.1269-72, Dec. 1998.

54. H. Ohno, J. Barnard, C.E.C Wood, L.F. Eastman, “Double heterostructure InGaAs MESFETs by MBE”, IEEE Electron Device Letters, vol.EDL-1, no.8, Aug. 1980, pp.154-5

55. D.V.Lang in “Deep centers in semiconductors: a state of the art approach”, edited by Sokrates T. Pantelides, Gordon and Breach, New York, 1986.

56. Hideo Kosaka, Deepak .S. Rao, Hans .D. Robinson, Prabhakar Bandaru, Toshitsugu Sakamoto, Eli Yablonovitch, “Photoconductance quantization in a single-photon detector”, Physical Review B, vol.65, no.20, pp 201307(R)/1-4, May 2002.

57. K.J Thomas, J.T Nicholls, M.Y Simmons, M. Pepper, D.R. Mace, D.A. Ritchie, “Possible spin polarization in a one-dimensional electron gas” Physical Review Letters, vol.77, no.1, 1 July 1996, pp.135-8

58. A.C. Graham, K.J. Thomas, M. Pepper, M.Y Simmons, D.A. Ritchie, “0.7 structure in quantum wires observed at crossings of spin-polarised 1D subbands”, Physica E - Low-Dimensional Systems & Nanostructures, vol.22, no.1-3, April 2004, pp.264-7.

59. D.K. Maude, J.C. Portal, L. Dmowski, T. Foster, L. Eaves, M. Nathan, M. Heiblum, J.J. Harris, R.B. Beall, “Investigation of the DX center in heavily doped n-type GaAs”, Physical Review Letters, vol.59, no.7, pp.815-18, Aug. 1987.

60. D.J. Chadi, K.J. Chang, “Theory of the atomic and electronic structure of DX centers in GaAs and Al/sub x/Ga/sub 1-x/As alloys”, Physical Review Letters, vol.61, no.7, pp.873-6, Aug. 1988.

61. K. Zdansky, I.D. Hawkins, “Slow decay of photoconductivity caused by tin-related DX centers in AlGaAs”, Czechoslovak Journal of Physics, vol.49, no.5, pp. 813-21, May 1999.

62. R.J. Nelson, “Long-lifetime photoconductivity effect in n-type GaAlAs”, Applied Physics Letters, vol.31, no.5, pp.351-3, Sept. 1977.

63. G. Brunthaler, K. Ploog, W. Jantsch, “Photoluminescence transients due to hole capture at DX centers in AlGaAs:Si”, Physical Review Letters, vol.63, no.20, pp. 2276-9, Nov. 1989.

64. A. Kastalsky, J.C.M Hwang, “Study of persistent photoconductivity effect in n-type selectively doped AlGaAs/GaAs heterojunction”, Solid State Communications, vol.51, no.5, pp.317-22, Aug. 1984.

65. H.P. Wei, D.C. Tsui, M. Razeghi, “Persistent photoconductivity and the quantized Hall effect in In/sub 0.53/Ga/sub 0.47/As/InP heterostructures”, Applied Physics Letters, vol.45, no.6, pp.666-8, Sept. 1984.

66. A.J. Shields, M.P. O'Sullivan, I. Farrer, D.A Ritchie, R.A. Hogg, M.L. Leadbeater, C.E. Norman, M. Pepper, “Detection of single photons using a field-effect transistor gated by a layer of quantum dots”, Applied Physics Letters, vol.76, no.25, pp. 3673-5, June 2000.

67. P.M. Mooney, G.A. Northrop, T.N. Morgan, H.G. Grimmeiss, “Evidence for large lattice relaxation at the DX center in Si-doped AlGaAs”, Physical Review B, vol.37, no.14, pp.8298-307, May 1988.

68. R. Piotrzkowski, E. Litwin-Staszewska, F. Bosc, J. Sicart, J.L. Robert, “New type of persistent photoconductivity related to DX-center: the study of interband PPC in Si-doped AlGaAs” Physica B, vol.273-274, pp.792-5, Dec. 1999.

69. I.V. Kukushkin and K. von Klitzing and K. Ploog and V.E. Kirpichev and B.N. Shepel, “Reduction of the electron density in GaAs-AlGaAs single heterojunctions by continuous photoexcitation”, Physical Review B ,vol 40, No.6, pp. 4179-4182, Aug 1989.

70. J. Chen and C.H. Yang and R.A. Wilson and M.J. Yang, "Observation of negative persistent photoconductivity in an *n*-channel GaAs/$Al_xGa_{1-x}As$ single heterojunction", Applied Physics Letters, vol 60, no. 17, pp 2113-2115, Feb 1992.

71. U. Meirav, M.A. Kastner and S.J. Wind, Physical Review Letters, "Single-electron charging and periodic conductance resonances in GaAs nanostructures" vol 65, no. 6, pp 771-775, Aug 1990.

72. M. Field, C.G. Smith, M. Pepper, D.A. Ritchie, J.E.F. Frost, G.A.C. Jones and D.G. Hasko, "Measurements of Coulomb blockade with a non-invasive voltage probe", Physical Review Letters, vol 70, no. 9, pp 1311-1315, March 1993.

73. M. Ciorga, A.S. Sachrajda, P. Hawrylak, C. Gould, P. Zawadzki, S. Jullian, Y. Feng and Z. Wasilewski, "Addition spectrum of a lateral dot from Coulomb and spin-blockade spectroscopy", Physical Review B ,vol 61, No.24, pp. R16315, June 2000.

74. D. Sprinzak, Y. Ji, M. Heiblum, D. Mahalu and H. Shtrikman, "Charge Distribution in a Kondo-Correlated Quantum Dot", Physical Review Letters, vol 88, no. 17, pp 176805-176809, April 2002.

75. J.M. Elzerman, R. Hanson, J.S. Greidanus, L.H. Willems van Beveren, S. De Franceschi, L.M.K. Vandersypen, S. Tarucha and L.P. Kouwenhoven, "Few-electron quantum dot circuit with integrated charge read out", Physical Review B,vol 67, pp. R161308, 2003.

76. J. Cooper and C.G. Smith and D.A. Ritchie and E.H. Linfield and Y. Jin and H. Launois, Physica E, "Direct observation of single-electron decay from an artificial nucleus", vol 6, pp 457-460, 2000.

77. Ashoori, R.C, "Electrons in artificial atoms", Nature, Vol 379, No.1 , pp 413-419.

78. http://vortex.tn.tudelft.nl/grkouwen/qdotsite.html

79. Hideo Kosaka, Deepak .S. Rao, Hans .D. Robinson, Prabhakar Bandaru, Kikuo Makita, Eli Yablonovitch, "Single Photoelectron Trapping, Storage, and Detection in a Field Effect Transistor", Physical Review B, vol.67, no.20, pp 045104/1-4, Jan 2003.

80. J.M. Elzerman, R. Hanson, L.H. Willems van Beveren, B. Witkamp, L.M.K. Vandersypen and L.P. Kouwenhoven, "Single-shot read-out of an individual electron spin in a quantum dot", Nature, Vol 430, No. 6998, pp-431-435, 2004.

81. M. Xiao, I. Martin, E. Yablonovitch, H.W. Jiang, “Electrical detection of the spin resonance of a single electron in a silicon field-effect transistor”, Nature, vol.430, No.6998, 22, pp.435-9, July 2004.